UNIVERSITÉ DE STRASBOURG

ÉCOLE DOCTORALE MSII (ED n°269)

LABORATOIRE ICUBE (UMR 7357)

THÈSE

Présentée par:

HONGYU LI

Soutenue le 21/12/2021

pour obtenir le grade de: **Docteur de l'Université de Strasbourg**

Discipline/ Spécialité: **Signal, image, automatique, robotique**

Development of an SPR microscope for phase imaging with digital holography

THÈSE dirigée par :
M. Yoshitate Takakura — Maître de conférences, HDR, Université de Strasbourg

Rapporteurs :
M. Renaud Bachelot — Professeur, Université de technologie de Troyes
M. Serge Habraken — Professeur, Université de Liège

Autres membres du jury :
M. Bruno Serio — Professeur, Université de Paris Nanterre
M. Pascal Picart — Professeur, Université du Maine
M. Patrice Twardowski — Maître de conférences, Université de Strasbourg

Acknowledgements

During these three years, I have received a large number of help and assistance from my supervisors, colleagues, friends and family.

First, I would like to express my sincere gratitude to my supervisor Mr. Yoshitate Takakura who has guided my research. He has given me numerous valuable guidance for both my work and my life in France. I have learned a lot from his broad and profound knowledge in Optics, Mathematics and Experimental Techniques. However, the most important thing that I have learned from him is his conscientious and strict attitude towards Science. I will try my best to keep this attitude in my future professional life.

Then, I would like to thank my co-supervisor Mr. Patrice Twardowski. He has given me many important suggestions during my work. I have received a lot of help from him during the writing of my dissertation.

I would like to thank team TRIO and team leader Mr. Jihad Zallat for the technical and financial support of my research work. I should also acknowledge my team colleagues for their kind help and suggestions during my work. I would like to thank Mr. Jean Dellinger particularly for his help in fabricating 3D printed components and for letting me use the optical components in his lab.

Also, Mr. Nicolas Zimmermann of team MaCPV and Mr. Norbert Dumas of team SMH should be gratefully acknowledged for the deposition of gold film on the thin cover slip that generates the SPR effect.

I gratefully acknowledge, Mr. Renaud Bachelot, Mr. Serge Habraken, Mr. Bruno Serio and Mr. Pascal Picart for joining my defense committee. I would like to thanks Mr. Renaud Bachelot, Mr. Serge Habraken especially for being the *rapporteurs*, the reviewers of my manuscript. Thanks to every member of the committee for their time and attention.

I am also grateful to my old friends, Haoqing, Sen, Yifan and Yuchen. They have given me many useful advice for my work. The joyful recreations with them also allowed me to have a rest beside my research. I would also like to thank all my friends for the six years I spent in France, even 10 since me entering the university. Without their company and support, I could not have completed this dissertation.

In the end, I would like to express my deepest appreciation to my parents. During the extremely hard period of Covid and the protracted confinement, it would not have been possible for me to live through the tough time without their support. They have always been there to hearken my confides and complains. I could not thank them enough for their wise advice and encouragement and mental support.

Abstract

Objective based surface plasmon resonance microscopy (SPRM) is a label free technique which is suitable for real-time observations of biological and chemical activities on metal-dielectric interfaces. It has been applied for biological imaging, medical diagnostic, environmental monitoring and food industry. Its high resolution and sensitivity allow real time monitoring of antibody-antigen binding, and in-vivo adhesion observations of a single cell. Various phase imaging techniques have been combined with SPRM to further increase its sensitivity. Recently, an SPR digital holographic microscope (SPR-DHM) has been proposed which is capable of recording high resolution SPR phase images in real time. However, conventional SPRM and SPR-DHM require the utilization of extremely high numerical aperture (NA) objectives which are expensive and may hardly be accessible. In this thesis, we have designed and constructed a novel SPR-DHM which uses an 850 nm near infrared (NIR) laser diode instead of the commonly used visible laser as the SPR stimulation source. The utilization of such a source significantly reduces the requirements for the NA. An NA 1.42 objective which is cost effective has been employed. A common path off axis holographic configuration has been used for SPR holographic imaging. Such an NIR SPR-DHM has been tested by imaging the gold-air and gold-water interfaces. SPR holograms have been successfully recorded and reconstructed. The results show its potential for real time biological SPR phase imaging.

Table of contents

List of figures

Nomenclature

Acronyms / Abbreviations

$2D-SRNCP$ Two-dimensional phase-unwrapping algorithm based on Sorting by Reliability following a Noncontinuous Path

ATR Attenuated Total Reflection

BFP Back Focal Plane

$BL-ASM$ Band-Limited Angular Spectrum Method

CP Continuous Path

$DFT-FR$ Double Fourier Transform based Fresnel method

DoF Depth of Focus

EM Electromagnetic

FFP Front Focal Plane

$FWHM$ Full Width Half Maximum

GI Gini's index

$K-R$ Kretschmann and Raether

LED Light Emitting Diode

$LI-DHM$ Lensless Inline Digital Holographic Microscopy

MO Microscope Objective

$M-Z$ Mach-Zehnder

NA Numerical Aperture

NIR Near Infrared

OTF Optical Transfer Function

PVD Physical Vapor Deposition

RFT Robust two-dimensional phase unwrapping using a Fast cosine Transform

RI Refractive Index

RIU Refractive Index Unit

ROI Region of Interest

SFT − FR Single Fourier Transform based Fresnel method

SNR Signal to Noise Ratio

SoG Sparsity of Gradient

SPP Surface Plasmon Polariton

SPR Surface Plasmon Resonance

SPR − DHM Surface Plasmon Resonance-Digital Holographic microscopy

SPRi Surface Plasmon Resonance imaging

SPRM Surface Plasmon Resonance Microscopy

SPW Surface Plasmon Wave

TC Tamura coefficient

TIRF Total Internal Reflection Fluorescence

TM Transverse Magnetic

Chapter 1

General introduction

Surface plasmon resonance (SPR) is the resonance of collective oscillations of free electrons at the interface between negative permittivity material (metal) and positive permittivity material (dielectric). It could be considered as a surface wave that propagates along the interface. The SPR could be stimulated by an external electromagnetic (EM) wave and exhibits a strong absorption. This phenomenon was first observed by R.W Wood and reported in his publication in 1902 [1]. In 1968, A. Otto presented the first optical excitation method for non-radiative surface plasmon waves (SPW) based on the attenuated total reflection (ATR) and gave a theoretical explanation for the SPR absorption [2]. Later in the same year, E. Kretschmann and H. Raether independently proposed their ATR based SPR stimulation method [3]. Their prism-metal-dielectric configuration (K-R configuration) is still the most commonly used method for SPR sensing and imaging.

Begining from the 1980's, the SPR techniques have been applied for the biosensing. Since then, they have been used in various domains including medical diagnostic [4], environmental monitoring [5] and food industry [6]. The SPR sensing method is a highly sensitive label free method that is suitable for in-vivo detection. Its short penetration depth (hundreds of nanometers) makes it an ideal tool for detecting of surface oriented biological or chemical interactions.

The SPR imaging (SPRi) technique was firstly proposed in 1988 [7] based on the K-R configuration. It allows the two-dimensional imaging of SPR responses in real time. In 2007, Huang *et al.* introduced a novel widefield SPR microscope (SPRM) that replaced the coupling prism in the K-R configuration by a high numerical aperture microscope objective [8]. It has a much higher resolution than prism based SPR systems. Single cell in-vivo imaging has been achieved with such an objective based SPRM.

Phase responses of the SPR have higher sensitivities than its intensity counter parts. Since

the late nighties, numerous phase sensing methods have been combined with the SPRM including polarimetry, optical heterodying, interferometry and holographic methods. Among them, the holographic phase imaging method has the advantage of being able to retrieve phase information from a single acquisition. So it is ideal for real time in-vivo SPR phase imaging. In 2015, B. Mandracchia *et al.* proposed an SPR digital holographic microscope (SPR-DHM) which combines the objective based SPRM with Mach-Zehnder interferometer [9]. Later in 2017, J. Zhang *et al.* introduced their SPR-DHM using a Wollaston prism based holographic unit [10]. They have recently reported in-vivo observations of the cell-substrate adhesion gap using such a system [11].
Conventional SPR-DHM systems have the advantage of high resolution and high sensitivity. However, due to the large resonant angle of the SPR under visible light stimulation, extremely high numerical aperture (NA) are required for biological observations. Usually, special total internal reflection fluorescence (TIRF) (NA 1.49 or NA 1.65) objectives are needed. These objectives are expensive and not common in biological laboratories.
In this thesis, we propose a near infrared (NIR) SPR-DHM. An 850 nm NIR laser diode is used as the stimulation source instead of visible light. It could effectively reduce the resonant angle of the SPR. As a result a much cost effective NA 1.42 microscope objective could be chosen. Our NIR SPR-DHM has been tested to record phase responses with gold-air and gold-water interfaces. The main body of this manuscript has four chapters.

Chapter 2 In this chapter, principles of the DHM and SPR are introduced. We review the state of the art of SPR phase imaging and SPR-DHM. In the first section, we introduce basic physics of scalar wave diffraction theory. Then we present the digital holography theory and compare inline and off-axis holographic setups. Off-axis holography is selected for its real time imaging advantage. In the second section, physics of the SPR is addressed. Then the SPR stimulation theory and methods are presented. We explain that the NIR source could reduce the resonant angle. In the last section, by reviewing developments of SPR phase imaging, we have shown that the digital holographic method is suitable.

Chapter 3 In this chapter, we introduce the design of our SPR-DHM system. It could be divided into three parts: the illumination subsystem, the SPR stimulation and imaging subsystem and the holographic subsystem. The functionality and design of each system is introduced in detail. Some representative technical issues and their solutions are presented.

Chapter 4 This chapter is dedicated to the algorithms that have been applied for the digital holographic reconstruction. Due to the complexity of the SPR-DHM, these methods are first tested on a home-made lensless inline DHM (LI-DHM). The LI-DHM generally has a worse imaging quality than the off-axis DHM. So it is suitable to test the effectiveness and robustness of the chosen algorithms. Then, they are applied to the SPR-DHM. Based on the test result, we have concluded that auto-focusing may not be necessary for our SPR-DHM reconstruction.

Chapter 5 We present the experiment results of our system. The sample is a glass coverslip of about 85 µm coated with a 3 nm chrome (Cr) layer and a 45 nm gold (Au) layer. It is shown that the system could successfully stimulate SPR for gold-air as well as gold-water interfaces. We have first analyzed the intensity response and its spectrum distribution. Then, DHM images of gold-air and gold-water interfaces are captured and reconstructed. For the gold-water interface, a continuous acquisition has been proceeded to monitor the evaporation of a 5 µL water drop.

Chapter 2

Background introduction to surface plasmonic holographic microscope

2.1 Introduction to holographic imaging techniques

The holographic method was invented by D. Gabor in 1947 and published in 1948 [12]. It is a photographic technique based on the wave nature of light that enables the recording and reconstruction of a given light field complex distribution. He created the word 'holography' which originated from the Greek word 'holo' which means whole, for whole information and 'graphein' which means to write [13]. The technique was originally intended to be applied to increase the resolution of the electron microscope. His initial idea was to take a bad picture, an interference pattern of an electronic beam with the coherent background, and try to correct it by optical means. But the principle was tested with a monochromatic light source with a low coherence length at that time. The object captured in the first reported hologram was a set of opaque names – 'HUYGENS YOUNG FRESNEL' with transparent background [12]. The detailed theory and the reconstruction methods were introduced in his 1949 publication [14]. The obtained quality was not ideal because of the low source coherence and limitation of the 'inline' configuration. He reported that the 'ghost' or the 'conjugate image' (it is usually referred to as the twin image nowadays) deteriorates the reconstruction [15]. The invention of laser in 1960 promoted the development of modern optics rapidly. Its coherence permits recording of optical holograms. E. Leith and J. Upatnieks invented the off-axis holographic configuration in 1962 [16]. This configuration avoids the twin image effect in reconstruction by separating the readout wave from the reconstructed object wave. The reconstruction quality was dramatically improved as compared to the first holograms. Their presentation at the American Institute of Physics (AIP) has shaped the public perception

of hologram [17]. Later in 1971, D. Gabor was awarded the Nobel prize "for his invention and development of the holographic method" [18]. After the 1990s, thanks to the rapid development of digital imaging sensor, digitally recorded holograms became possible. Digital recording and reconstruction facilitate applications of holographic techniques and improve the reconstruction quality. Digital holographic imaging and microscopy have become a practical and efficient tools for biological imaging and industrial metrology.
In this chapter, the basic concept of scalar wave diffraction theory is introduced. Then the fundamentals of holography are described, including the on-axis (called also sometimes inline) and off-axis configurations, and their applications.

2.1.1 Electromagnetic wave theory of light

Holographic imaging is an imaging technique which encodes the object information using interference of light. Interference is a physical phenomenon that reveals the wave nature of light. The famous Maxwell equations include four differential equations to describe the physical behavior of an electromagnetic field. From his initial equations, Maxwell deduced that light is an electromagnetic field. His inference was proven by H. Hertz's experiment in 1888. In regions of space where both charge and current densities are zero, the Maxwell equations (SI units) in vacuum can be written as:

$$\nabla \cdot \mathbf{E} = 0 \tag{2.1a}$$

$$\nabla \cdot \mathbf{H} = 0 \tag{2.1b}$$

$$\nabla \times \mathbf{E} = -\mu_0 \frac{\partial \mathbf{H}}{\partial t} \tag{2.1c}$$

$$\nabla \times \mathbf{H} = \varepsilon_0 \frac{\partial \mathbf{E}}{\partial t} \tag{2.1d}$$

where $\mathbf{E}$ and $\mathbf{H}$ are the electric and magnetic fields, ∇ is the gradient operator, and μ_0 and ε_0 are the magnetic permeability and the electrical permittivity of free space. Taking the curl of the last two equations (Eqs. 2.1c, 2.1d), we derive the wave equation for the electric and magnetic fields:

$$\nabla^2 \mathbf{E} - \frac{1}{c^2} \frac{\partial^2 \mathbf{E}}{\partial t^2} = 0 \tag{2.2a}$$

$$\nabla^2 \mathbf{H} - \frac{1}{c^2} \frac{\partial^2 \mathbf{H}}{\partial t^2} = 0 \tag{2.2b}$$

where ∇^2 is the Laplace operator and $c = \frac{1}{\sqrt{\mu_0 \varepsilon_0}}$ is the speed of light in vacuum. In free space and most optical media, the vector wave equation is separable into scalar equations for each component of the electric and magnetic fields. Then each component of the electric and magnetic field vectors, i.e. (E_x, E_y, E_z, H_x, H_y, H_z) verifies the scalar wave equation [19]:

$$\nabla^2 U(P,t) - \frac{1}{c^2}\frac{\partial^2 U(P,t)}{\partial t^2} = 0 \tag{2.3}$$

where $U(P,t)$ represents any of the scalar field components, P and t denote to the spatial coordinates and temporal variable respectively.
A useful solution of the wave equation is the harmonic solution which corresponds to the case of monochromatic light and can be written in complex notation as:

$$U(P,t) = U(P)\exp(-j2\pi ft) \tag{2.4}$$

where $U(P)$ is the complex amplitude of the scalar wave at the position P, and f represents the optical frequency.
Substituting Eq. 2.4 into Eq. 2.3 we obtain:

$$(\nabla^2 + k_0^2)U(P) = 0 \tag{2.5}$$

where k_0 is the wave number, with $k_0 = 2\pi\nu/c = 2\pi/\lambda_0$ and λ_0 is the wavelength in vacuum. Eq. 2.5 is a time-independent scalar wave equation which in known as the Helmholtz equation.
For a non-absorbing and homogeneous medium, its refractive index n is defined as the ratio of the speed of light in vacuum c to that in the medium v

$$n = \frac{c}{v} \tag{2.6}$$

The wave number and the wavelength inside the medium are then given by:

$$k = nk_0 \tag{2.7}$$

$$\lambda = \lambda_0/n \tag{2.8}$$

And the Helmholtz equation becomes:

$$(\nabla^2 + k^2)U(P) = 0 \tag{2.9}$$

Considering the relative electric permittivity ε_r and the relative magnetic permeability μ_r in the medium, the refractive index can be written as:

$$n = \sqrt{\varepsilon_r \mu_r} \tag{2.10}$$

The electric permittivity and magnetic permeability in the medium verify

$$\varepsilon = \varepsilon_r \varepsilon_0 \tag{2.11}$$

$$\mu = \mu_r \mu_0 \tag{2.12}$$

For non-magnetic materials at optical frequencies, the relative permeability is very close to 1 and then

$$n \approx \sqrt{\varepsilon_r} \tag{2.13}$$

If we consider a non-magnetic material with absorption, the refractive index and relative permittivity can be defined as complex numbers with

$$\tilde{\varepsilon}_r = \varepsilon' + i\varepsilon'' \tag{2.14}$$

$$\tilde{n} = n + i\kappa \tag{2.15}$$

where κ is the extinction coefficient. In this dissertation, we study only the holographic process inside an isotropic, homogeneous, non-dispersive and non-magnetic medium, In order to simplify the discussion, in next subchapters, the optical wave is assumed to propagate inside vacuum, so $n = 1$, and $k = k_0$.

2.1.2 Scalar diffraction theory

The scalar diffraction theory is the fundamental tool for holographic imaging . It describes the propagation of scalar waves diffracted by an aperture. For holographic imaging, the object dimension is much larger than the wavelength, additionally the interference in the near field is not considered. So, the scalar wave diffraction theory is suitable to describe the hologram generation process. Also, it is an essential tool for the reconstruction process. The propagation of scalar wave satisfies the Helmholtz equation described in Sec. 2.1.1. In the following, rigorous solutions and their approximations will be introduced.

2.1.2.1 Rigorous solution of scalar diffraction

Kirchhoff formulation and Rayleigh-Sommerfeld formulation

In this part the Kirchhoff formulation, Rayleigh-Sommerfeld formulation and Angular Spectrum Method (ASM) will be briefly presented. Kirchhoff formulation and Rayleigh-Sommerfeld formulation share the same idea of using the Green's theorem to solve Eq. 2.9 through Helmholtz-Kirchhoff integral theorem. The Helmholtz-Kirchhoff integral theorem allows to express the field at any arbitrary position P_1 by the "boundary value" of the surface around it [19]:

$$U(P_1) = \frac{1}{4\pi} \iint_S \left(G \frac{\partial U}{\partial \vec{n}} - U \frac{\partial G}{\partial \vec{n}} \right) ds \tag{2.16}$$

U represents the scalar field; G is the so-called Green function. The integral surface is a closed surface which encloses point P_1. $\vec{n}$ is the unit normal vector of the surface S. For the Kirchhoff formulation, the Green's function G is selected as:

$$G = \frac{\exp(jkr)}{r} \tag{2.17}$$

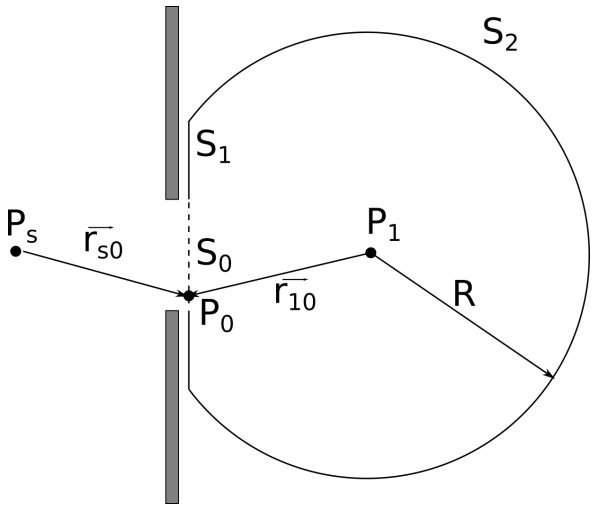

Fig. 2.1 Kirchhoff formulation of diffraction by a plane aperture. S_0 is the integral surface in front of the aperture, S_1 is the integral surface behind the edge of the aperture. S_2 is a semi-spherical surface. P_s is a point source, P_0 is a point at the opening of the aperture. P_1 is the point where the field needs to be calculated.

The most widespread model of scalar diffraction is the one that describes the diffraction by a plane aperture. As shown in Fig. 2.1, the light emitted by a point source P_s is diffracted by the aperture, so $U(P_0) = A\exp(jkr_{s0})/r_{s0}$. The point P_1 is enclosed by the surfaces S_0, S_1

and S_2. It has been proven that if the radius R of S_2 is large enough, the integration on S_2 would vanish. In order to calculate the integration on S_0 and S_1, Kirchhoff supposed that at the boundary S_0, the field U and its normal derivative would be the same as the field in the absence of the aperture. At S_1 the field U, along with its normal derivative, would be zero since it is blocked by the edge of the aperture. These two assumptions are the Kirchhoff boundary conditions. Applying these boundary conditions provides the Kirchhoff diffraction formula:

$$U(P_1) = \frac{jA}{2\lambda}\iint_{S_0}\frac{\exp[jk(r_{s0}+r_{10})]}{r_{s0}r_{10}}[\cos(\vec{n},\vec{r_{10}})-\cos(\vec{n},\vec{r_{s0}})]ds \tag{2.18}$$

This formulation gives good results which are remarkably consistent with experiment for the most situations, although it is not negligible that the theory is based on an inconsistency. Indeed, when a potential function and its normal derivative equal to zero on any finite surface, the function must be equal to zero in all space [19].
In order to solve this inconsistency Sommerfeld introduced alternative Green functions which do not need both U and $\frac{\partial U}{\partial \vec{n}}$ being zero simultaneously at the boundary. The alternative Green's functions are generated by the point P_1 and its mirroring point $P_1^{'}$ at the other side of the aperture. Here are the two Green functions which meet the requirement:

$$G_-(P_0) = \frac{\exp(jkr_{10})}{r_{10}} - \frac{\exp(jkr_{10}^{'})}{r_{10}^{'}} \tag{2.19a}$$

$$G_+(P_0) = \frac{\exp(jkr_{10})}{r_{10}} + \frac{\exp(jkr_{10}^{'})}{r_{10}^{'}} \tag{2.19b}$$

$r_{10}^{'}$ is the distance between the point P_0 and the mirroring point $P_1^{'}$. $G_-(P_0)$ and the normal derivative of $G_+(P_0)$ are equal to zero at surfaces S_0, S_1. As a result, U and $\frac{\partial U}{\partial \vec{n}}$ are not required to be zero at the same time, the previous inconsistency is solved. Substituting these two Green functions into Eq. 2.16 respectively, we can get the first and second Rayleigh-Sommerfeld solutions. Considering the model mentioned before, for a point source emitting light and diffracted by an aperture, the Rayleigh-Sommerfeld solutions are:

$$U(P_1)_I = \frac{jA}{2\lambda}\iint_{S_0}\frac{\exp[jk(r_{s0}+r_{10})]}{r_{s0}r_{10}}\cos(\vec{n},\vec{r_{10}})ds \tag{2.20a}$$

$$U(P_1)_{II} = -\frac{jA}{2\lambda}\iint_{S_0}\frac{\exp[jk(r_{s0}+r_{10})]}{r_{s0}r_{10}}\cos(\vec{n},\vec{r_{s0}})ds \tag{2.20b}$$

The Rayleigh-Sommerfeld solutions and the Kirchhoff solution have similar mathematical form. In this thesis dissertation, rather than the spherical wave diffraction, we focus more on the diffraction of a plane wave. The plane wave diffraction may be considered as the point source locates far away from the aperture. In Cartesian coordinates shown in Fig. 2.2, scalar diffraction on a point $P(x,y,d)$ behind the aperture can be written as [20]:

$$U(x,y,d) = \frac{1}{j\lambda}\iint_{-\infty}^{+\infty} U(x_0,y_0,0)\frac{\exp(jkr)}{r}K(\theta)dx_0dy_0 \tag{2.21}$$

$r = \sqrt{(x-x_0)^2+(y-y_0)^2+d^2}$ is the distance between the point P_0 aperture plane and the P_1 on the receiver plane. $K(\theta)$ is the obliquity factor, θ is the angle between the vector $\vec{r}$ and the vector $\vec{n}$. For each solution:

$$K(\theta) = \begin{cases} \frac{1}{2}[\cos(\theta)+1] & \text{Kirchhoff theory} \\ \cos(\theta) & \text{First Rayleigh} - \text{Sommerfeld solution} \\ 1 & \text{Second Rayleigh} - \text{Sommerfeld solution} \end{cases} \tag{2.22}$$

It should be mentioned that although the Rayleigh-Sommerfeld solutions permitted to avoid the inconsistency of the Kirchhoff's theory, it doesn't mean they are more accurate. Actually, in many circumstances, the Kirchhoff theory is more accurate than the Rayleigh-Sommerfeld solutions [21–24]. For a small object, deviation between these three approaches decreases significantly with increasing propagation distance [23]. When solving a practical optical imaging problem with paraxial approximation, θ is usually small enough so that all the three obliquity factors in Eq. 2.22 could be considered equal to 1.

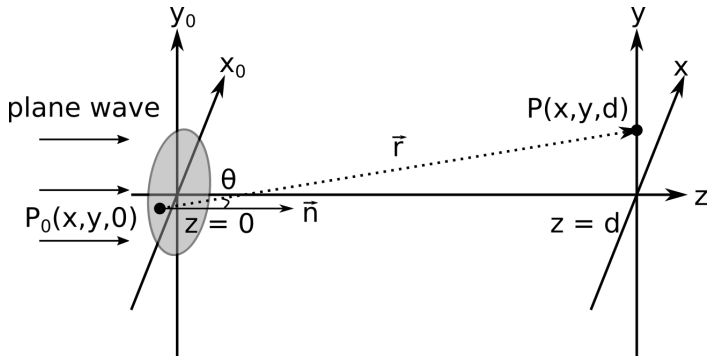

Fig. 2.2 Schematic representation of plane wave diffracted by a plane aperture with Cartesian coordinates. The aperture is located at the plane $z = 0$, the receiver at the plane $z = d$.

Angular Spectrum Method (ASM) for scalar diffraction

Kirchhoff theory and Rayleigh-Sommerfeld solutions are derived from the Eq. 2.9 for spatial domain. In this part, we consider the diffraction problem in the angular spectrum domain. Each point in the angular spectrum domain represents a plane wave which propagates along a specific direction. The amplitude is the complex amplitude of the corresponding plane wave. Considering the model shown in Fig. 2.2, the plane wave is diffracted by an aperture located at the plane $z = 0$ and the wave distribution on plane $z = d$ needs to be estimated. The angular spectrum $\hat{U}$ of a scalar field U is calculated by its Fourier transform:

$$\hat{U}(f_x, f_y; z) = \iint_{-\infty}^{+\infty} U(x, y, z) \exp[-j2\pi(f_x x + f_y y)] dx dy \tag{2.23}$$

The original field U is a combination of spectral components $\hat{U}(f_x, f_y)$ which can be calculated by inverse Fourier transform

$$U(x, y, z) = \iint_{-\infty}^{+\infty} \hat{U}(f_x, f_y; z) \exp[j2\pi(f_x x + f_y y)] df_x df_y \tag{2.24}$$

Substituting Eq. 2.24 into equation Eq. 2.9 provides:

$$\hat{U}(f_x, f_y; z) = \hat{U}(f_x, f_y; 0) \exp\left[j\frac{2\pi}{\lambda} z\sqrt{1 - (\lambda f_x)^2 - (\lambda f_y)^2}\right] \tag{2.25}$$

From Eq. 2.25, it can be concluded that the angular spectrum $\hat{U}(f_x, f_y; z)$ at position z is the angular spectrum $\hat{U}(f_x, f_y; 0)$ times a phase factor which is related to z. In conclusion, in the angular spectrum domain, the diffraction process may be described by a linear, invariant transform. The scalar wave distribution at plane z is the inverse Fourier transform of Eq. 2.25. In Eq. 2.25 we can find that only the spectrum component which satisfies $1 - (\lambda f_x)^2 - (\lambda f_y)^2 > 0$ could propagate to the target plane. The rest of the components are the so-called evanescent waves which exist only in the near field of the aperture. Their intensity decreases rapidly with the increase of the propagation distance.

Although the ASM is deduced from a very different aspect compared to the Kirchhoff formulation and the Rayleigh-Sommerfeld formulation, it has been proved that the solutions provided by the ASM are identical to the result calculated by second Rayleigh-Sommerfeld formulation [25].

2.1.2.2 Paraxial approximation - Fresnel diffraction formulation

Three solutions of the scalar diffraction problem have been introduced. But practically, these solutions are not the mostly used because of their mathematical complexity. The Fresnel approximation is the paraxial approximation. It is one of the employed diffraction formulation which can solve most of the problems in instrumental optics. The Fresnel approximation can be derived from all three approaches. Here, the approximation will be made from the Huygens-Fresnel principle which is identical to the second Rayleigh-Sommerfeld formulation of Eq. 2.21. Historically the Huygens-Fresnel principle was introduced by Fresnel. He created the mathematical expression for diffraction by combining the Huygens' construction with the interference theory. Replacing the $\cos(\theta)$ by d/r in Eq. 2.21, the Huygens-Fresnel principle is given as:

$$U(x,y,d) = \frac{d}{j\lambda}\iint_{-\infty}^{+\infty} U(x_0,y_0,0)\frac{\exp(jkr)}{r^2}dx_0dy_0 \tag{2.26}$$

with

$$r = \sqrt{d^2+(x-x_0)^2+(y-y_0)^2} \tag{2.27}$$

For the paraxial situation, the term in r^2 in the denominator can be replaced by d. The r inside the exponent is related to the high frequency oscillation, a small variation in r will introduce an large variation. It cannot be approximated by d directly for this reason. Applying the binomial decomposition to r and keeping only the first two orders, we obtain:

$$r \approx d\left\{1+\frac{(x-x_0)^2}{2d^2}+\frac{(y-y_0)^2}{2d^2}\right\} \tag{2.28}$$

This equation is valid when d is large enough. Replacing r in the exponent in Eq. 2.26 given:

$$U(x,y,d) = \frac{\exp(jkd)}{j\lambda d}\iint_{-\infty}^{+\infty} U(x_0,y_0,0)\exp\left\{\frac{jk}{2d}[(x-x_0)^2+(y-y_0)^2]\right\}dx_0dy_0 \tag{2.29}$$

Eq. 2.29 is the convolution form of the Fresnel approximation. Moving the terms that are independent of the integrating variables outside the integral, we get:

$$U(x,y,d) = \frac{\exp(jkd)}{j\lambda d}\exp\left[\frac{jk}{2d}(x^2+y^2)\right] \iint_{-\infty}^{+\infty}\left\{U(x_0,y_0,0)\exp\left[\frac{jk}{2d}(x_0^2+y_0^2)\right]\right\}\exp[-j2\pi(\frac{x}{\lambda d}x_0+\frac{y}{\lambda d}y_0)]dx_0dy_0 \tag{2.30}$$

This is the Fourier form of the Fresnel approximation. The diffraction field $U(x,y,d)$ is the Fourier transform of $U(x_0,y_{0,}0)\exp\left[\frac{jk}{2d}\left(x_0^2+y_0^2\right)\right]$, with spatial frequencies $f_x = \frac{x}{\lambda d}$, $f_y = \frac{y}{\lambda d}$.

2.1.3 The concept of digital holography

Holography is an interference imaging technique which can encode the amplitude and phase information in an interference pattern. In a typical holographic setup, light emitted by a coherent source is split into two. One of them illuminates the object. Depending on its nature, the scattered wave may either pass through the object or be reflected by its surface. This wave carries the information and is called the object wave. The other part of the wave will propagate directly to the detector where it interferes with the object wave. The recorded interference will create the hologram. In photographic holography, the analog hologram is recorded on a photosensitive film and fixed after a physico-chemical treatment. In this dissertation, we focus on digital holography. The hologram is recorded by a digital image sensor. The digitalized hologram allows reconstruction by a numerical approach. In addition numerous algorithms could be applied to increase the reconstruction quality [26–30].
The intensity of the hologram can be described by:

$$\begin{aligned} H(x,y) &= |R(x,y)+O(x,y)|^2 \\ &= |R(x,y)|^2+|O(x,y)|^2+R^*(x,y)O(x,y)+R(x,y)O^*(x,y) \end{aligned} \tag{2.31}$$

where $R(x,y)$ represents the reference wave, $O(x,y)$ is the object wave. The first two terms in the second line of Eq. 2.31 form the zero orders which represents the background of the hologram. The third and fourth terms carry the object information. For the sake of simplicity, the photoelectric conversion rate of the digital sensor is not taken into consideration. Eq. 2.31 is the hologram expression for a perfect monochromatic light. In the case of a

partial coherence source, a factor $\gamma(0 \leq \gamma \leq 1)$ that is related to coherency should multiply the two interference terms. To simplify, the light source is assumed to be perfectly coherent ($\gamma = 1$) in this chapter.
In photographic holography, the object wave $O(x,y)$ is reconstructed by lighting the hologram with the reference wave $R(x,y)$. In digital holography, it is realized digitally by multiplying the complex reference wave front with the recorded interference pattern. Reconstruction can be described as:

$$H(x,y)R(x,y) = \{|R|^2 + |O|^2\}R + O(x,y) + R^2(x,y)O^*(x,y) \tag{2.32}$$

The first term represents the influence of the zero order. The second term is the reconstructed object wave. The last term denotes the twin image which generates a distorted real image of object [13]. For a good reconstruction, the influence of the zero order and the twin image need to be minimized. The suppression of the zero order and twin image effect could be realized by a properly designed recording setup or computational approaches. Noticing that the reconstructed complex distribution $O(x,y)$ is the distribution at the sensor plane, it should be backpropagated to the object position using the scalar propagation methods. The selection of the propagation method depends on the design of the holographic setup.

2.1.4 Digital holographic imaging configuration and applications

Holographic imaging configurations will be briefly introduced here. They may be classified into two main categories: inline or on-axis and off-axis. The inline configuration, as indicated by its name, has the object wave and the reference wave propagating in the same direction. On the contrary, the object wave and reference wave for off-axis hologram arrive at the detector with an angle.

2.1.4.1 Inline digital holography setup

This holography technique was firstly developed by Gabor in 1948 [12]. The schematic representation of Gabor's inline setup is shown in Fig. 2.3. The sample is illuminated by a point source. The wave that is diffracted by the object is the object wave. The rest of the wave which is not diffracted serves as the reference wave. For classical Gabor inline setup, the object must be small enough, so that turbulence to the reference wave could be neglected.

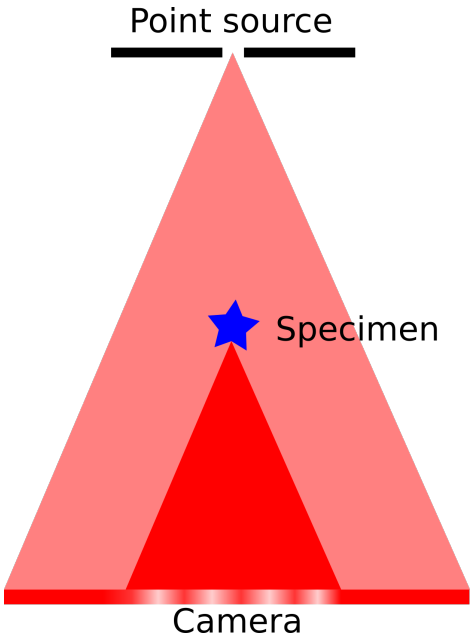

Fig. 2.3 The Gabor inline holography setup

Schematic representation of Gabor hologram reconstruction is shown in Fig. 2.4. The reconstruction is obtained after lighting the hologram with the reference wave. $O(x,y)$ is the object wavefront on the hologram plane. In order to reconstruct the object, this wavefront should be back propagated to the object plane using scalar diffraction formulation introduced in Sec. 2.1.2.

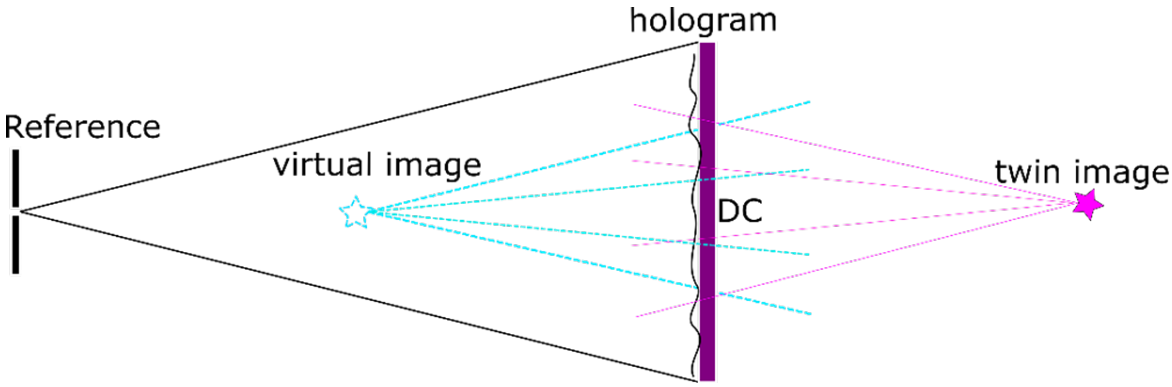

Fig. 2.4 Schematic representation of inline hologram reconstruction.

Because the object wave and the reference wave are inline, the virtual image, the twin image and the zero order (DC term) will overlap. Disturbance of DC term (zero order) and the twin image effect worsen the reconstruction in quality especially for phase hologram. The zero order is the sum of object and reference intensities. The intensity of the scattered wave is small enough comparing to the reference intensity [31]. It could be neglected in this case. The reference intensity could be recorded independently which can be easily subtracted from the hologram. However, suppression of the twin image effect remains a difficult task. In the second half of the last century, many researchers have worked on the suppression of the twin image for in inline holograms. The proposed solutions usually require additional acquisitions, either by displacing the object to another specific position [32] or using multiple wavelength illuminations [33]. Because of the difficulty and the complexity of removing the twin image effect for in inline holograms, the mainstream of optical holographic application was soon transferred to off-axis holography after its creation in 1962. However, after 2000 due to the rapid development of computational imaging techniques along with the technological improvement of digital cameras and modern computers, digital suppression of twin image effect become feasible [34–38]. Recently deep-learning techniques have been introduced for inline hologram reconstruction [39–41]. These methods show a very good performance both in quality and speed.

The Gabor inline setup which is also called as lensless inline holography setup, has become more and more popular during the last decade. First, it is extremely simple in structure. No optical lens is needed between the source and the sensor. From utterly short wavelength (electron wave) to extremely long wavelength (Terahertz to microwave), the Gabor setup may be widely applied [42–44]. Simplicity also means robustness in structure. It could be utilized under the extreme environment such as the undersea microorganism microscopic imaging [45]. Compact inline holographic microscopes have been built for in-field bio-medical

measurements [46, 47]. Secondly, because the object wave and the reference wave propagate along the same direction, path difference between them is small. The hologram can be easily generated with low coherence source such as light emitting diode (LED) [47, 48].
Despite of the advantages of the Gabor inline holography, its drawbacks also comes from its imaging mechanism. The object has to be small enough so as to reduce its influence on the reference wave. Because of this reason, Gabor holography is generally employed in microscopic domain. An independent reference wave is needed for imaging relatively large object as shown in Fig. 2.5.

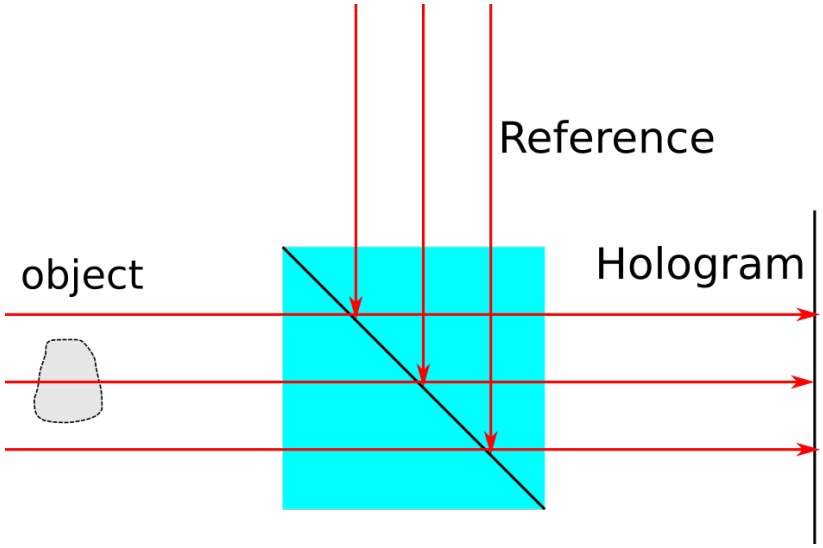

Fig. 2.5 Inline holography setup with independent reference wave.

2.1.4.2 Off-axis digital holography setup

Overlaps between the orders of Gabor inline holography have severely limited its application. The off-axis configuration invented by E. Leith and J. Upatrieks in 1962 solved this issue. The off-axis configuration is capable of spatially separating the orders. The authors successfully recorded a continuous-tone and a 3D solid objects which is not possible by inline setup back in that time [16, 49, 50]. The off-axis holography setup for transmissive samples is shown in Fig. 2.6. The coherent light source is separated by a beam splitter. The object wave passes through the transmissive object and arrives onto the sensor plane. The reference wave reaches to the sensor directly. The angle θ between the object wave and the reference wave is generated by the tilted beam splitter (see Fig. 2.6).

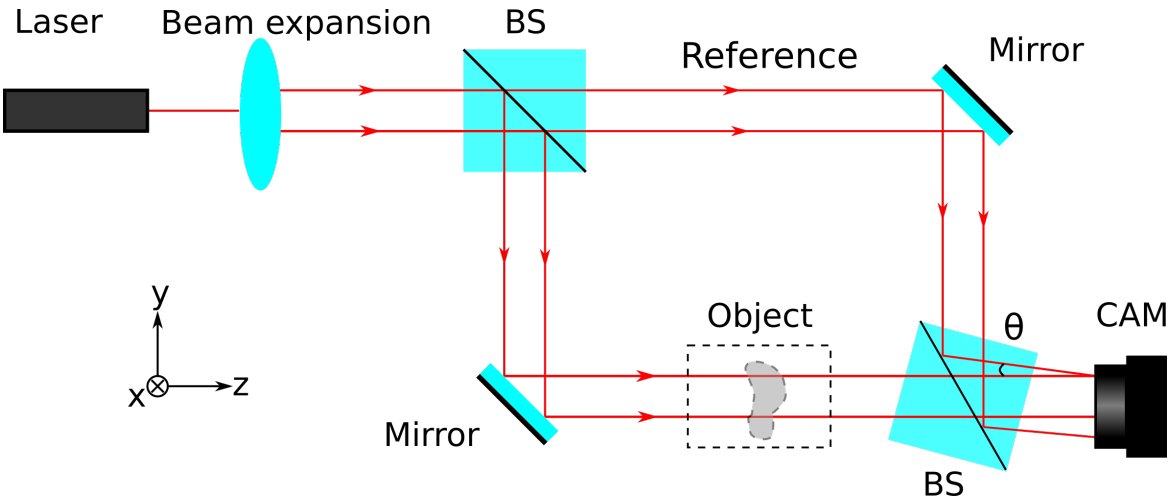

Fig. 2.6 Schematic representation of off-axis hologram recording setup with a transmissive sample. BS represents the Beam Splitter, CAM is the digital camera.

The object wave and reference wave arriving on the x-y camera plane are described by:

$$O(x,y) = O_0(x,y)\exp[-j\phi_0(x,y)] \tag{2.33}$$

$$R(x,y) = R_0\exp[-jk(\sin\theta)y] \tag{2.34}$$

The reference wave here is a plane wave, Its amplitude R_0 is a real constant in $x-y$ plane. The angle between its propagation direction and z axis is noted θ. The object wave $O(x,y)$ propagates along the z axis. The hologram intensity is written as:

$$H(x,y) = R_0^2 + |O(x,y)|^2 + O(x,y)R_0\exp[jk(\sin\theta)y] + O^*(x,y)R_0\exp[-jk(\sin\theta)y] \tag{2.35}$$

The hologram could be reconstructed with a light coming from the direction of the reference wave as shown in Fig. 2.7(a).

The reconstruction wave is

$$R'(x,y) = R'_0\exp[-jk(\sin\theta)y] \tag{2.36}$$

The reconstruction intensity R'_0 does not have to be identical with R_0. Here we take $R'_0 = 1$. We have:

$$\begin{aligned} H(x,y)R'(x,y) = {} & (R_0^2 + |O(x,y)|^2)\exp(-jky\sin\theta) \\ & + O(x,y)R_0 + O^*(x,y)R_0\exp(-jky\cdot 2\sin\theta) \end{aligned} \tag{2.37}$$

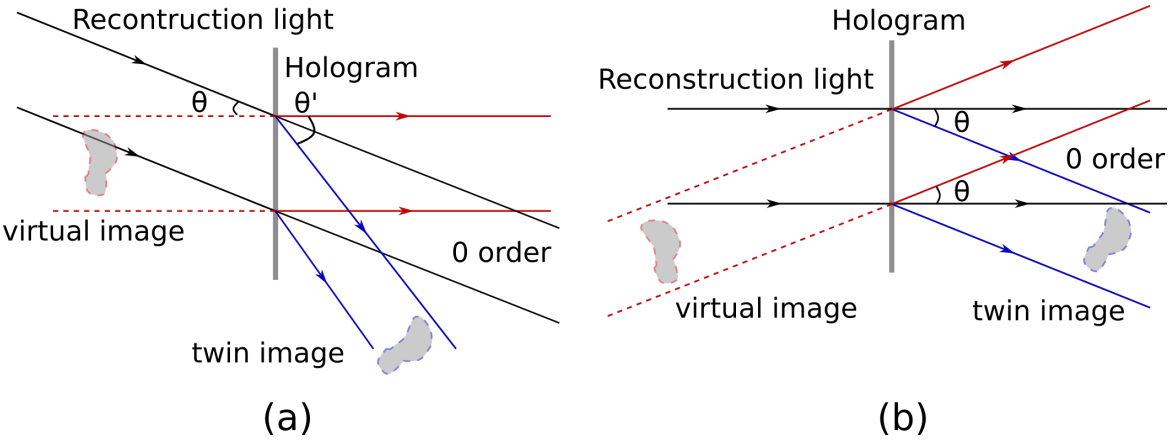

Fig. 2.7 Off-axis hologram reconstruction. (a) Reconstruction with light coming from the direction of the reference wave. (b) Reconstruction with a light wave normal to the hologram.

The first term in Eq. 2.37 is the zero order which propagates along the direction of reconstruction wave. The second term $O(x,y)R_0$ is the reconstructed virtual image of the object. R_0 is a real constant that does not modulate the spatial distribution of object wave $O(x,y)$. The latter propagates along the direction of the object wave vector. In the case of Fig. 2.7(a), this direction is normal to the hologram plane. The last term is the twin image. The angle between its propagation direction and z axis is $\theta' = \arcsin(2\sin\theta)$. The three terms are spatially separated, so that the disturbance of the zero order and the twin image is removed. Reconstruction with a light of normal incidence to the hologram is shown in Fig. 2.7(b). The three orders are also spatially separated. This means the reconstruction wave does not have to follow the same direction as the reference wave. Propagation direction of various waves will be altered according to the direction of the reconstruction. The order separation could be analyzed by the Fourier transform of the hologram distribution. The Fourier transform of Eq. 2.37 is given by:

$$\begin{aligned}\widetilde{H}(f_x,f_y) = {} & R_0^2\delta(f_x,f_y) + \widetilde{O}(f_x,f_y) * \widetilde{O}^*(f_x,f_y) \\ & + R_0\widetilde{O}(f_x, f_y - \frac{\sin\theta}{\lambda}) + R_0\widetilde{O}^*(-f_x, -f_y - \frac{\sin\theta}{\lambda})\end{aligned} \tag{2.38}$$

The zero order $R_0^2\delta(f_x,f_y) + \widetilde{O}(f_x,f_y) * \widetilde{O}^*(f_x,f_y)$ is the Fourier transform of the DC term. $R_0\widetilde{O}\left(f_x, f_y - \frac{sin\theta}{\lambda}\right)$ and $R_0\widetilde{O}^*\left(-f_x, -f_y - \frac{sin\theta}{\lambda}\right)$ are the +1 and -1 spectrum orders respectively.

The spectrum distribution of the Eq. 2.38 is shown Fig. 2.8. Assuming that the bandwidth of the object wave $O(x,y)$ is B, the bandwidth of the +1 and -1 orders will be B and the

bandwidth of the zero order will be $2B$ because of the self-convolution of the object wave.

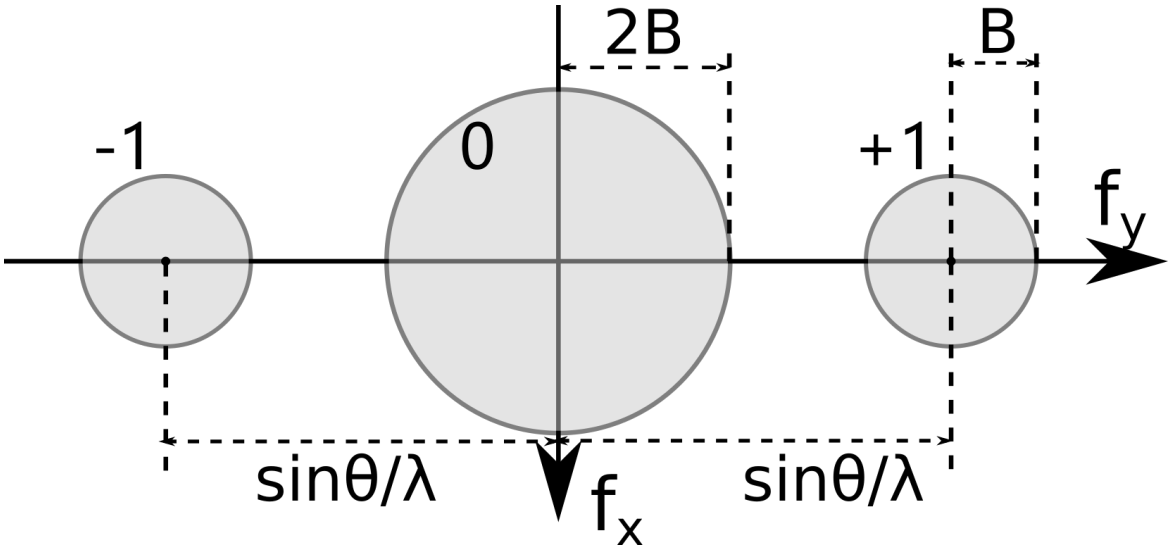

Fig. 2.8 The schematic representation of off-axis hologram spectrum.

With the aim of separating the zero order with the +1 and -1 orders the angle θ should satisfy:

$$\theta \geq \arcsin(3B\lambda) \tag{2.39}$$

For digital off-axis holograms, the maximum bandwidth of the hologram is limited by the pixel size p of the sensor according to the Shannon sampling theorem. The maximum frequency of the hologram is $1/2p$. As shown in Fig. 2.8, the maximum bandwidth of the hologram is proportional to $\sin\theta$. So, the angle θ should also satisfy the following constrain:

$$\frac{\sin\theta}{\lambda} + B \leq \frac{1}{2p} \tag{2.40}$$

In conclusion, in order to separate the orders and avoid aliasing, θ should satisfy:

$$\arcsin(3B\lambda) \leq \theta \leq \arcsin(\frac{\lambda}{2p} - \lambda B) \tag{2.41}$$

Comparing to other quantitative phase imaging (QPI) methods, off-axis holographic imaging have three advantages. Firstly, the object phase response is measured using a stable and a precise wavelength light source (Laser or LED) instead of a mechanical displacement of a reference or scanning [51]. This avoids measurement nonlinearities and calibration drift. Secondly, holographic imaging allows simultaneous multiplex imaging. The target can be

recorded with several wavelengths, phases, with different angles, or with several polarization states simultaneously [52]. Thirdly, the method allows high-speed acquisition, because only one acquisition is needed for reconstruction in the optimal situation.
Because off-axis holography solves the problem of order overlap, the complex response of the object could be unambiguously reconstructed by a single hologram [53]. It releases the potential of holographic imaging for real-time metrological applications. Due to its advantages comparing to other QPI methods, digital holographic imaging along with digital holographic microscope have been successfully applied to live cell imaging [52, 54], real-time metrological measurements including thermodynamic change, mechanical deformation and so on [51, 55, 56].
Off-axis holography also has its own disadvantages in comparison with Gabor inline configuration. Firstly, separating the object wave and the reference wave increases the complexity of the system. This will decrease the system stability and robustness. Also, the separating arms make the utilization of low coherency light source difficult. Common path off-axis holographic techniques have been introduced to solve this problem [57–60]. The second drawback is that off-axis holography is less efficient as for spatial bandwidth. As illustrated in Fig.2.8, the orders containing the effective information (+1 or -1 orders) only occupy less than one fourth of the total spectrum. It means, when using the same imaging sensor, the theoretical highest resolution for off-axis digital holography is less than ¼ of inline digital holography. Solutions have been proposed to increase the bandwidth-efficiency by multiplexing or optimizing the relative position of orders in the spectrum [53].

2.1.5 Digital holographic microscopy

Digital holographic microscopy (DHM) is a high-resolution quantitative phase imaging technique. The High resolution may be achieved by two approaches: optical approach, and computational approach. The optical approach is most realized by integrating a microscope objective into the off-axis digital holographic setup. Fig. 2.9 shows a typical off-axis DHM based on a Mach-Zehnder (M-Z) interferometer. In the object arm, light diffracted by the sample is captured by the microscope objective so as to acquire the high-resolution image. The object wave is then combined with the reference wave by a slightly tilted beam splitting cube. The interference between the object wave and the reference wave generates a hologram that is recorded by a digital imaging sensor. The complex response of the sample is encoded by the hologram. It can be retrieved by a reconstruction algorithm of off-axis holograms. With the help of the microscope objective, the lateral resolution of the DHM can reaches

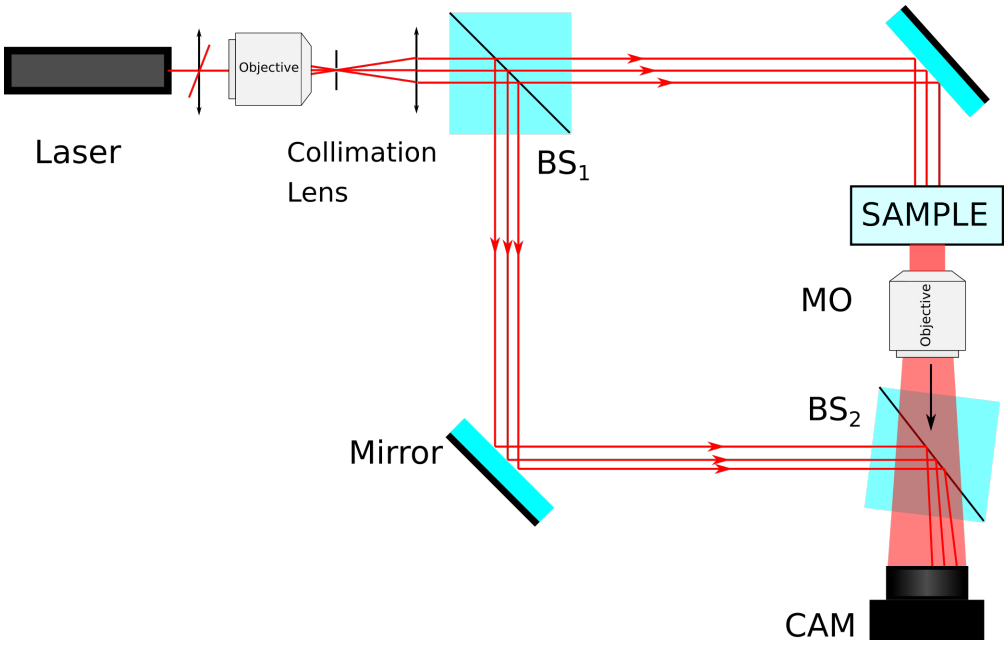

Fig. 2.9 Off-axis digital holographic microscope.

hundreds of nanometers. The axial resolution of several nanometers is also achievable. In addition to the advantage of such a high resolution, the off-axis DHM also has the advantages of off-axis holographic imaging. It is suitable for real-time phase imaging and in-vivo biological imaging. It has been applied for live cell imaging [54], biological tissue imaging [61], microorganism imaging [62], 3D particle tracking [63, 64], and real-time profile monitoring [65]. The all-in one off-axis DHM has become commercially available recently [66].

The second type of digital holographic microscope is realized by computational imaging techniques. For Gabor lensless inline holography, it is hard to increase its resolution by an optical approach. The associated computational approach allows a novel high-resolution phase microscope technique. Due to its simplicity in structure, computational super-resolution techniques are easily implemented including angular multiplexing [27, 47], wavelength multiplexing [67], focusing multiplexing [28]. As introduced before, deep learning implementation has also increased the image quality of lensless inline DHM. However, because the computational super-resolution methods need multiple acquisitions and time-consuming computation, real-time imaging remains a challenge for lensless inline DHM. These methods could also further increase resolution and SNR of off-axis DHM [53, 68].

2.2 Introduction to surface plasmon resonance

Surface Plasmon Resonance (SPR) is the collective resonant oscillation of free electrons at the interface between a metal (negative permittivity material) and a dielectric (positive permittivity material). It can be considered as a surface wave that propagates along the interface. This phenomenon was firstly observed by R.W. Wood in 1902 [1]. In this article he reported an abnormal absorption at the spectrum reflected by a metallic grating when the latter is illuminated directly by an incandescent lamp. In 1941, U. Fano suggested that the "anomalies" observed by Wood may be caused by a "quasi-stationary surface wave" [69]. But this abnormal absorption was not fully explained until the theory of surface plasmon was established. D. Pines introduced the word "plasmon" in 1956 as the quantum of plasma [70]. One year later, in 1957, R.H. Ritchie assumed the energy loss, occurring at a value which is less than the plasma energy when fast electrons hit a thin metal film, is related to the excitation of surface plasmon [71]. His assumption was validated and the theory of surface plasmon was established in the following works [72, 73]. In 1958, T. Turbadar reported his finding of "complete absorption of light by thin metal films" [74]. He discovered that when a p-polarized light impinges on an aluminum film (within a certain thickness range) coated on glass from the glass side, a sudden drop of reflectivity occurred after the critical angle. He successfully explained this reflectivity drop by using the thin film theory. But he didn't relate it to the surface plasmon. Ten years after, in 1968, A. Otto invented the optical excitation method for non-radiative surface plasmon waves (SPW) which also finally explained the phenomenon of reflectivity drop within the scope of SPR [2]. E. Kretschmann and H. Raether also reported their SPR excitation setup independently in the same year [3]. Their prism-metal film-dielectric configuration is still the most popular setup for SPR sensing nowadays.

In this section, basic physics and characteristics of surface plasmon waves will be introduced. The optical excitation theory of SPW and the SPR stimulation methods will be discussed next. The applications of SPR sensing and imaging will also be presented briefly.

2.2.1 Basic physics of SPW

Surface plasmon wave is a propagative wave bounded to an interface between metal and dielectric material. Fig. 2.10 represents schematically the propagation of SPW at the boundary between semi-infinite media. Though gold, silver copper and aluminum can all be employed as the metal medium, gold is the most commonly used medium for commercial biosensor application. Comparing to other materials, gold has a better chemical inertness, and more mature techniques for its bio-functionalization. As dielectric part, water and air are the most employed media for SPR applications. For biological applications of SPR, the samples (DNA, protein, cell) are immersed in aqueous solutions.

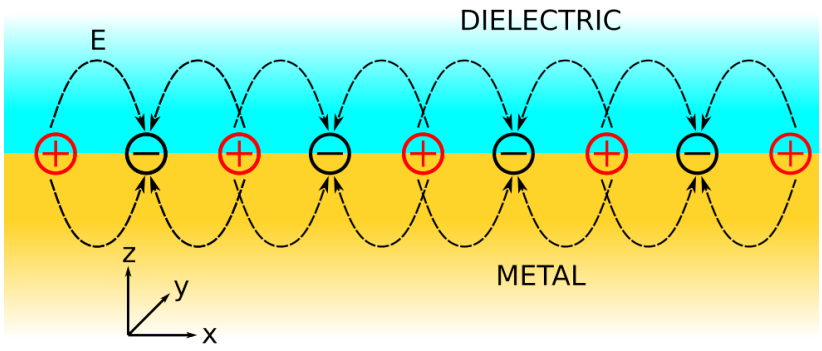

Fig. 2.10 TM-polarized surface plasmon wave propagating at the interface of semi-infinite dielectric and metal.

The wave vector of SPW can be obtained from the Maxwell equations. SPW can be excited from p-polarization (TM polarization) because of the discontinuity of the normal electric component induced by the surface charges [75]. In this case, the electric field and the magnetic fields are given respectively by:

$$\mathbf{E}_i = \begin{pmatrix} \mathbf{E}_{x,i} \\ 0 \\ \mathbf{E}_{z,i} \end{pmatrix} \exp[j(k_{x,i}x \pm k_{z,i}z - \omega t)] \tag{2.42}$$

$$\mathbf{H}_i = \begin{pmatrix} 0 \\ \mathbf{H}_{y,i} \\ 0 \end{pmatrix} \exp[j(k_{x,i}x \pm k_{z,i}z - \omega t)] \tag{2.43}$$

$k_{x,i}$ is the wave vector component along the interface. $k_{z,i}$ is the pure imaginary vector which represents the exponential decay into medium. ± indicates the positive and negative parts of z axis, inside metal '–' is taken. i denotes the medium (m for metal and d for the dielectric). ω is the angular frequency, $\omega = 2\pi f$. According to the boundary conditions:

$$\mathbf{E}_{x,m} = \mathbf{E}_{x,d} \tag{2.44a}$$

$$\mathbf{H}_{y,m} = \mathbf{H}_{y,d} \tag{2.44b}$$

$$\varepsilon_m \mathbf{E}_{z,m} = \varepsilon_d \mathbf{E}_{z,d} \tag{2.44c}$$

From Eq. 2.43 and Eq. 2.44b when $z = 0$, we obtain $k_x = k_{x,m} = k_{x,d}$.

The related Maxwell equation can be rewritten as:

$$\nabla \times \mathbf{H} = \mu\varepsilon \frac{\partial \mathbf{D}}{\partial t} + \mathbf{J} \tag{2.45}$$

The external current density J is equal to zero, $D = \varepsilon E$. Substituting Eq. 2.42 and Eq. 2.43 into Eq. 2.45, considering the x direction component we get:

$$jk_{z,m}\mathbf{H}_{y,m} = -j\omega\varepsilon_0\tilde{\varepsilon}_m\mathbf{E}_{x,m} \tag{2.46}$$

$$-jk_{z,d}\mathbf{H}_{y,d} = -j\omega\varepsilon_0\varepsilon_d\mathbf{E}_{x,d} \tag{2.47}$$

From the Eq. 2.44a, Eq. 2.44b, Eq. 2.46 and Eq. 2.47 we get:

$$\frac{k_{z,d}}{\varepsilon_d} + \frac{k_{z,m}}{\tilde{\varepsilon}_m} = 0 \tag{2.48}$$

The wave vector verifies the following equation:

$$k^2 = k_x^2 + k_{z,i}^2 = \tilde{\varepsilon}_i \left(\frac{\omega}{c}\right)^2 \tag{2.49}$$

The tangential wave vector k_x is given by:

$$k_x = \frac{\omega}{c}\sqrt{\frac{\varepsilon_d\tilde{\varepsilon}_m}{\varepsilon_d + \tilde{\varepsilon}_m}} \tag{2.50}$$

The relative permittivity of metal is defined as $\tilde{\varepsilon}_m = \varepsilon'_m + i\varepsilon''_m$. The permittivity of the dielectric medium can be regarded as a pure real positive number ε_d. Assuming that $|\varepsilon'_m| > \varepsilon''_m$

(which can be fullfilled when using gold as metal media $\varepsilon_m^{'} < 0, \varepsilon_m^{"} > 0$), we can get:

$$k_x = k_x^{'} + ik_x^{"} \approx \frac{\omega}{c}\sqrt{\frac{\varepsilon_m^{'}\varepsilon_d}{\varepsilon_m^{'}+\varepsilon_d}} + i\frac{\varepsilon_m^{"}}{2(\varepsilon_m^{'})^2}\frac{\omega}{c}\left(\frac{\varepsilon_m^{'}\varepsilon_d}{\varepsilon_m^{'}+\varepsilon_d}\right)^{3/2} \tag{2.51}$$

$$\Re(k_x) = \frac{\omega}{c}\sqrt{\frac{\varepsilon_m^{'}\varepsilon_d}{\varepsilon_m^{'}+\varepsilon_d}} \tag{2.52}$$

$$\Im(k_x) = \frac{\varepsilon_m^{"}}{2(\varepsilon_m^{'})^2}\frac{\omega}{c}\left(\frac{\varepsilon_m^{'}\varepsilon_d}{\varepsilon_m^{'}+\varepsilon_d}\right)^{3/2} \tag{2.53}$$

The normal component $k_{z,i}$ can be calculated by:

$$k_{z,i} = \sqrt{(\frac{\tilde{n}_i\omega}{c})^2 - k_x^2} \tag{2.54}$$

$$k_{z,i} = k\sqrt{\frac{\tilde{\varepsilon}_i^2}{\tilde{\varepsilon}_m+\varepsilon_d}} \tag{2.55}$$

$\tilde{\varepsilon}_i = \varepsilon_d$ in the dielectric medium.

2.2.1.1 Propagation distance

Because of the existence of a non-zero imaginary part in k_x, the SPW is attenuated with the propagation distance. The propagation distance of SPW when its energy decreases to 1/e can be described as:

$$L_x = 1/2|\Im(k_x)| \tag{2.56}$$

From Fig. 2.11, it can be noticed that the SPW only exists if the excitation wavelength is longer than a critical wavelength for each type of metal. This critical wavelength is ruled by the plasma (Drude) frequency of the used metal [78].

$$\omega_p = \sqrt{Ne^2/(\varepsilon_0 m_e)}. \tag{2.57}$$

where N is the concentration of free electrons, e is the electron charge and m_e is the effective mass of electron.

Generally the propagation distance of SPW increases with wavelength. For example, for gold-water combination the calculated L_x increases from 1.7 μm to 38 μm within the wavelength

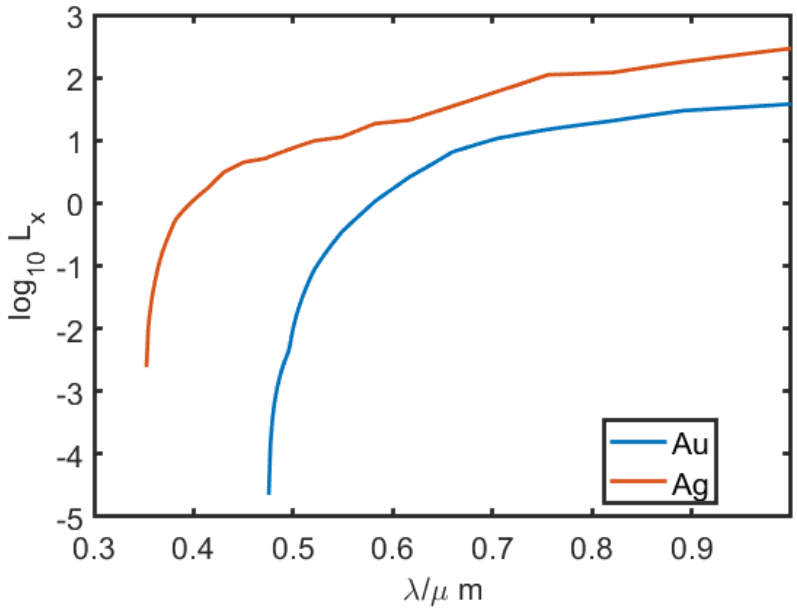

Fig. 2.11 Propagation distance of SPW along the interface of gold-water and silver-water as a function of wavelength. Refractive index of materials taken from [76] and [77].

range of 600 nm to 1000 nm. The lateral propagation distance L_x is one of the main issues which limit the lateral resolution of wide field SPR microcopy.

2.2.1.2 Penetration depth

The intensity in z direction is proportional to $\exp(-2|k_{zi}||z|)$. We define the penetration depth as the distance from the interface where the intensity is attenuated to $1/e$:

$$L_{z,i} = 1/2|\Im(k_{z,i})| \tag{2.58}$$

i represents the medium into where SPW penetrates. Different from the lateral propagation distance, which is the same in both media, the penetration depth depends on the material. Fig. 2.12 shows that SPW penetrates much deeper inside dielectric than metal. For a gold-water structure, we have calculated that SPW can penetrate 198 nm into water comparing to 12 nm into metal at 850 nm wavelength. From Fig. 2.13 we observe that the penetration depth increases with excitation wavelength in dielectric and decrease slightly inside metal. The penetration depth $L_{z,d}$ in dielectric limits the sensitive distance from the interface where SPR is able to detect.

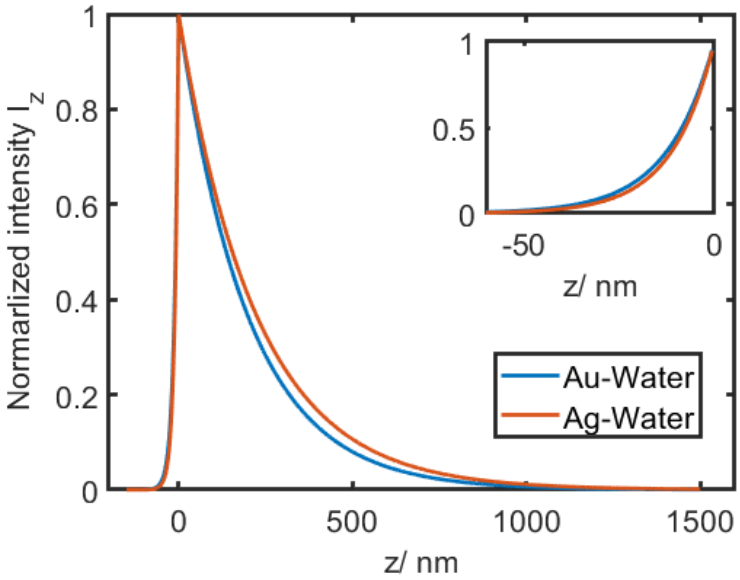

Fig. 2.12 Normalized itensity of SPW on z direction at Au-Water and Ag-Water interfaces. The excitation wavelength is 850 nm. Inset: magnification on metal part ($z < 0$).

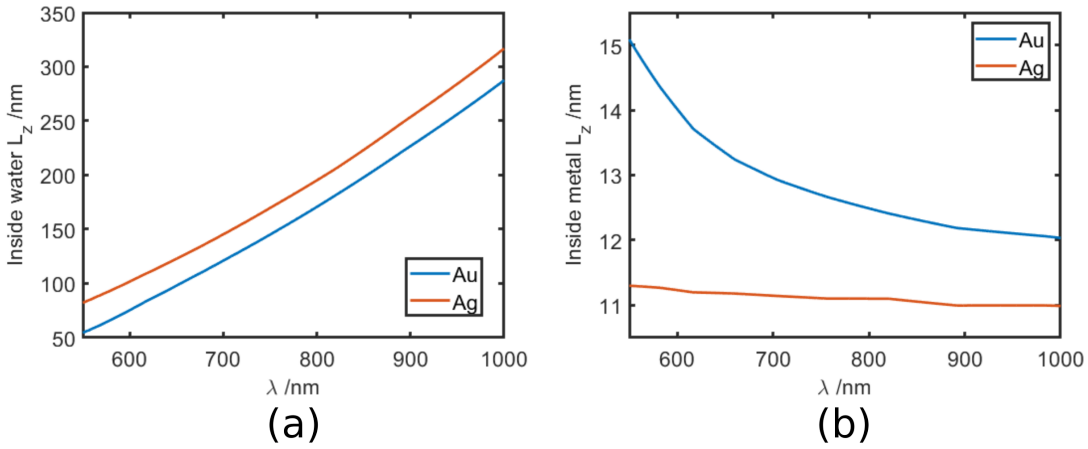

Fig. 2.13 Penetration depth of SPW as a function of wavelength. (a) into water (b) into metal.

Because of the limited $L_{z,d}$ value, SPR measurements must be considered in two typical situations. In the first situation, the sample is a bulk solution, or the target layer thickness is far larger than the $L_{z,d}$ length. In the second situation, the sample is a thin film as shown in Fig. 2.14, which has a thickness smaller the $L_{z,d}$. The latter is a commonly seen case when using a protein solution. The protein moleculars will be adsorbed onto the gold surface then forming an adsorbate layer. The thickness is usually less than 100 nm. SPW can penetrate through the adsorbate layer, the response is influenced by both the sample and the solvent.

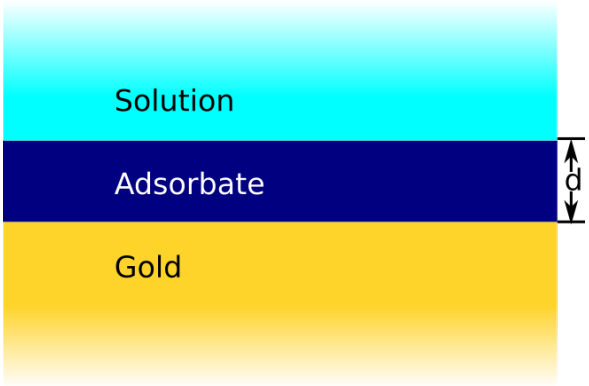

Fig. 2.14 Schematic diagram of limited thickness adsorbate layer. Thickness d is less than the penetration depth of SPW. SPW can penetrate throughout the adsorbate.

In this case the refractive index of dielectric needs to be replaced by an effective refractive index n_{eff} [79],

$$n_{eff} = (2/L_{z,d}) \int_0^\infty n(z) \exp(-2z/L_{z,d}) dz \tag{2.59}$$

where $n(z)$ is the refractive index at height z. When the sample has only two uniform layers as shown in Fig. 2.14, Eq. 2.59 can be simplified as:

$$n_{eff} = n_s + (n_a - n_s)[1 - \exp(-2d/L_{z,d})] \tag{2.60}$$

$L_{z,d}$ is the SPW penetration depth into the semi-infinite medium, n_a and n_s are the refractive index of the adsorbate layer and solution respectively.

2.2.2 Optical stimulation of SPR

From Eq. 2.53 we know that the phase velocity of SPW is always smaller than the one of plane wave in the dielectric. So it is not possible to optically stimulate the SPR in a simple Metal-Dielectric structure without a specific configuration. Generally, there exists two categories of stimulation. The first category is the attenuated total reflection (ATR) method which couples the stimulation light from a third medium. The third medium has a higher refractive index than the dielectric. In this way, the stimulation light may have a component with lower phase velocity. The second category utilizes a grating. When the scattered diffraction matches a resonance condition, the SPR is stimulated.

2.2.2.1 Prism coupling

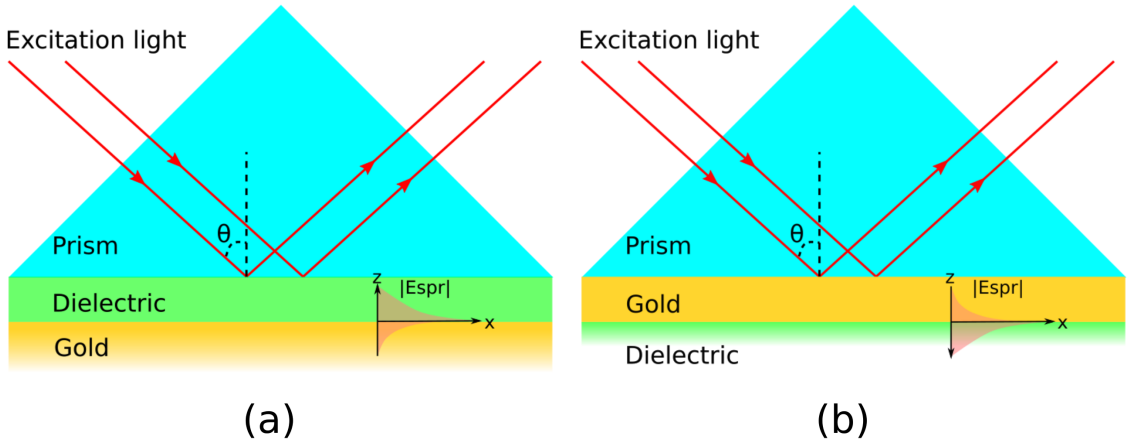

Fig. 2.15 Schematic representation of a prism coupling setup (a) Otto configuration, (b) Kretschmann-Raether (K-R) configuration.

A. Otto published the Prism-Dielectric-Metal configuration (Otto configuration) in 1968. It contains a glass prism, a thin dielectric film with a well-selected thickness and the semi-infinite metal layer. The p-polarized light is incident at an angle larger than the critical angle of glass-dielectric interface. The evanescent wave will penetrate through the thin dielectric film. The glass prism has a higher refractive index than the dielectric film, so the evanescent wave coming from the prism could have a smaller phase velocity than the plane wave in dielectric material. The phase velocity in x direction is controlled by the incident angle of light. When it meets the resonant condition, the SPW will be excited at the dielectric-metal interface. The resonant condition may be deducted by Fresnel theory which will be introduced in Sec. 2.2.4.

In the same year, E. Kretschmann and H. Raether published the prism-metal-dielectric configuration. The K-R setup shares the same idea of utilizing total internal reflection. The evanescent wave travels through the thin gold layer then excites SPW at the gold-dielectric interface. The coating techniques for gold layer on glass prism are far easier and more mature than creating a thin dielectric film (which is usually a liquid layer). Also, the K-R configuration is more stable and rigid than the Otto structure, which makes it easier to be used for various applications. After the invention of the K-R setup, the SPR sensing techniques and its applications started growing rapidly.

2.2.2.2 Objective coupling

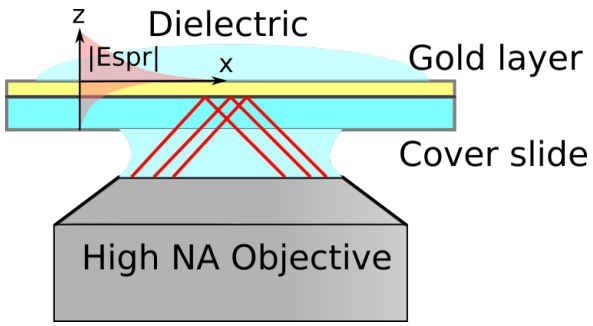

Fig. 2.16 Objective SPR coupling configuration.

The objective coupling method shown in Fig. 2.16 was firstly proposed by Huang *et al.* in 2007 [8]. It is based on the prism-metal-dielectric structure using the ATR method. Instead of coupling the stimulation light by a prism, a high NA oil immersed objective is used. The illumination light is focused on the back focal plane (BFP) of the high NA objective. The light is collimated by the same objective and impinges onto the interface as a parallel wave. Its incident angle is controlled by the lateral focusing position at the BFP. Compared to the K-R configuration, the objective coupling method provides a much higher magnification and resolution for SPR imaging. The image distortion induced by the prism is also avoided.

2.2.2.3 Waveguide coupling

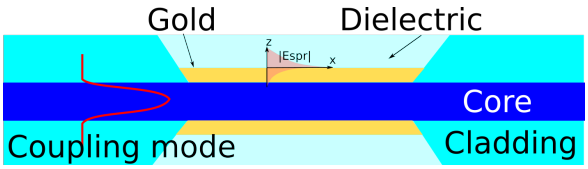

Fig. 2.17 Waveguide SPR coupling configuration

The waveguide coupling method using an optical fiber was introduced by R.C. Jorgenson and S.S. Yee in 1993 [80]. It is also a variation of ATR methods. Fig. 2.17 shows a SPR sensor based on an optical fiber. A part of the cladding is removed to expose the core. A thin layer of metal is then coated on the exposed part. This fraction of treated fiber is immersed into the sample solvent. The core has a higher refractive index than the sample solvent which meets the requirement of ATR methods. When a guided mode arrives at the treated part, SPR will be stimulated.

2.2.2.4 Grating coupling

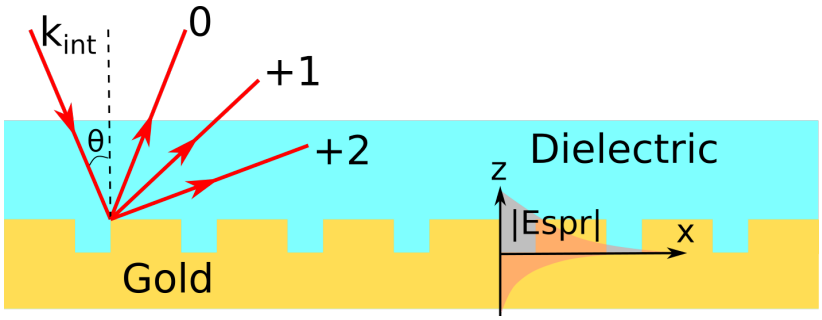

Fig. 2.18 Grating SPR coupling configuration.

The first observation of SPR phenomenon was reported by Wood using a grating in 1902 [1]. However, the application of grating coupling was not realized until 1980s [81]. The principle of reflective grating coupling method is shown in Fig. 2.18. Stimulation light illuminates the surface of the grating. The higher diffraction orders have larger wave number than the incident plane wave. By adjusting the incident angle or the incident wavelength, the diffraction light may be coupled into the SPW.

2.2.3 Theory of Attenuated Total Reflection (ATR)

Prism coupling, objective coupling and waveguide coupling introduced previously are all based on the attenuated total reflection method. They share the same principle of coupling evanescent waves inside to the metal-dielectric interface to stimulate the SPR. In this work, the objective coupling method has been selected for the SPR microscopy. The theory of ATR method is introduced here.

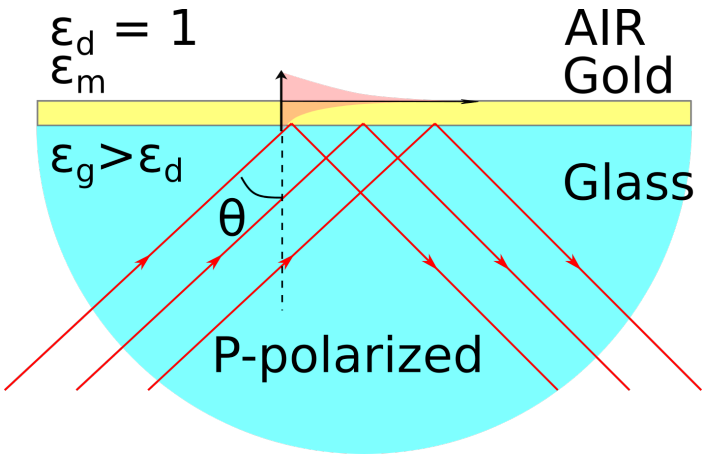

Fig. 2.19 Schematic representation of a K-R type three layers SPR stimulation model.

2.2.3.1 Resonant angle for the ATR method

We consider a three layer K-R model as shown in Fig. 2.19. The SPR is stimulated at the air-gold interface. The evolution of dispersion as a function of k_x is shown in Fig. 2.20. The dispersion curve of SPR is calculated by Eq. 2.50. The permittivity of gold $\tilde{\varepsilon}_m$ is approximated by the Drude perfect metal model [82]. The permittivity is governed by three coefficients ε_0, ω_p and Γ, where ω_p is the plasma frequency of metal, Γ is proportional to the electron relaxation time. The solid red line in Fig. 2.20 represents the dispersion of light in air $\omega = ck$. It could be observed that the SPR curve and the dispersion curve in air have only one common point which locates at the $k_x = 0$. It proves that SPR could not be stimulated by a simple metal-dielectric structure as mentioned before. In an ATR based configuration as shown in Fig. 2.19, a third dielectric material is needed. This material should have a higher refractive index than the dielectric of interface. The dispersion inside this material is $\omega = ck/n$. It has a second crosspoint with SPR curve different from $k = 0$, so SPR could be stimulated. The dispersion curve (3) in Fig. 2.20 corresponds to a light impinging with an incident angle of θ, dispersion relation $\omega = ck\sin(\theta)/n$. The crosspoint is then controlled

by θ. The resonance relation of the ATR method is given by:

$$k_{x,g} = \Re(k_{x,spr}) \tag{2.61}$$

$$\sqrt{\varepsilon_d}\sin(\theta) = \Re\left(\sqrt{\frac{\tilde{\varepsilon}_m \varepsilon_d}{\tilde{\varepsilon}_m + \varepsilon_d}}\right) \tag{2.62}$$

$k_{x,g}$ is the x directional component of the wave vector inside the prism. From Eq. 2.62 we can get the resonant angle as a function of the excitation wavelength. The angle decreases as the excitation wavelength increases.

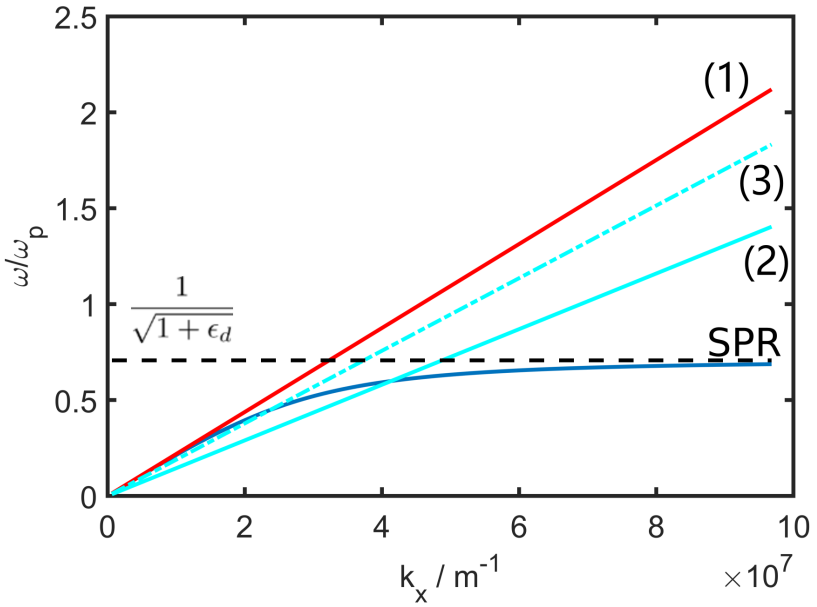

Fig. 2.20 Dispersion relation of SPR. Solid blue line is the dispersion for SPR at metal-dielectric interface. Here the dielectric is air $\varepsilon_d = 1$ and the metal is gold. The straight solid red line (1) represents the dispersion of light for air $\omega = ck$. The solid cyan line (2) is the dispersion for the coupling material: the glass prism. It follows the equation $\omega = ck/n$. And the dotted cyan line (3) representqtive of the incoming light from the glass prism with an incident angle of θ.

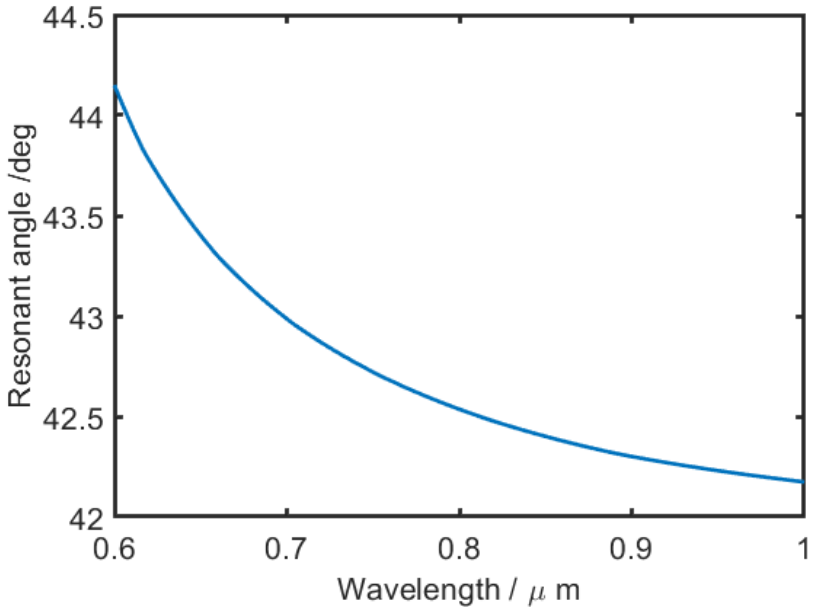

Fig. 2.21 Stimulation angle of SPR as a function of the excitation wavelength. The curve is drawn based on an NBK-7-gold-air setup.

2.2.4 Reflectivity for the ATR method

The reflectivity can be calculated from Fresnel equations. In a practical SPR application, a thin layer of Cr or Ti is coated between gold and glass, since the adhesion of Au on SiO2 is not ideal. Moreover, additional layers can be coated to increase the performance of SPR sensors. The SPR sensor has a stratified structure. The matrix method for N-layers stratified medium is suitable for its reflectivity calculations [83, 75]. The schematic representation of light transmission inside a N-layers stratified medium is shown in Fig. 2.22. We consider the $z_{i-1} \leq z \leq z_i$ layer as an isotropic layer. The light is reflected ,refracted and transmitted at each interface.

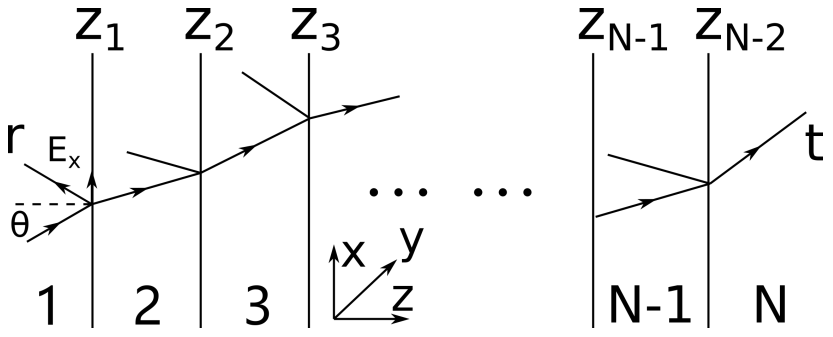

Fig. 2.22 Transmission and reflection in a stratified medium.

In the matrix formulation, each material is represented by a characteristic matrix M_i is given by:

$$M_i = \begin{bmatrix} \cos\beta_i & \frac{-j}{q_i}\sin\beta_i \\ -jq_i\sin\beta_i & \cos\beta_i \end{bmatrix} \tag{2.63}$$

where

$$q_i = (\mu_i/\tilde{\varepsilon}_i)^{1/2}\cos\theta_i \tag{2.64}$$

$$\beta_i = \frac{2\pi}{\lambda_0} n_i \cos\theta_i (z_i - z_{i-1}) \tag{2.65}$$

From the Snell's law, we know that

$$\cos\theta_i = \sqrt{1 - \frac{n_1^2}{\tilde{\varepsilon}_i}\sin^2\theta_1} \tag{2.66}$$

For the study of SPR microscopy, we focus on reflections of p-polarized waves. The tangential components are given by:

$$U_i = H_y = H_y^T + H_y^R \tag{2.67}$$

$$V_i = E_x = E_x^T + E_x^R \tag{2.68}$$

Relation between the tangential components of light at the first ($z = z_1$) and the last boundary($z = z_{N-1}$) are given by:

$$\begin{bmatrix} U_1 \\ V_1 \end{bmatrix} = M_2 M_3 \cdots M_{N-1} \begin{bmatrix} U_{N-1} \\ V_{N-1} \end{bmatrix} = M \begin{bmatrix} U_{N-1} \\ V_{N-1} \end{bmatrix} \tag{2.69}$$

M is the characteristic matrix of the system which is calculated by multiplying characteristic matrices.

$$M = \prod_{i=2}^{N-1} M_i = \begin{bmatrix} m_{11} & m_{12} \\ m_{21} & m_{22} \end{bmatrix} \tag{2.70}$$

Knowing the complex refractive index of each layer, the reflectivity r of p-polarized light could be easily calculated.

$$r_p = \frac{(m_{11} + m_{12}q_N)q_1 - (m_{21} + m_{22})q_N}{(m_{11} + m_{12}q_N)q_1 + (m_{21} + m_{22})q_N} \tag{2.71}$$

$$R_p = |r_p|^2 \tag{2.72}$$

$$\phi_p^r = \arg(r_p) \tag{2.73}$$

r^p is the complex reflectivity. R_p is the reflectivity for the intensity. ϕ_p^r is the phase shift produced by the reflection.

The reflectivity of the s-polarized light can be calculated by replacing q_i by p_i:

$$p_i = \sqrt{\tilde{\varepsilon}_i/\mu_i}\cos\theta_i \tag{2.74}$$

From these equations, the SPR reflectance curve is calculated as illustrated in Fig. 2.23. Resonance occurs after the critical angle. It will absorb most of the incident energy, a strong attenuation could be observed when SPR is stimulated. This attenuation phenomenon gives its name to the attenuated total reflection (ATR) methods. It could be observed from this figure that the resonant angle decreases as the excitation wavelength increases.

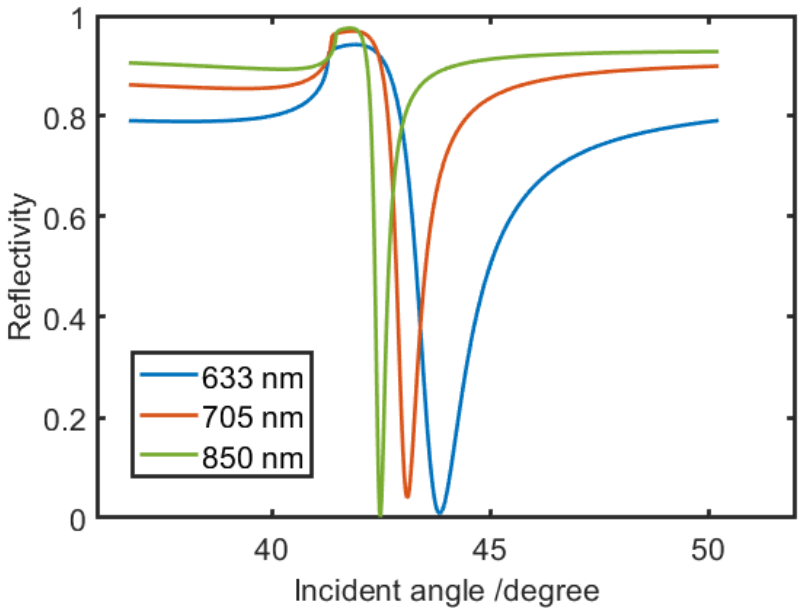

Fig. 2.23 Amplitude reflectivity of a glass-gold (45 nm)-air structure for different excitation wavelengths.

2.2.5 Surface plasmon resonance sensing and imaging

2.2.5.1 Surface plasmon resonance sensing

Surface plasmon resonance sensing is a label free detection method which is surface oriented [84]. It does not need any additional labelling treatment using the fluorescence or radioactive materials which may impair the binding [85]. As introduced before the penetration depth of the SPW is around hundreds of nanometers in dielectric materials. This makes it an ideal tool for surface affinity detections. Thanks to its short penetration depth, the background noise could be avoided.

In 1983, B. Lieberg *et al.* introduced the first application of SPR in biosensing [86]. They successfully monitored gas concentrations and the antibody adsorptions by a silver coated K-R setup. Soon after the first biological application, the first commercial SPR sensor (Biacore) was launched on the market in 1990. Since then, the SPR publications start increase rapidly. Until now, SPR techniques have become a popular tool for the detection of DNA, hormones, proteins, antibodies, and virus [87]. They have also been applied for environmental monitoring and food industry [88, 89].

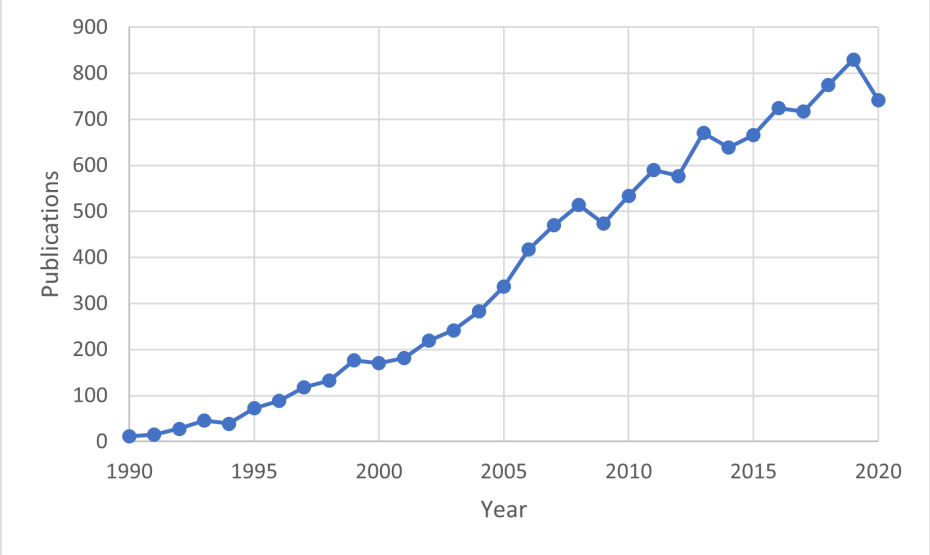

Fig. 2.24 Evoluation of the number of paper related to SPR. Data collected from Web of Science [90].

2.2.5.2 Prism based surface plasmon resonance imaging

In 1988, B. Rothenhausler and W. Knoll introduced the first SPR imaging setup [7]. The optical sensors was replaced by a camera and achieved 2D imaging of a SPR interface for the first time. The setup was based on a silver coated K-R configuration. The sample was a thin layer of dielectric film coated on silver. The large field of view allowed a multichannel parallel detection. Planted multiple sites of sensing on the metal surface (gold for most situations), combined with the well-designed micro-fluid channel, have permitted to manufacture of high throughput SPR sensors [91].
Other than the detection of molecules, SPR imaging also makes the SPR technologies applicable to the cell imaging. A. W. Peterson *et al.* used SPRi techniques to observe cell activities in vivo. Due to the short penetration depth, SPRi is suitable to monitor cell-substrate interactions at the substrate surface [92]. Being a label free method means the SPRi could observe cells in their natural environment without disturbance.

2.2.5.3 Objective based surface plasmon resonance microscopy

Wide-field SPRM As introduced, the K-R configuration is the first and mostly commonly used method for SPR imaging. However, though the utilization of prism facilitates SPR coupling, it limits the image resolution. In order to capture the image at the interface from the exit plane of prism, a long working distance objective or a lens is necessary which have a limited magnification. S. Stabler *et al.* solved this issue by replacing the prism by a high numerical aperture (NA) objective. The angle of excitation is controlled by defocusing the objective [93]. Later in 2007, Huang *et al.* introduced the more commonly used setup [8]. The coupling angle is controlled by lateral focusing on the back focus plane.
A typical objective based SPRi setup is shown in Fig. 2.25. SPR excitation and imaging are accomplished by a high NA objective so that a high resolution could be obtained. The resolution of Huang's system is asymmetric. In the direction normal to the wave vector of SPW, it is governed mainly by the highest NA of the objective and the illumination. For the direction parallel to the SPW direction, the resolution is dominated by the propagation distance. Methods have been proposed to optimize such resolution. A.W. Peterson *et al.* replaced the focusing illumination by a digital light projector [94, 95]. A crescent shaped pattern was projected on the BFP of the objective. The effective NA of the illumination was increased, and a resolution approaching to theorical limit was claimed (0.3 μm using 1.65 NA objective under 620 nm illumination) [94]. Tan *et al.* introduced a circular illumination

method to solve the asymmetric resolution [96]. A quantitative comparison of these SPR microscopes by simulation was published recently [97].

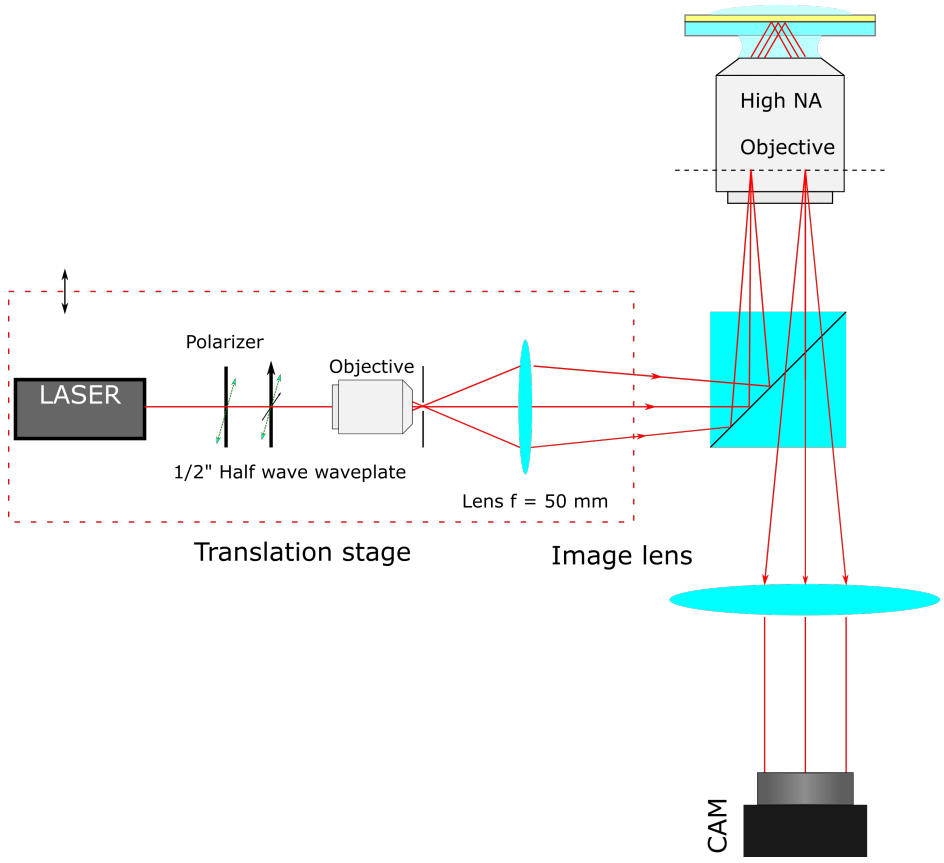

Fig. 2.25 An objective based SPR microscope.

Scanning surface plasmon resonance microscopy

In 1998, H. Kano introduced the method to excite the surface plasmon polaritons (SPP) by focusing on the interface with high NA microscope objective [98]. The localized SPP could be used as a probe to detect the dielectric properties of the sample [99, 100]. The two-dimensional detection is then achieved by scanning the sample using a piezo translation stage. Different from the widefield SPRM for which the illumination is focused on the BFP, the scanning SPRM utilizes collimated illuminations over the whole BFP. Because of this, they cover all the incident angles (from 0 degree to $\theta_{max} = \arcsin(NA/n_o)$, n_o is the refractive index of the objective oil) at the sample-metal interface as shown in Fig. 2.26.

The refractive index of the sample is retrieved from the BFP images of the objective. They

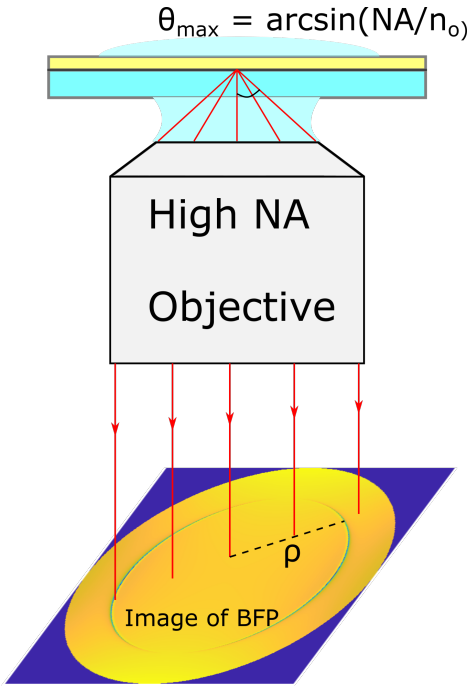

Fig. 2.26 The principle of the scanning SPRM.

respresent the angular spectrum of the the sample response. The radial distance ρ on the BFP corresponds to the incident angle of the illumination. The stimulation of SPR will result in an absorption dip on the BFP image. By measuring the position of such a dip on the BFP, the refractive index of the sample could be retrieved. Two-dimensional cell imaging using scanning SPRM has been reported [101].

Scanning SPRM could be regarded as a probe detection method. So, its resolution is limited by the probe size – the size of the focusing light spot. Such a spot size is related to the NA of the objective and to the polarization of the illumination. A resolution of 210 nm inside water

is reported with an NA 1.40 objective under the radially polarized illumination [100].
This work is focused on the phase response using a high-resolution objective based SPR system. In the next section, the state of the art concerning SPR phase imaging will be introduced in detail.

2.3 State of the art of SPR phase sensing and SPR holographic microscope

In the previous section, I have introduced the background for the SPR sensing and imaging. SPR imaging allows high throughput measurements by monitoring multiple sensing site at the same time. The two-dimensional label free real time monitoring capability also makes this method a powerful tool for the study of cell adhesion to substrate.
Sensitivity of the detection is an essential parameter. For intensity resolved SPR detection method, it is reported to be 10E-5 refractive index unit (RIU). The corresponding limit of detection is estimated to be 1pg/mm^{-2} [102]. SPR phase response detection is reported to be an efficient way to increase the sensitivity of SPR imaging [103]. A. V. Kabashin *et al.* have proved it can improve the sensing sensitivity to 10E-8 RIU with a better stability than the intensity interrogation methods [102]. The high sensitivity of SPR phase detection is due to its steeper slope as shown in Fig. 2.27. And its high stability comes from the fact that a laser source output is more stable in phase than its amplitude [102].

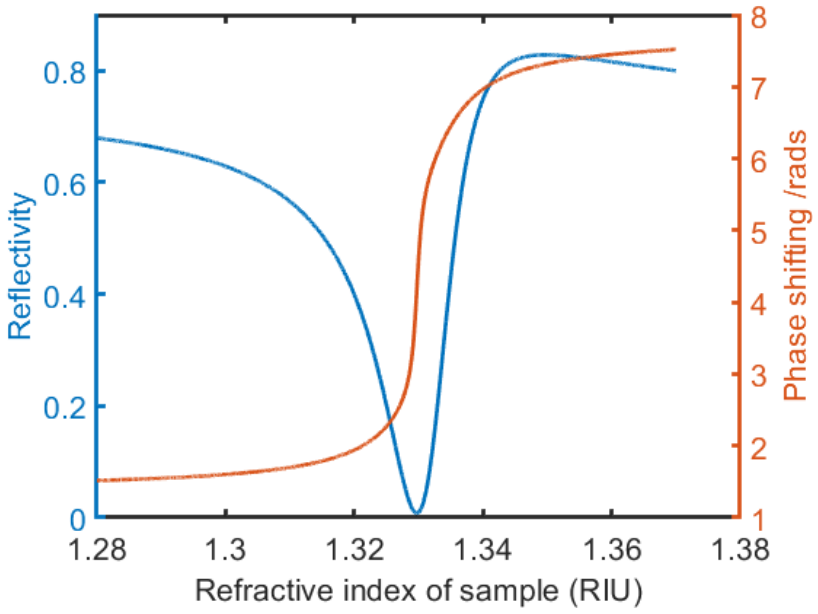

Fig. 2.27 Reflectivity and phase reponses as functions of the sample refractive index (RI). Structure is Glass-Gold-Water with excitation wavelength of 850 nm.

2.3.1 SPR phase sensing and imaging developments

The first theoretical deduction of the SPR phase sensing process was proposed by F. Abelès in 1976 [104]. In this article, he has also introduced the first SPR phase detection method using the ellipsometry (or polarimetry) based on the K-R SPR configuration. The phase response was retrieved from the polarization change of the reflected light. Since then, phase detection methods have been extensively explored. Various phase imaging methods have been combined with the SPRi techniques [102, 105, 106, 103], including polarimetric methods [107–109], optical heterodyning methods [110, 111] temporal modulated interferometric methods (phase shifting interferometry) [112–114] and the spatial modulated interferometric methods which includes the holographic methods [115]. Among these methods, the off-axis holographic methods have the unique advantage of being able to reconstruct unambiguously the intensity and phase response of SPR from a single acquisition. This advantage makes it suitable for real-time in-vivo imaging.

The spatially modulated interferometry method was firstly introduced for SPR phase detection by A. V. Kabashin *et al.* [116, 117]. In their setup, SPR phase response was obtained by a Mach-Zehnder (M-Z) interferometer. A reference wave from the laser source is split and recombined with the object wave reflected from the K-R system. They have then applied the approach to SPR imaging [118]. A wavelength scanning laser source is used. At the excitation wavelength, the phase jump of SPR creates singularities on interference pattern. So instead of a phase detection method, it is actually a wavelength interrogation one. Later in 2000, A. G. Notcovich has published experiment results of the SPR phase imaging based on a similar setup. The 2D phase response is retrieved by a Fourier fringe analysis [119]. The interferometric image captured by Notcovich could already be regarded as a hologram. However, due to the limited image quality and the resolution of the digital imaging sensor available in that time, the holographic principle has not been applied to SPRi until 2010 [115]. C. Hu *et al.* built an SPR digital holographic microscope (SPR-DHM) based on the K-R configuration combining with the M-Z interferometer. The setup is shown in Fig. 2.28. The object wave stimulates the SP resonance through the prism-based K-R setup. The reflected image is then obeserved by a microscope objective (MO). Like the Kabashin's setup, the reference light is split after the laser source. It travels through an additional MO that is identical to the imaging one to compensate the phase distortion introduced by the imaging system. The reference and the object waves are then recombined by a slightly tilted beam splitter (BS) to generate the hologram. Using the SPR-DHM, the onion epidermal cell was observed. Later, in 2012, S. Li and J. Zhong achieved the real-time phase monitoring of NaCl solution evaporation using a similar configuration [120].

The aforementioned DHM is based on the classical M-Z interferometer. The object and reference waves follow independent wavepath before recombined by a BS. The independent wavepath will reduce the system stability and cause interference noise. Additionally, the spatial phase modulation brought in by the imaging system at the object arm needs to be compensated by installing an identical system in the reference arm. The complexity of system is increased.

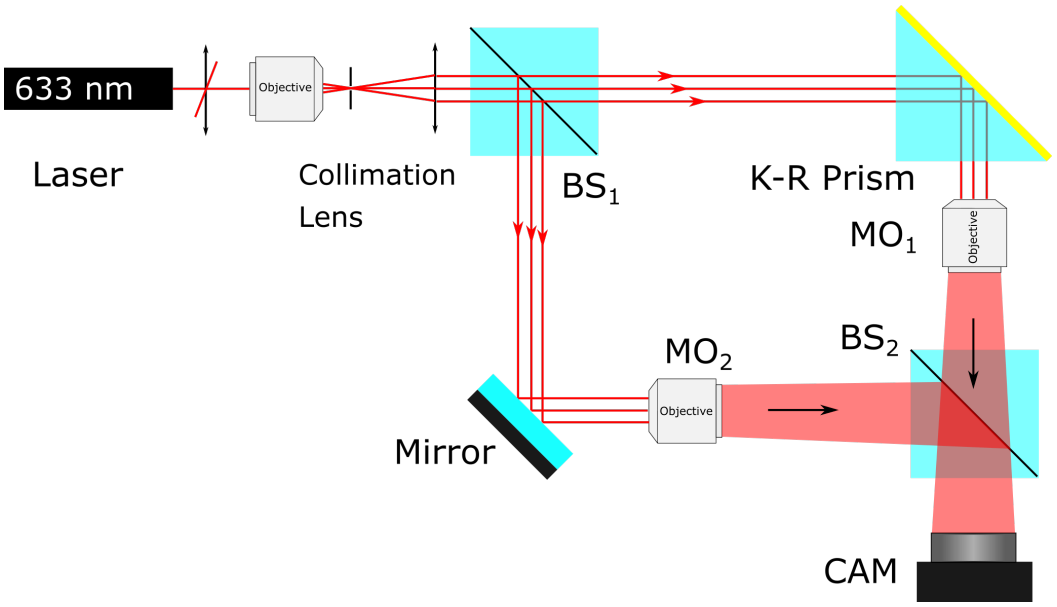

Fig. 2.28 The M-Z interferometer based off-axis SPRDHM. Drawing based on Ref. [115].

2.3.2 Common path SPR-DHM

It has been mentioned in the previous chapter that only p-polarized light will excite the SPW, the s-polarized component is merely changed and reflected by the metal surface. In this case, the s-polarized light could be used as a reference wave. The first common path interferometric SPR setup was introduced in 1999 by N.I. Nikiten *et al.* [121]. The configuration is illustrated in Fig. 2.29. At the output side of the K-R prism, a Wollaston prism is installed to divide the object wave and reference wave. The latter is a birefringent optical component which can separate orthogonal polarizations with a small angle. The laterally sheared light field travels through a polarizer so that the polarizations of both the object and the reference wave are turned to the same direction. The overlap of the two components will create the interference image. In the work of Nikiten, the system is used for a single point sensing. X. Yu *et al.* have implemented the common path SPR interferometric imaging setup by adding an imaging lens under the collimated illumination. The phase information is then retrieved by analyzing the interference fringes. The real-time parallel monitoring of sensing array on the gold surface was then achieved. The p and s components could also be divided by other birefringent meterial. J. Zhang *et al.* replace the Wollaston prism by a specifically positioned single polarizing BS (PBS) [122–124]. Instead of the fixed dividing angle of Wollaston prism, it could be adjusted by turning PBS in Zhang's setup.

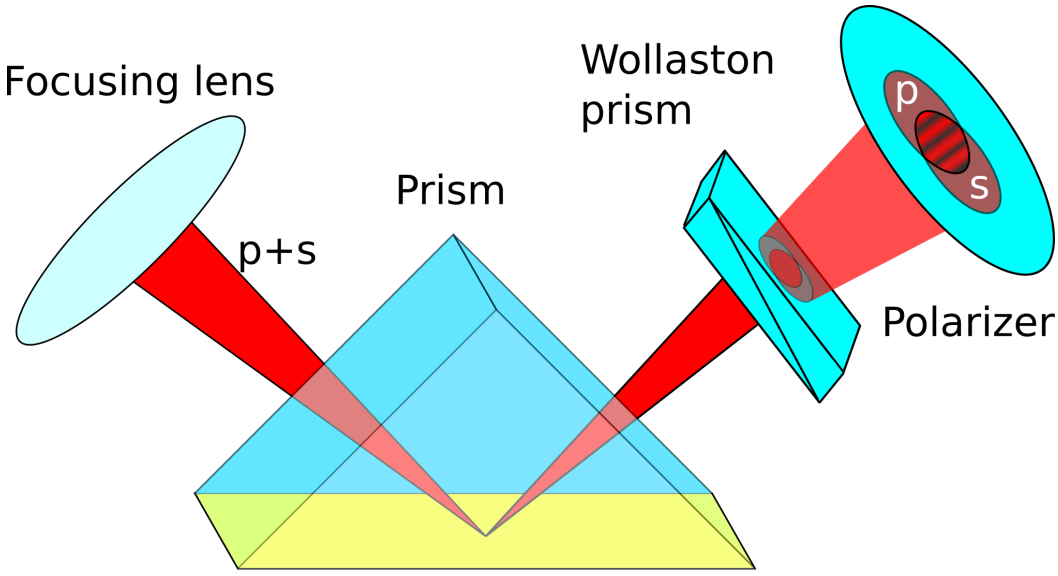

Fig. 2.29 Wollaston prism based off-axis SPR-DHM. Drawing based on Ref. [121].

2.3.3 Objective based SPR-DHM

The resolution of the K-R SPRi setup is limited by the coupling prism [8]. Only a long working distance objective is applicable with such a prism. Its NA is usually limited to lesser than 0.5. Objective based SPRM with the utilization of high NA oil immersed objective can increase the lateral resolution to hundreds nanometers. B.Mandracchia introduced the first objective based SPR-DHM in 2015 [9]. The setup is illustrated in Fig. 2.30. A M-Z interferometer is used to create the hologram. The p-polarized light which carries the SPR information and the s polarized light that is reflected from the objective are split by the polarizing beam splitter (PBS). The polarization direction of the s component is rotated by a half wave plate. They are then recombined by a non-polarizing beam splitter (BS) which is slightly tilted to produce the off-axis hologram.

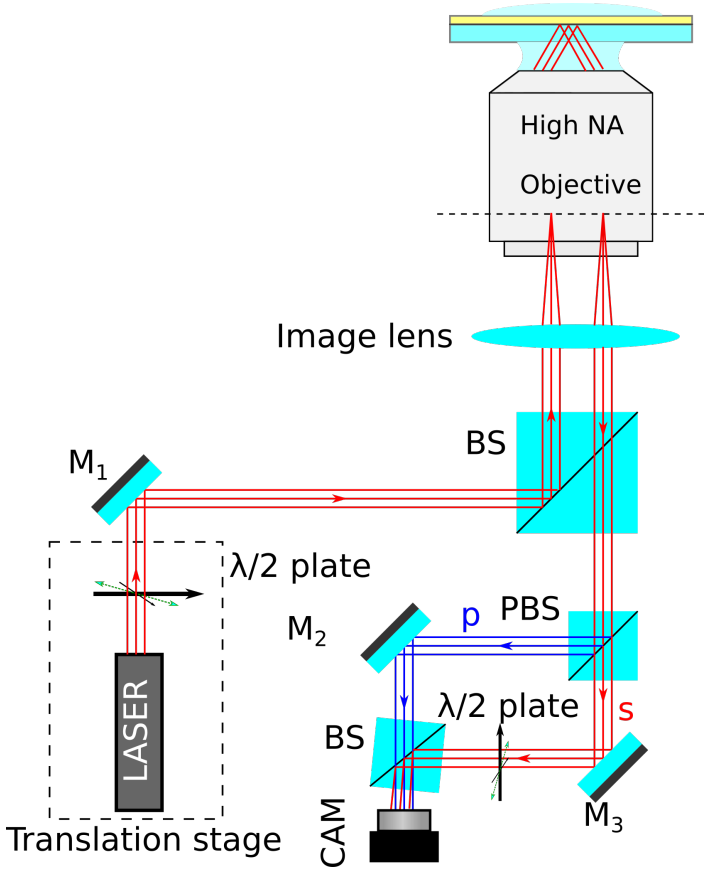

Fig. 2.30 Objective based SPR-DHM, the hologram is generated by the M-Z interferometer. BS: Beam Splitter, PBS: Polarized Beam Splitter, M : mirror. Drawing based on the Ref. [9].

A polymere pattern is observed by the proposed SPRDHM. The synthetic measurement of intensity and phase response has increased the measurement sensitivity to the object profile.

Zhang *et al.* replaced the M-Z interferometer in Mandracchia's system by a Wollaston prism [10]. The common path off-axis configuration reduces the complexity of the system and increases its robustness. They have successfully implemented their system for quantitative reconstruction of the near field thin film. Based on the Fresnel relations, relation between the sample thickness and the SPR response has been established. They claimed that the sensing resolution is sub-nanometric. Recently they have applied this common path off-axis SPR-DHM for real time in vivo observation of cell-substrate adhesion [11]. The activity of living mouse osteoblast cells and human breast cancer cells was observed. They have further improved the performance by using a two-channel illumination [125]. As introduced in Sec. 2.2.1.1, the lateral resolution of SPRM is mainly limited by its propagation distance. Depending on the excitation wavelength, the resolution along the SPW direction ranges from several microns (1.7 μm for 600 nm excitation) to thirties microns (36 μm for 1000 nm excitation). In the improved setup two channel illuminations were injected into the excitation objective to create two SPR waves with mutual orthogonal propagation direction. The resolution reduction caused by the SPW surface propagation is compensated by the SPW propagating in its orthogonal direction. In the following chapter, we propose our NIR SPR-DHM. The 850 nm NIR source reduces the resonant angle so that the NA 1.42 microscope objective can be applied. The holographic imaging is realized by the Wollaston prism based setup.

2.4 Conclusion

In this chapter, principles of the holographic imaging and SPR imaging techniques have been introduced. Also the development of the SPR phase sensing and SPR holographic imaging is briefly reviewed. The digital holographic techniques combined with the objective based SPR microscopy allows high sensitivity and high resolution imaging of the SPR response in real time.

Chapter 3

The surface plasmonic holographic microscope setup

3.1 A general introduction of the setup

3.1.1 Technical background of the design

There are three essential choice to be made in order to design and construct a SPR phase microscope: the SPR coupling configuration, excitation source, and the phase detection technique.

In last chapter, historical developmens of SPR phase microscopes have been introduced. The prism coupling method and the objective coupling method could be selected for the purpose of widefield SPR imaging. Since high-resolution imaging of SPR is demanded in this work, the objective based SPRM configuration becomes an optimal choice. It allows widefield high-resolution imaging. In biological applications, the sample is immersed in aqueous solution which has an RI similar to water. In order to observe biological samples such as cells or proteins, it is necessary to stimulate SPR at gold-water interface. However, visible light stimulation of the SPR requires a resonant angle extremely high. Based on Eq. 2.62, such angle is shown in Fig. 3.1.

The resonant angle for the commonly used 633 nm He-Ne sources is more than 72 degrees. The maximum excitation angle of the objective based SPR setup depends on its NA. It can be calculated by :

$$\theta = \arcsin(NA/n_g) \tag{3.1}$$

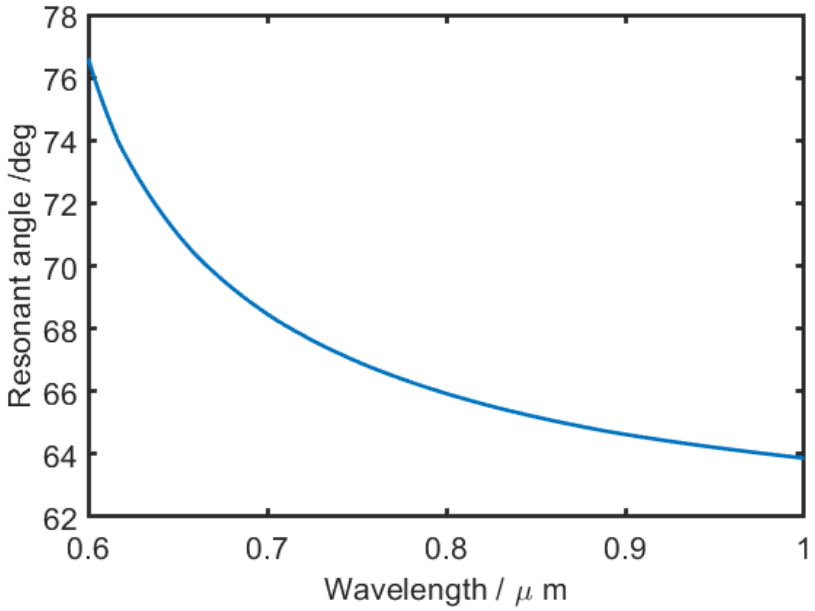

Fig. 3.1 Resonant angle of the SPR as a function of stimulation wavelength using ATR method at gold-water interface.

where n_g is the refractive index of the coupling glass for the ATR method. Considering the most commonly used BK-7 glass, n_g is around 1.51. As a result, in order to excite SPR at the gold-water interface, the NA should be at least 1.44. In practice, the NA 1.49 or NA 1.65 TIRF objectives are needed. These objectives are expensive and not common in biological laboratories.

According to the Fig. 3.1, the resonant angle decreases as the excitation wavelength increases. At the near infrared regime, it could be reduced to less than 66 degrees. The utilization of NIR illumination for SPR microscopic imaging has been reported in the work of A. Halpern *et al.* The resonant angle has been reduced to 65.5 degree by using an 814 nm NIR laser diode source [126]. Although in this paper an NA 1.49 objective is selected, they suggested that an NA 1.40 objective could be applied for the SPR excitation in this case. Recently R. Spies *et al.* used the NA 1.40 oil immersed objective to observe diffraction of SPW by particles at the interface. However, the SPR is not stimulated by the objective, Instead it is excited independently by lighting a microsphere [127]. To the best of our knowledge, the relatively low NA objective has not been reported for SPR excitations. The SPR-DHM which uses the NIR source and non-TIRF objective remains to be explored.

Apart from the fact that the NIR illumination could reduce the resonant angle, an NIR based SPR setup has a better sensitivity for intensity. According to Fig. 3.2, the SPR with 850 nm excitation is far more sensitive than the one with 633 nm. The sensor for the simulation is

composed of glass, a 3 nm Cr adhesion layer and a 45 nm gold layer. The sample is a water solution with the center RI of 1.33 refractive index unit (RIU).

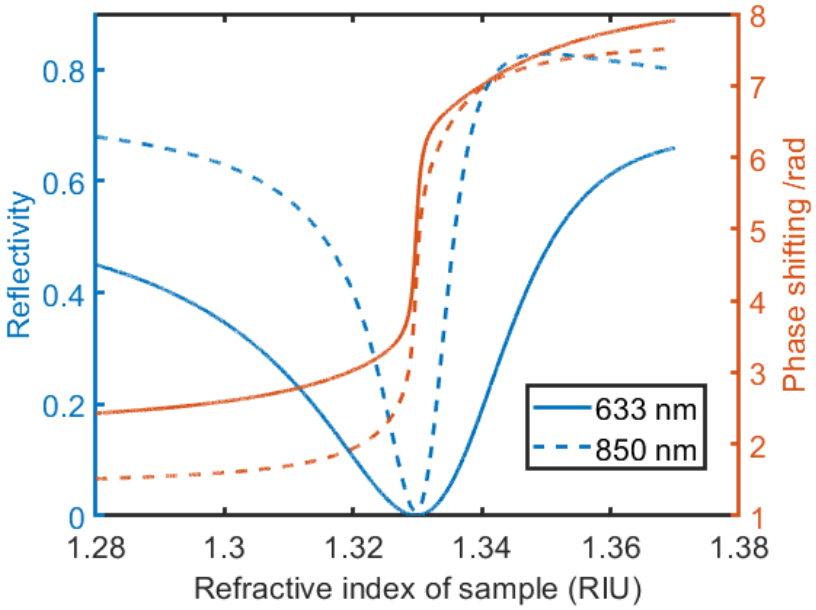

Fig. 3.2 Reflectivity and phase shift of SPR as a functions of the sample refractive index (RI). Blue curves are the reflectivities, and the orange curves are the phase shifts. Solid lines denote an excitation wavelength of 633 nm and dashed lines denote a 850 nm excitation.

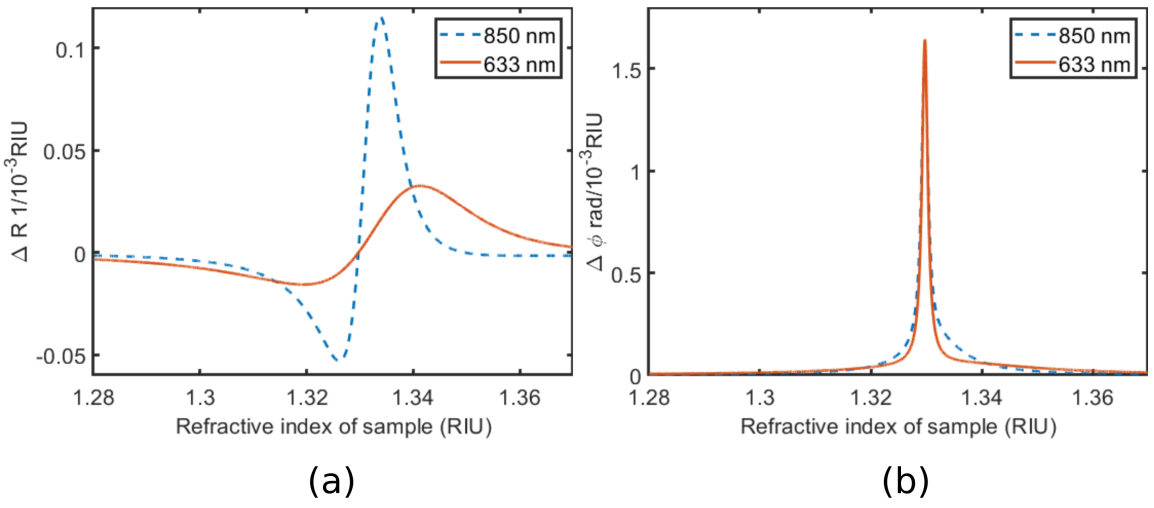

Fig. 3.3 Sensitivity as a function of the sample's refractive index. Blue dashed line is for 850 nm excitation and orange solid line is for 633 nm. (a) Sensitivity of refractivity as a function of sample's RI. (b) Sensitivity of phase shift as a function of sample's RI.

Sensitivity of the SPR detection deduced from the complex SPR response is shown in Fig. 3.3. Maximum sensitivity for the 850 nm source is 0.115 /10E^{-3} RIU which is 3.5 times higher than the one of 633nm. As for phase response, their sensitivity is similar. In conclusion, the use of NIR source could increase the sensitivity as compared to the commonly used 633 nm laser.
Based on these advantages, an NIR laser source has been selected as the excitation source for the SPR-DHM. And an cost effective 850 nm laser diode has been chosen.
Phase detection method is the last selection to be made. Real-time imaging requirement makes the off-axis DHM a better choice among various phase imaging techniques. Due to the limited coherence length of the laser diode, instead of the most commonly used M-Z configuration for DHM, the common path configuration was selected.

3.1.2 Description of the used experimental setup

By using the 850 nm NIR source the resonant angle is reduced to 65 degrees. The NA requirement for coupling microscope objective(MO) is then reduced to 1.37. In this project, an NA 1.42 infinite corrected objective was selected. The schematic presentation of the SPR-DHM is shown in Fig. 3.4. Fig. 3.5 is a photo of the setup. The system could be separated into three parts: the illumination part, the SPR stimulation and imaging part and the hologram generation part. Here the functionality of each part will be introduced briefly.

Illumination subsystem This part contains an 850 nm NIR diode laser, a polarizer, a half wave plate, a spatial filter (objective and pinholes) and a focusing lens. The NIR source is polarized and filtered then focused onto the BFP of the imaging microscope objective (MO). The system is installed on a translation stage to control the focusing position.

SPR stimulation and imaging subsystem This part includes the cube beam splitter, the coupling and imaging high NA MO, an image lens and a spatial filter. Light is focused on the BFP of the high NA MO, it is then collimated by the MO on the front focal plane (FFP). The illumination light impinges on the gold-dielectric interface at the SPR resonant angle. p-polarized light will stimulate the SPR, and the reflected beam carries the information of the interaction between the sample and the SPW. The s-polarized part cannot excite the SPR, It is reflected by the metal interface directly and serves as the reference wave. The reflected p and s light are then collected by a long focal length lens. The MO and the long focal length lens together, may be regarded as a 4-f system which directs the information to the sensor. A

spatial filter is installed before the lens to block unwanted reflections from the cube beam splitter (BS).

Hologram generation subsystem In this work, phase information of the SPR is acquired by means of holography for the purpose of real time imaging. We have selected a common path off-axis holographic configuration which is inspired by the work of Zhang [10]. The common path configuration is the based on a Wollaston prism. It splits the p polarized light and s polarized light with a small angle. The p-wave which carries the informations of SPR is the object wave, and the s wave since it is reflected directly serves as the reference wave. The orthogonally polarized object and reference waves are combined by a linear polarizer. The hologram is captured by a conventional CMOS camera without the IR filter.
Technical issues and their solutions of each sub-system will be discussed in detail in the following subchapters. The used optical components are listed in the Appendix.A.1.

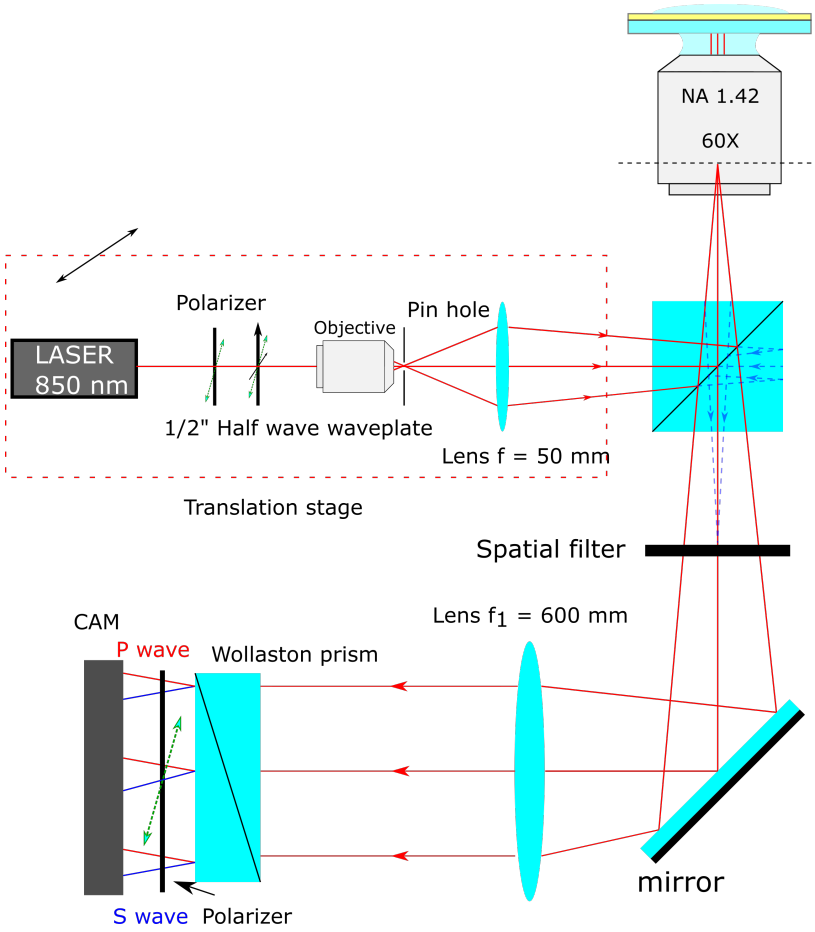

Fig. 3.4 Schematic representation of the SPR-DHM

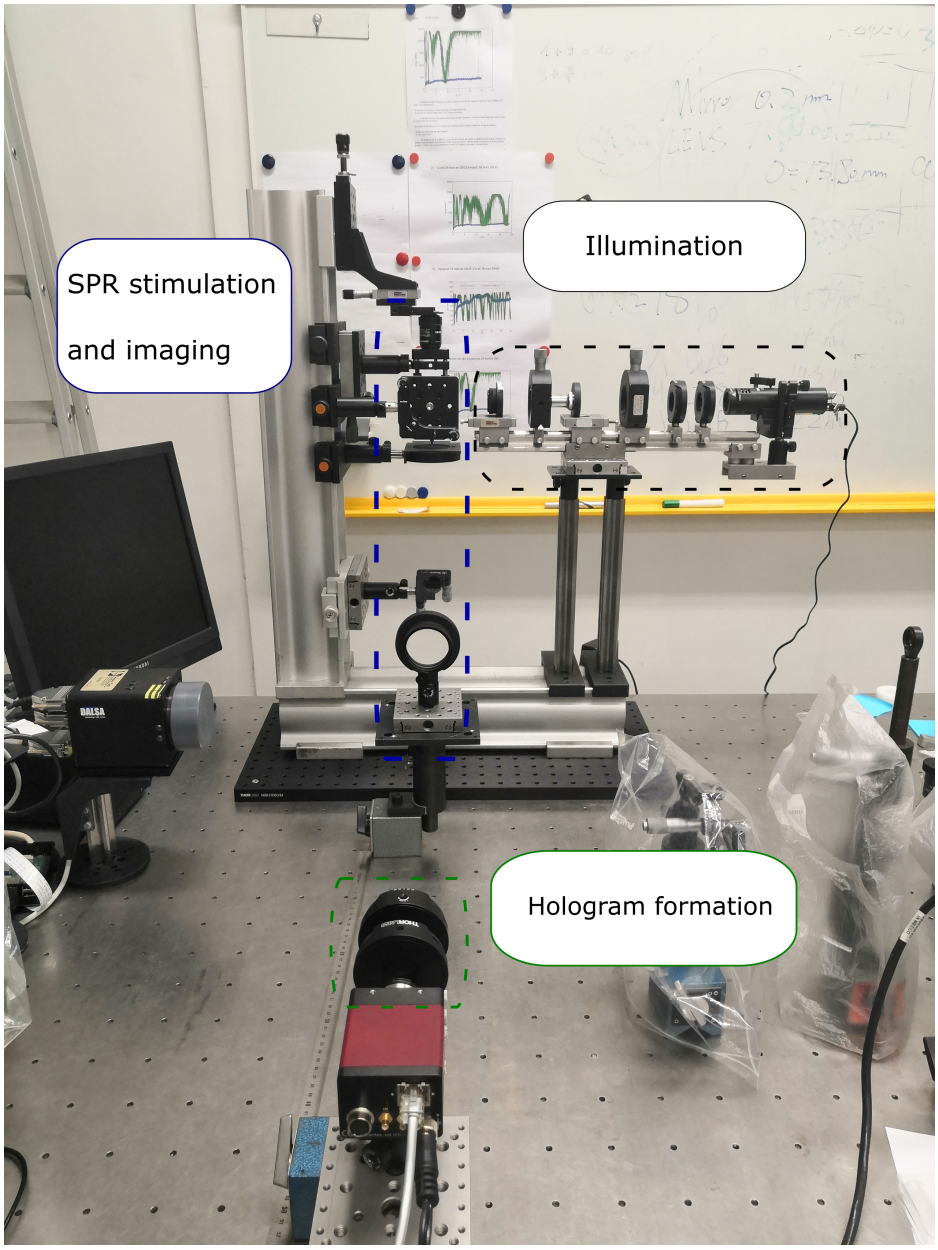

Fig. 3.5 SPR-DHM setup

3.2 Illumination subsystem

The illumination subsystem is composed of an NIR laser diode, a linear polarizer, a half wave plate, a spatial filter, beam shaping components (objective and pinhole) and a focusing lens. It is installed on a translation stage which controls the focusing position on the BFP of the coupling MO.

3.2.1 Coherence measurement of the laser source

In order to have high contrast interference fringes on the sensor, the optical path difference between the object wave and the reference wave should be smaller than the coherence length of the laser source. To properly design the holographic setup, it is required to know such a length.

We have selected the "Thorlabs LDM 850" 850 nm NIR laser diode as the infrared source. Its approximate bandwidth is 2 nm in wavelength. The coherent length is calculated with [128]:

$$\Delta l = c\Delta t \approx \frac{c}{\Delta v} = \frac{\overline{\lambda_0}^2}{\Delta\lambda_0} \tag{3.2}$$

$\overline{\lambda_0}$ represents the average wavelength, and $\Delta\lambda_0$ is the FWHM of the spectrum. So, the theoretical coherent length of our laser diode is about 360 µm. It should be mentioned that the spectrum of a cost-effective laser diode depends on the fabrication process. Each laser diode is different.

In order to measure Δl, a Michelson interferometer was built. It is widely used for interferometric measurements. It is also an optimal setup to measure the coherence length of a light source. The schematic representation of a Michelson interferometer is given in Fig. 3.6. The mirror on the right side is slightly tilted to create the interference fringes. It is installed on a translation stage to control the optical path difference between the arms.

The intensity distribution of the interference pattern I could be written as:

$$I = I_1 + I_2 + 2\Gamma_{12}\sqrt{I_1 I_2}\cos(\Delta\phi) \tag{3.3}$$

I_1 and I_2 are the intensities of the light reflected by the mirrors of the interferometer arms. Γ_{12} denotes to the degree of coherence. The visibility of the fringes is calculated by:

$$V = \frac{I_{max} - I_{min}}{I_{max} + I_{min}} = \frac{2\sqrt{I_1 I_2}}{I_1 + I_2}\Gamma_{12} \tag{3.4}$$

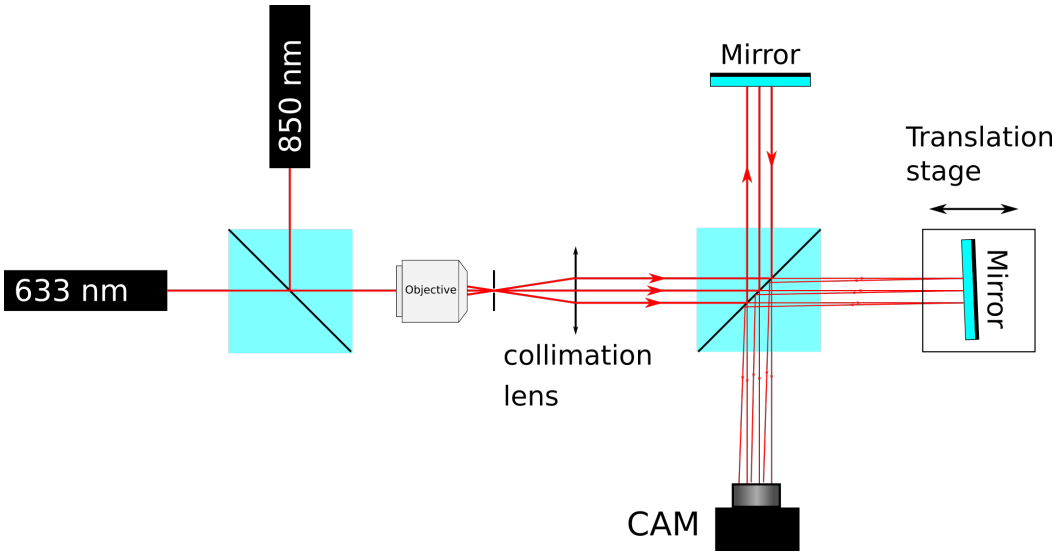

Fig. 3.6 Schematic representation of the Michelson interferometer. A 633 nm HeNe laser is used for the system alignment.

When the light coming from the both have identical intensities, Eq. 3.4 becomes:

$$V = \Gamma_{12} \tag{3.5}$$

In practice, the intensities are slightly different. As a result, the maximum fringe visibility is lower than 1. The coherence length is defined as the optical path difference when the fringe visibility is reduced to $1/e$ of its maximum [129]. The measured fringe visibility and their corresponding optical path difference are shown in Fig. 3.7. The coherence length is 480 µm. Multiple estimations have been made by selecting the fringes on various location on the interference image. A variation of 5 µm is observed. So, the measured coherence length of our 850 nm laser diode is 480 ± 5 µm.

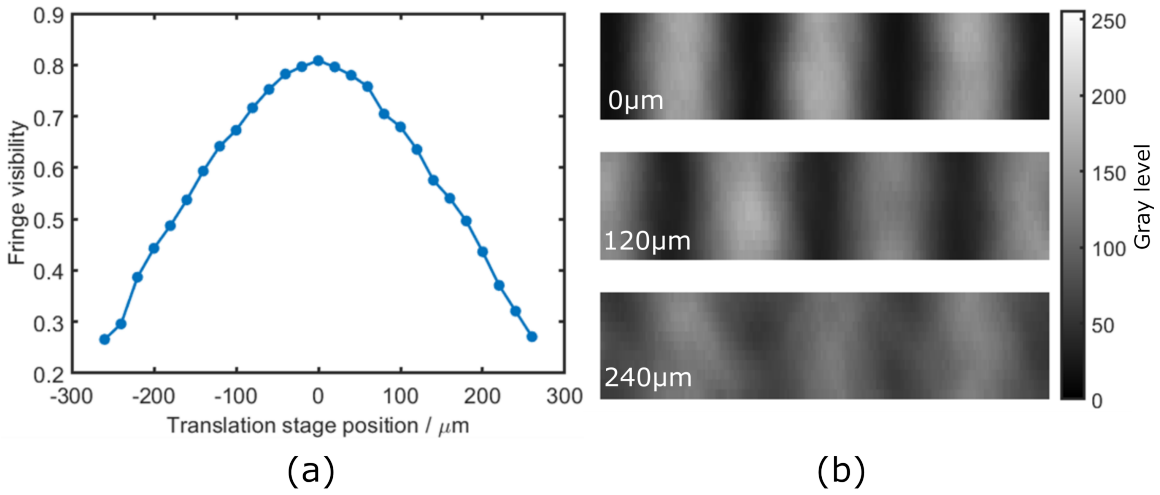

Fig. 3.7 (a) Measured fringe visibility (b) Interference fringes at measured positions of 0, 120 µm and 240 µm.

3.2.2 Laser diode filtering and shaping

Laser diodes have usually elliptical beam shapes due to the cavity and the output window. The LDM850 laser diode spot is 3.5 x 4.4 mm which is measured at 3m away. For imaging system, circular gaussian beams are preferred. Also, beam expanding is also required for our BFP focusing. For these two reasons, the objective and the pinhole combination was selected.

Additionally, in order to have a better quality of beam filtering, the elliptical beam is prefiltered by a 1mm diameter pinhole before .

In this part, two parameters need to be determined, the objective focal length and the pinhole size. The filtering objective determines the image size on the sensor plane, as shown in Fig. 3.8.

The relation between the image size and the MO focal distance is written as:

$$d = \frac{D_{in}}{F_{obj}} \frac{f_0 f_l}{Z_2 - f_0} \tag{3.6}$$

D_{in} is the beam diameter which equals to 1mm. f_0 and f_l denote the focal length of the focusing and imaging lens respectively. Z_2 is the distance between the collimated lens and BFP of the objective. F_{obj} is the MO focal length. Here the image diameter is limited by the aperture of the Wollaston prism which is 10 mm. The focal distances of the focusing lens and image lens are 50 mm and 600 mm respectively. And the distance between the focusing

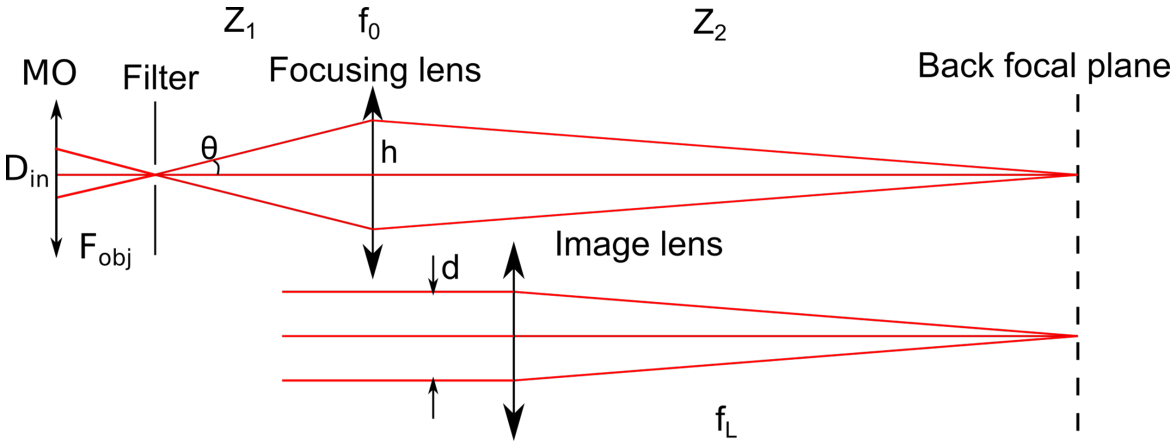

Fig. 3.8 Image generation based on geometrical optic.

lens and the BFP is around 160 mm. The F_{obj} is calcuted to be 27.3 mm when the diameter of the image equals to the aperture size of the Wollaston prism.

Apart from the the Wollaston aperture, the selection of the filtering MO must take into account the pupil size of the imaging MO. The resonant angle of the SPR for gold-water interface is around 65 degrees. For such a large resonant angle, the focus point needs to approach the edge of the MO BFP. It also means that it approaches the edge of the MO pupil. If the filtering objective has a too large NA, the illumination beam could be diffracted by the pupil. Unwanted fringes will appear on the image as shown in Fig. 3.9. This phenomenon could be avoided by limiting the NA of the objective. The pupil size and its position are not given by the manufacturer. So the NA of the focusing objective needs to be determined experimentally. In the end, the 10x NA 0.25 objective has been selected with a focal distance of 16.5 mm. The diameter of the image is around 16.5 mm that is larger than the aperture of the Wollaston prism in order to have a relatively uniform hologram intensity. The pinhole serves to filter out the central lobe of the airy pattern. Its size of the first lobe is determined by:

$$D = 2\lambda F_{obj}/D_{in} \tag{3.7}$$

The pinhole diameter is 28 µm for $\lambda =$ 850 nm. It is suggested to be 30 % larger than the diameter of the first lobe. So the optimal size is calculated to be 38 µm. In practice, by slightly moving away a little bit from the MO focal point, a larger pinhole could also be used. Here a 50 µm pinhole has been selected for filtering.

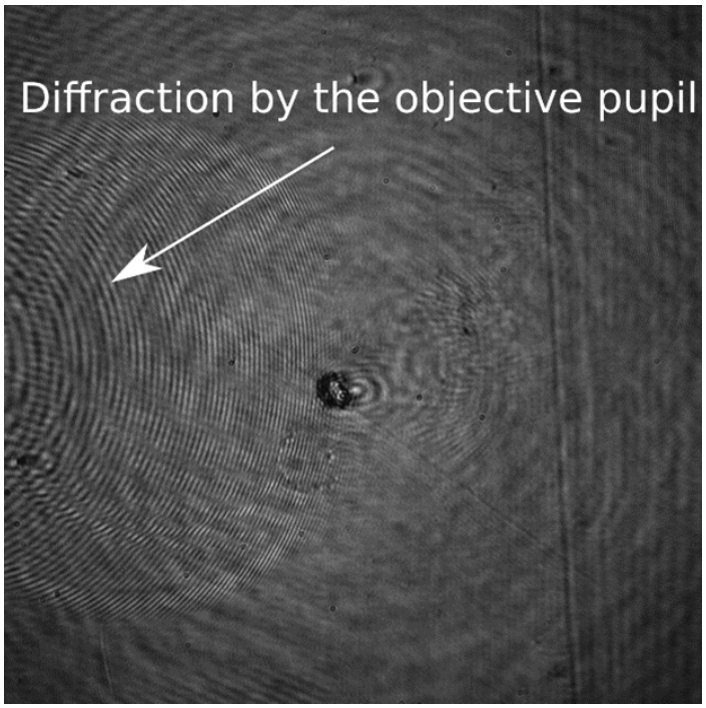

Fig. 3.9 Diffraction by the imaging MO pupil as the illumination beam approaches to its edge.

3.3 The SPR stimulation and imaging subsystem

In this setup, the SPW is excited and observed by a microscope objective as illustrated in Fig. 3.10. The coupling MO collimates the illumination which is focused on its BFP. The p-polarized component will stimulate the SPR on the metal-dielectric interface, and the s component is reflected directly. The image plane is conjugated to the camera plane by a long working distance lens. A spatial filter is inserted before the lens to filter the light reflected from the cube.

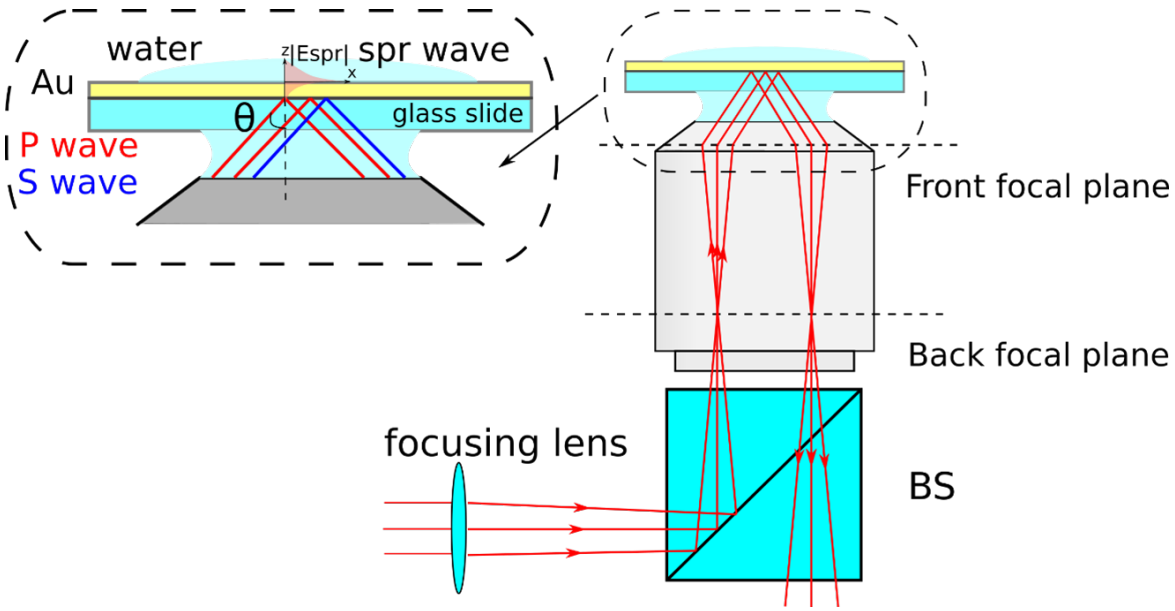

Fig. 3.10 SPW excitation by a microscope objective. Inset shows excitation at the interface with a large angle of incidence.

3.3.1 The high numerical aperture objective

The coupling objective selected for the NIR SPR-DHM is the Olympus NA 1.42 UPLXAPO60XOPH oil immersed MO. As introduced before, the utilization of a 850 nm NIR laser could reduce the request for the coupling objective NA. Instead of the NA 1.45 100x objective which also meets the requirement, an NA 1.42 60x was selected for its larger field of view (FOV). The theoretical FOV of the UPLXAPO60XOPH objective is 440 µm when its BFP is fully illuminated. In our case, only a small part of the BFP is illuminated. The FOV is significantly reduced.

The quality of the MO has been tested by the setup shown in Fig.3.11(a). A 633 nm laser is injected directly into the Olympus objective. By tilting and displacing the latter, the

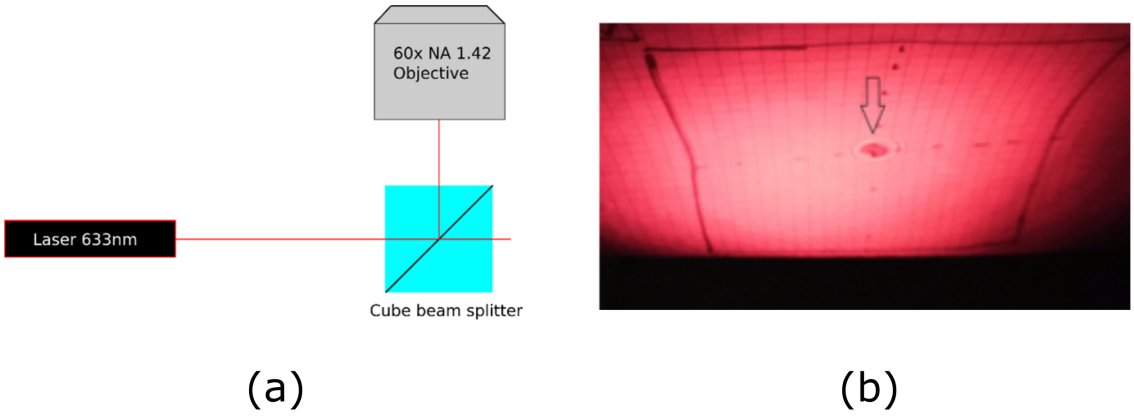

Fig. 3.11 (a) Setup to detect the defects in the objective (b) Transmitted itensity. The diffraction pattern resulting from defect inside the objective locates in the center.

laser will scan throughout the surfaces within the objective. The noticed defect inside the objective has caused a diffraction pattern on the transmitted light. This kind of test although not necessary for a conventional microscope, is critical in our case. For the white light microscopy, the minor defect inside the objective will only cause the lost in resolution. In our case, however a coherent illumination travels though the MO before arriving at the sample plane. Any small defect on the optical path will cause a strong diffraction pattern on the captured image as shown in Fig. 3.12.

Fig. 3.11(b) shows a test result: a diffraction pattern appears in the center of the field. The front and rear surfaces are carefully cleaned so as to avoid the influence of dust. This kind of defect might not have a severe impact on the image quality for conventional imaging. It might not be included in the quality control carried out by the manufacturer. We have tested three MO samples from the manufacturer. Only one was defect free.

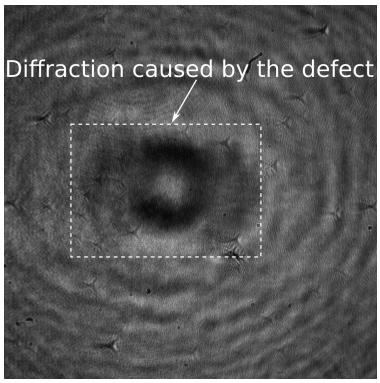

Fig. 3.12 Image captured with a NA 0.65 MO which has a defect inside.

3.3.2 Filtering the unwanted light reflected by the beam splitter

The cube beam splitter is used to reflect the light focusing into the high NA MO. Consequently, reflections by the cube surfaces are inevitable as shown in Fig. 3.13(a). Reflections by the upper and right surfaces are the strongest. The cube is coated with an anti-reflection coating within the range of 700 – 1100 nm. The reflection rate at 850 nm is less than 0.5%. It is not negligible for SPR imaging. As shown in Fig. 3.2 in Sec. 3.1.1, the signal of SPR could be less than 1% at the vicinity of the strongest resonant region. Consequently the reflection by the cube will interfere with the SPR signal and results in an unwanted interference noise.

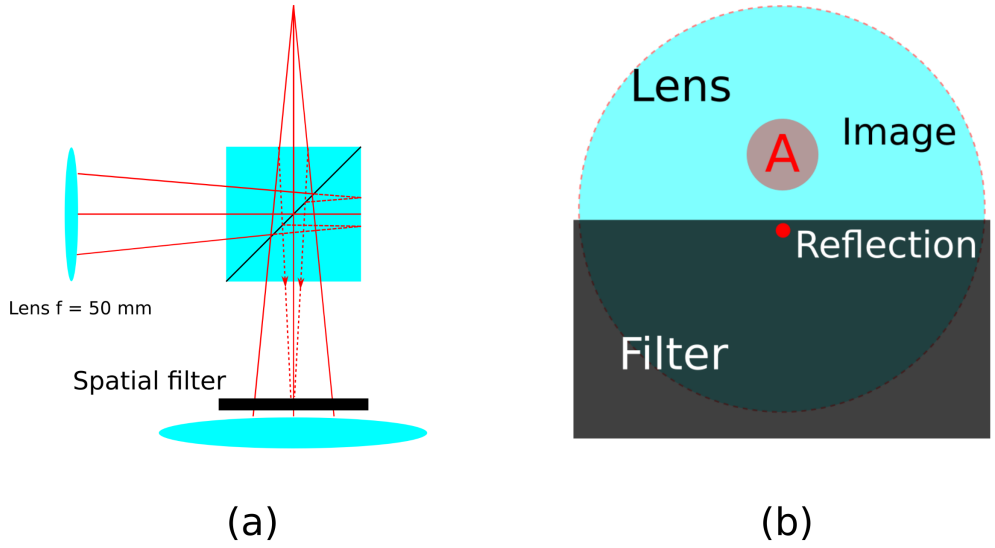

Fig. 3.13 Filtering reflection from the surface of the cube beam splitter. (a) Schematic of filtering (b) Upper side of the spatial filter. The reflected spot is removed by the filter.

With objective coupling method, the illumination does not follow the optical axis of the coupling MO. As a consequence, such an illumination and the reflected image locate symmetrically to the optical axis. As the illumination is focused to the coupling MO, its reflection by cube surfaces will creat an unwanted spot underneath the cube. The relative position of the image and the reflected spot is shown in Fig. 3.13(b).
We have designed and fabricated an edge filter by 3D printing as shown in Fig. 3.14. Its edge of the filter is a razor blade. The principle of the filtering is inspired by the Schlieren imaging [130].
Fig. 3.15 shows the image with and without the filter. The imaged is captured with a 633 nm laser. The cube beam splitter surface has a 1% reflectance . The filter effectively removes the reflected spot.

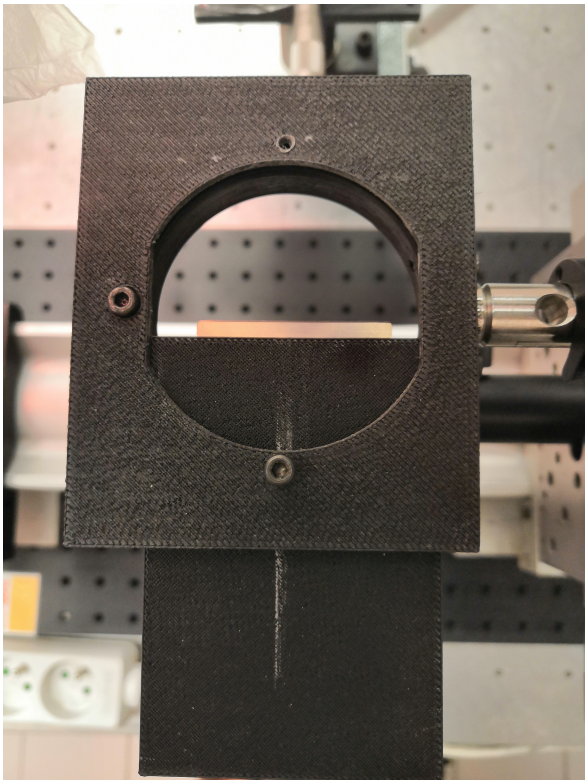

Fig. 3.14 3D printed edge filter

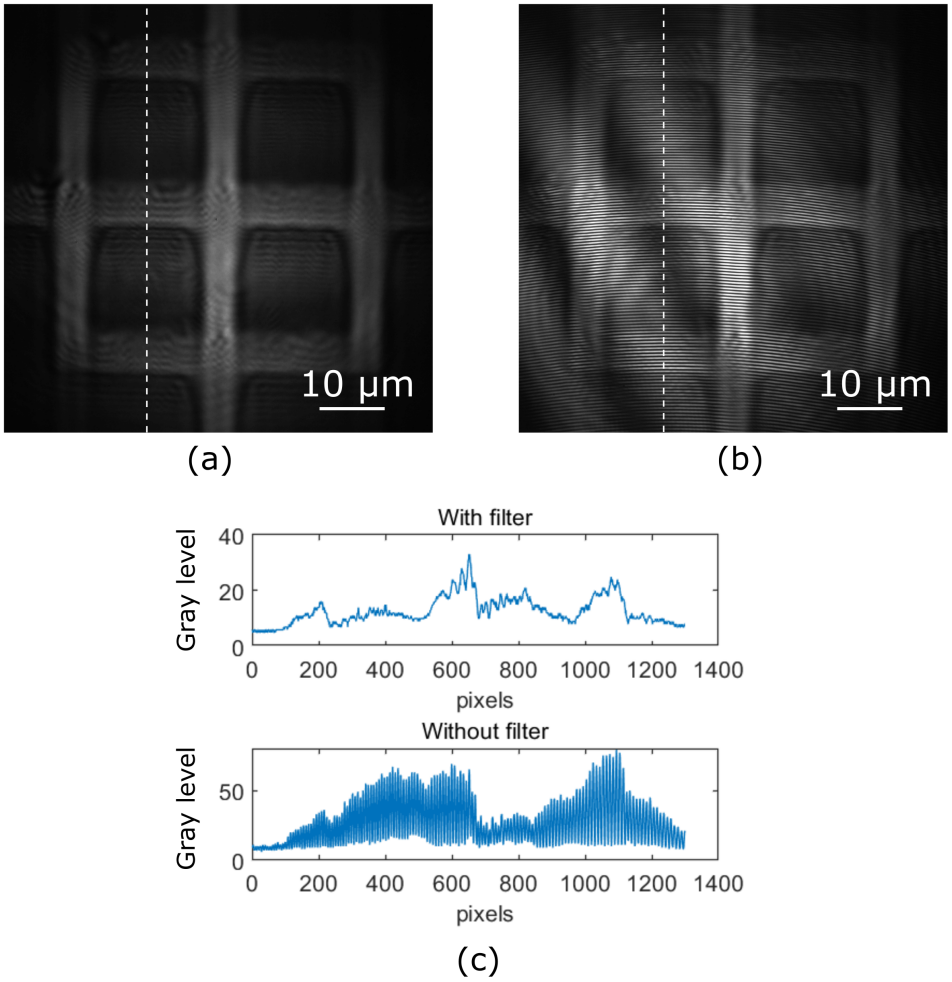

Fig. 3.15 Image captured with and without filtering by an NA 0.65 objective with a 633 nm HeNe laser source. (a) Image captured with the filter (b) Image captured without filter (c) Comparison along the dashed lines

In our SPR-DHM setup the short coherent length laser diode is applied, the reflection will not interfere with the object wave as the wave path difference between the reflection and image is longer than the coherent length. However, after passing through the Wollaston prism, the reflections will be splitted into two, and interfere after the polarizer. An example is shown in Fig.3.16. The hologram fringes are captured with the 850 nm laser diode with or without the edge filter. Because of the short coherence length, the reflected light does not interfere with the object. The influence is much less significant compared with Fig. 3.15 when a long coherence length laser has been used. Although the influence of the reflection

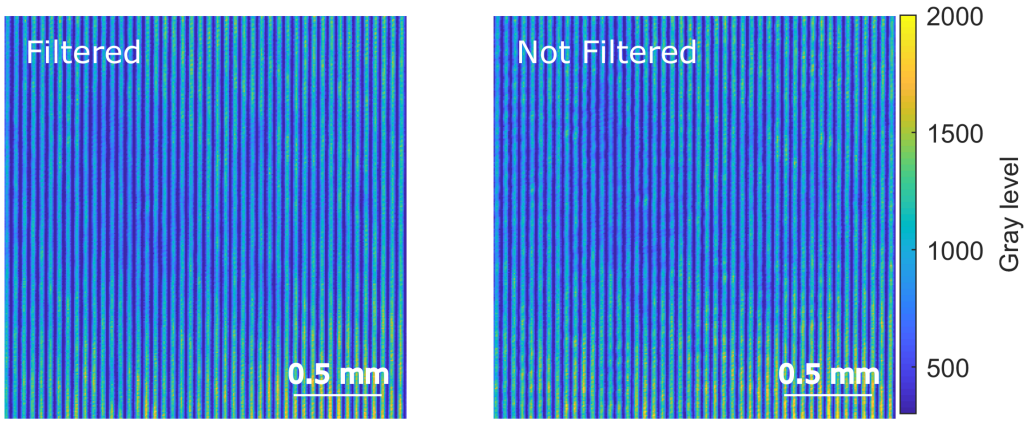

Fig. 3.16 The hologram fringes with and without the filter

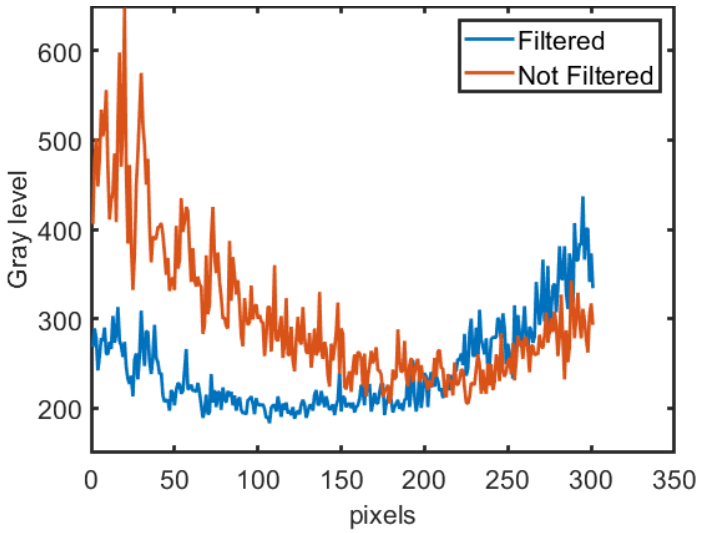

Fig. 3.17 Comparison between the center middle columns of Fig. 3.16

is less obvious, it has a clear effect on the fringes as shown in Fig.3.17. So filtering is still necessary even for a short coherence length illumination.

3.3.3 Focusing on back focal plane and divergence measurement of collimated illumination

The collimated illumination onto the SPR interface is realized by focusing a beam on the BFP of the objective. Such a position is not provided by the manufacturer, It is necessary to locate it experimentally. Also, measurements on the divergence of the collimated light may be useful for future investigations.

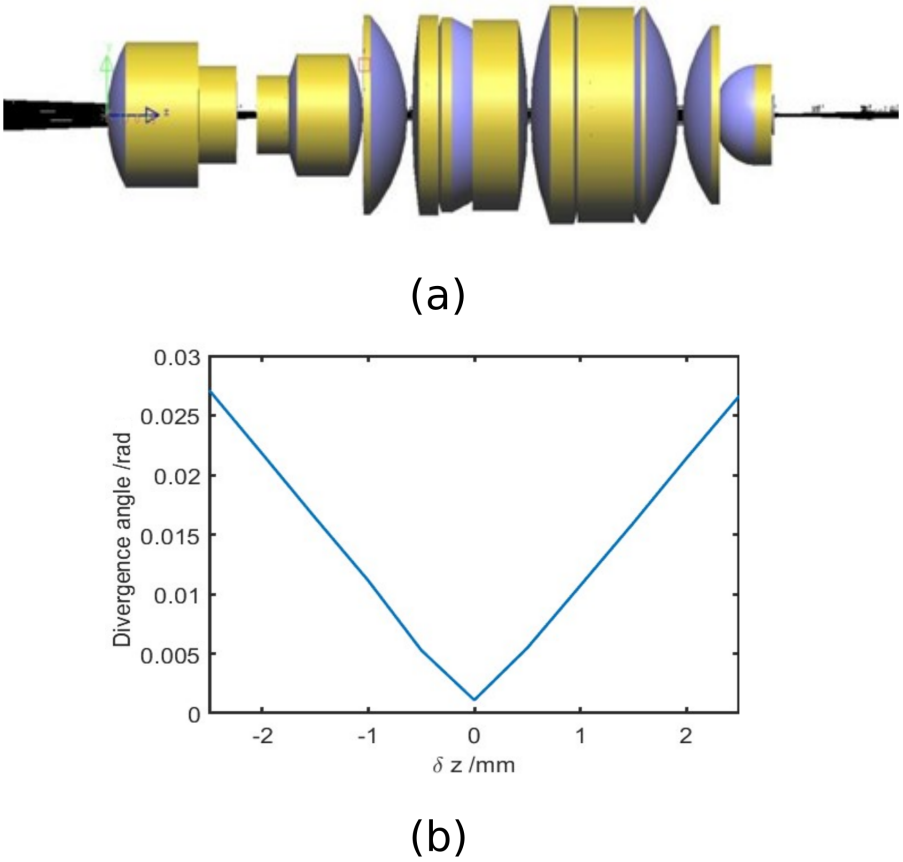

Fig. 3.18 Simulation of BFP focusing with Lighttools. (a) Model of an Olympus 60x objective with a 1.40 NA. (b) Divergence of collimated light as a function of focusing position. Minimum divergence is the position of the BFP.

The model of a 60x Olympus objective, with an NA of 1.40 has been imported into the LightTools^{TM} software. We have located the position of the BFP by means of the built-in optimization function for collimation. The minimum divergence when focusing on the BFP is 1 mrad. As shown in Fig.3.18, defocusing increases the divergence angle and enlarges the outgoing spot size.

We have carried out an experiment to measure such a divergence. The setup is shown in Fig. 3.19 (a). The SPR objective is mounted on a translation stage to control the axial focusing position. The spot diameter is measured by a camera at various axial positions so that divergence is inferred. Since the measurement of divergence is in air, the result should be divided by the refractive index of the microscope oil (n = 1.51). The results are shown in Fig. 3.19 (b). The minimum divergence is 4 mrad. This position is the BFP of the objective. In practice the diameter of the outgoing light spot would be minimum when the illumination is focused at the BFP position.

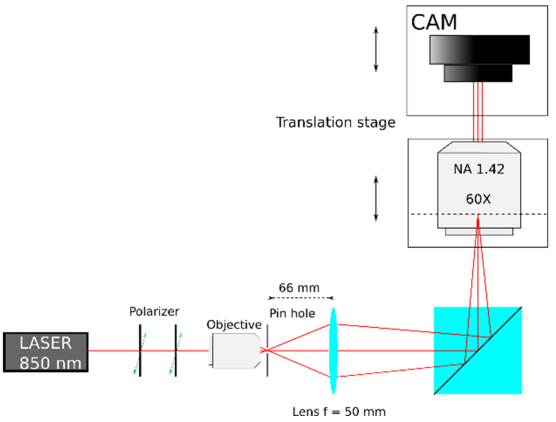

(a)

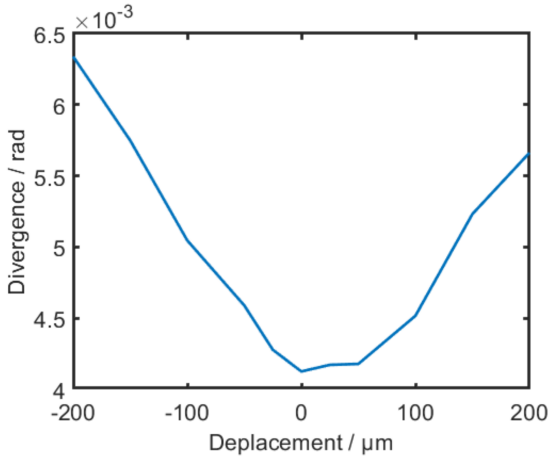

(b)

Fig. 3.19 (a) Measurement setup. (b) Measured divergence as a function of axial position.

3.3.4 Hologram formation

The off-axis hologram method has been selected for SPR phase observation. Its main advantage is being able to achieve the phase imaging in real time. The most commonly used setup is the Mach-Zehnder setup. It has a good flexibility and could be adapted to most of the microscopic setups. But it has a relatively complex structure. Moreover independent object and reference arms could increase the instability of the phase detection. And the short coherence length (480 µm) of the NIR source makes the system alignment difficult.
In our case, the common path off-axis holographic setup is preferable. The common path structure increases the system stability and reduces the requirement on coherency. The s-polarized light is used as the reference. For this reason, among various types of the common path setups, the Wollaston prism based setup is the most suitable.
The Wollaston prism is a birefringent component which consists of two birefringent prisms with orthogonal optical axes. As shown in Fig. 3.20, the prism splits the incident p and s components with an angle which depends on the material and on its angle θ_{prism}.

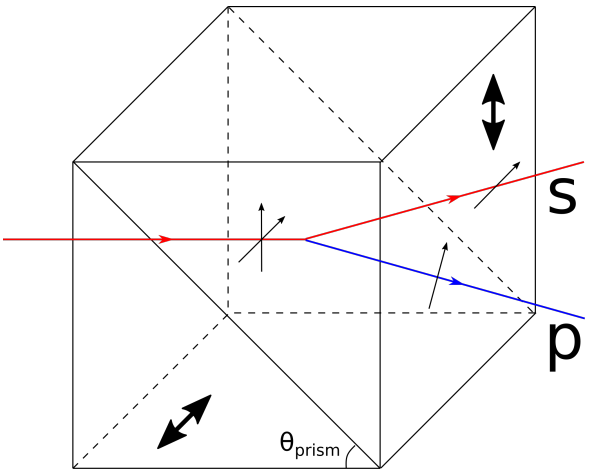

Fig. 3.20 The principle of the Wollaston prism

The splitted orthogonally polarized object and reference waves, are recombined by a polarizer. A schematic representation of the Wollaston prism-based holographic imaging unit is illustrated in Fig. 3.21(a). In Fig. 3.21(b), a resolution target has been imaged. The image is horizontally sheared, creating interferences.

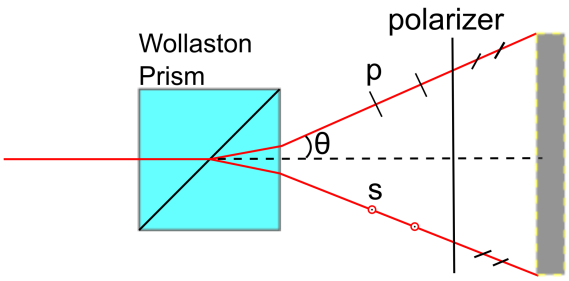

(a)

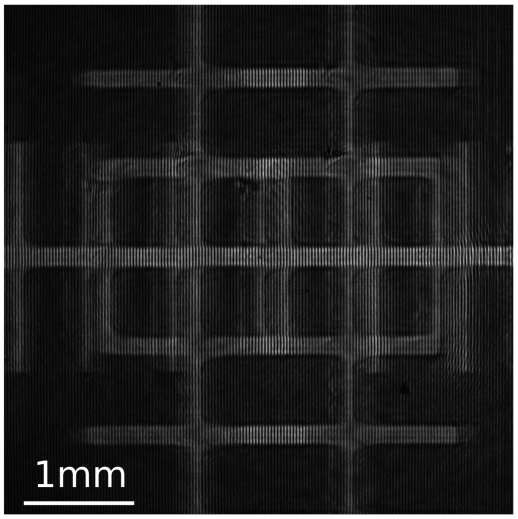

(b)

Fig. 3.21 (a) Schematic representation of the Wollaston prism based hologram formation, θ is the half splitting angle. (b) Shearing inferential image of a target. Image is captured with 40x microscope.

3.3.5 The requirement for the splitting angle

It has been introduced in Sec.2.6 that the splitting angle of off-axis holography should satisfy the following relation:

$$\arcsin(3B\lambda) \leq \theta \leq \arcsin(\frac{\lambda}{2p} - \lambda B) \tag{3.8}$$

The lower limit of the splitting angle θ depends on the image bandwidth, and its maximum is limited by the camera pixel size. The bandwidth B of the microscope is written as [59]:

$$B = \frac{NA}{\lambda M} \tag{3.9}$$

M is the magnification of the microscope. The NA 1.42 infinite corrected objective combined with the recommended f 180 mm tube lens has the magnification of 60 . The corresponding splitting angle would be larger than 4.06 degrees. This is not a typical splitting angle for commercially available Wollaston prisms. Usually they have splitting angles between 1 and 2 degrees (quartz) or around 20 degrees (Calcite, α-BBO prism). It is obvious that 20 degrees are too large here. So, the only solution is to reduce the required splitting angle of the off-axis hologram.
The latter is proportional to the image bandwidth, which is inversely proportional to the system magnification. It could be reduced by increasing such a magnification. It is calculated by:

$$M = f_{tubelens}/f_{objective} \tag{3.10}$$

M is linearly proportional to the focal length of the tube lens. Fig. 3.22(a) is the spectrum of the hologram captured by the NA 0.65 objective. The magnification is 40x using a lens of f 180 mm. The corresponding bandwidth of the first order is 26E-3 μm^{-1}. In Fig. 3.22(b) a f 300 mm lens is used. The magnification has increased to 67x. As a consequence the spectrum is reduced to 15E-3 μm^{-1} which is 60% of the original.
In this work, the f 180 mm tube lens is replaced by an achromatic f 600 mm lens reducing the spectrum to 1/3. The corresponding splitting angle is 1.2 degree. Because the aperture of the coupling MO is not fully illuminated in our setup, the practical resolution will be lower than the theoretical one. In [94, 131], the resolution of a similar setup was measured, the resolution of an NA 1.65 MO is reduced to 500-600 nm under a 633 nm illumination. It has to be compared to the theoretical number of 230 nm. Because of this reason the Wollaston prism with a splitting angle of 1 degree is enough to split the orders.

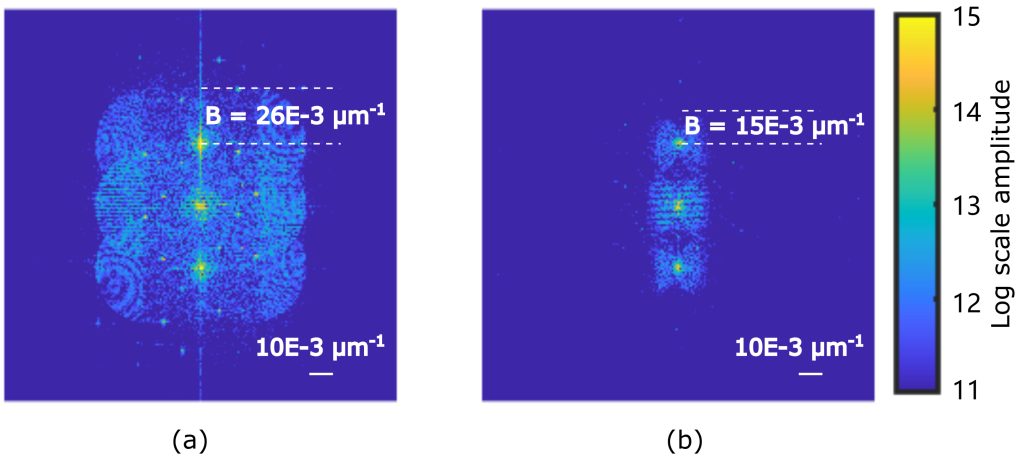

Fig. 3.22 The amplitude spectrum of the off-axis interference image generated by Wollaston prism. The image is captured by a NA 0.65 40x objective. (a) with an f 180 mm lens, the magnification of system is 40x (b) with an f 300mm lens, the magnification is increased to 67x.

3.4 Conclusion

In this chapter, the SPR-DHM system has been introduced. An 850 nm laser diode has been chosen so as to reduce the resonance angle of the SPR. By this means an NA 1.42 oil immersed objective is capable of stimulating the SPR at the gold-water interface. In this work, real time imaging of SPR phase response is sought after. Also, the short coherence length of the laser diode requires a common path holographic configuration. To that end, the Wollaston prism based common path off-axis DHM setup has been selected. The Wollaston prism has a division angle of one degree which is not large enough to separate orders of the off-axis DHM. An f 600 mm image lens has replaced the recommended f 180 mm image lens in order to reduce the bandwidth. The orders could then be separated by the one degree prism. A homemade edge filter has been installed before the image lens to filter out the unwanted reflection from the cube beam splitter. The interference noise on the hologram has been effectively reduced.

Chapter 4

Methods and algorithms for SPR hologram reconstruction

4.1 Introduction to the reconstruction process

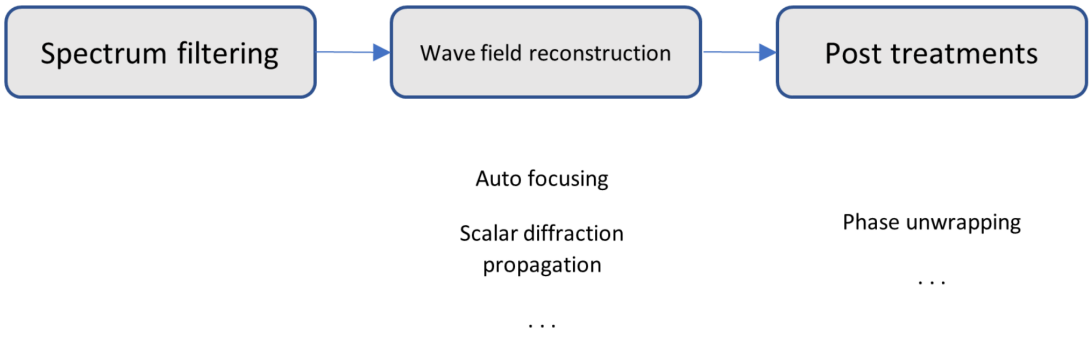

Fig. 4.1 Process of reconstruction

Generally, the reconstruction of an off-axis hologram is composed of three steps as shown in Fig. 4.1. In the step one, the object wavefront is filtered out of the hologram spectrum. Next, in the second step, it is reconstructed by the scalar diffraction propagation method. The propagation distance is determined by an auto-focusing algorithm. In the end, post-treatments would be applied to the reconstructed complex distribution. The most common one is phase unwrapping. The aberration correction is also a commonly seen treatment in digital holographic microscopy, and is usually complex. However, in our setup, the object and sample waves travel through the same optical path, so the aberrations introduced by the optical elements are automatically corrected.

In the following, the algorithms which have been applied to reconstructions will be presented in detail. Their performance for the second and third steps were tested with a lensless inline digital holographic microscope (LI-DHM) system. The main reasons for not using directly the SPR-DHM for the test is due to the limiting samples for observation. Indeed samples with regular shapes with known geometrical parameters are needed. As introduced before, the SPR-DHM is a microscopy technique for observing activities on metallic surfaces. In this case, regular structures need to be formed in the region near the surface. They need to be manufactured by lithography. Such samples are fragile, costly so not very suitable for testing.

Lensless inline holography, however, is more versatile for sample selection. The imaging standard used for transmissive microscopy could easily be applied to the LI-DHM. It is clear that there exists a significant difference in imaging principle between the SPR-DHM and LI-DHM. But, in our case, the LI-DHM is only used as a reference to evaluate the performances of the algorithms for wave field reconstruction and post treatments. Under this aspect, structural difference do not exhibit a big impact. Also, the LI-DHM has a worse imaging quality compared to the off-axis holography because of the overlapping orders in its spectrum. The algorithms which are capable to reconstruct a low LI-DHM holograms are consequently applicable for a higher quality off-axis DHM such as the SPR-DHM in this project.

The LI-DHM consists of a 633 nm HeNe-laser source, an objective and pinhole combination for filtering, a sample holder and a camera for the image acquisition. The sample used is a 150 µm diameter transparent glass sphere. It is immersed in the Canada balsam which compensates the phase difference so as to avoid overexposure due to strong diffraction [38]. The photos of the sample under a bright field microscope and a dark field microscope is shown in Fig. 4.3. The precise diameter of the sample is measured to be 146 µm.The hologram image of the sample under the LI-DHM is shown in Fig. 4.4.

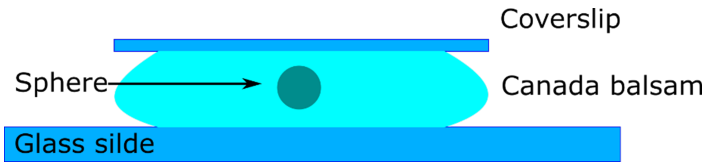

Fig. 4.2 Schematic representation of the sample structure.

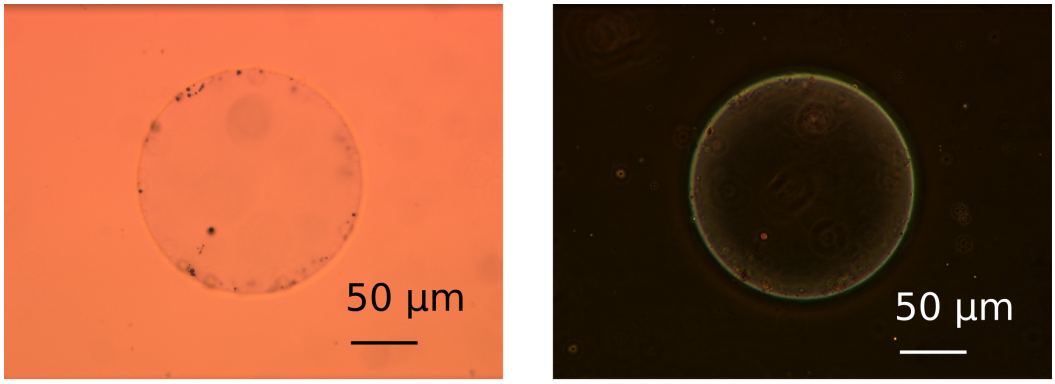

Fig. 4.3 Photos of the sample under a bright field microscope and a dark field microscope.

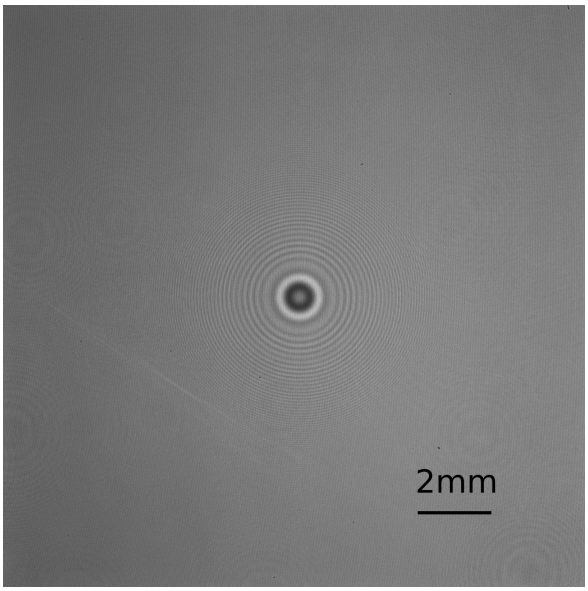

Fig. 4.4 Hologram of the transparent sphere sample using LI-DHM.

4.2 Numerical reconstruction of off-axis hologram

Optical reconstruction of the off-axis hologram has been introduced in Sec.2.1.3. The hologram formula Eq.2.31 is rewritten here as:

$$\begin{aligned} H(x,y) &= |R(x,y)+O(x,y)|^2 \\ &= |R(x,y)|^2+|O(x,y)|^2+R^*(x,y)O(x,y)+R(x,y)O^*(x,y) \end{aligned} \tag{4.1}$$

The optical reconstruction of the off-axis hologram described by Eq. 4.1 is achieved by illuminating the hologram with the original reference wave. As for a numerical reconstruction, it could be realized by the spectrum filtering as illustrated in the Fig. 2.8(illustrated again in Fig. 4.5).

When the splitting angle is large enough, the diffraction orders would be well separated.

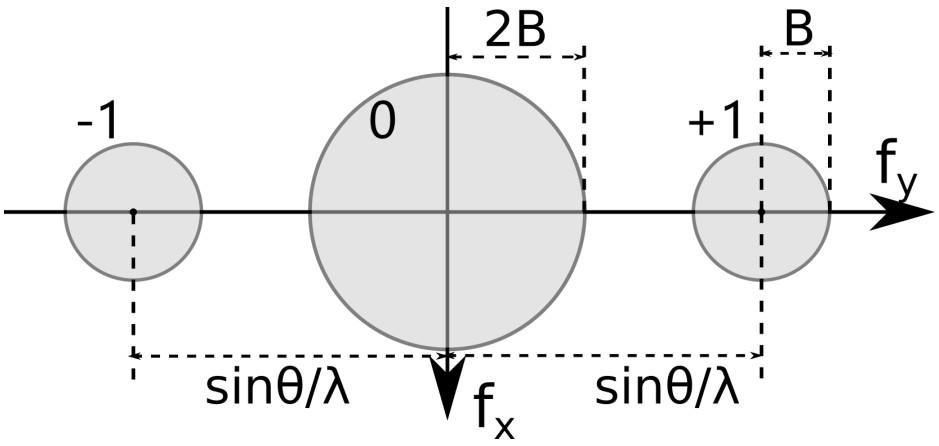

Fig. 4.5 The schematic representation of off-axis hologram spectrum (reprint of Fig. 2.8).

The hologram captured by the SPR-DHM and its spectrum distribution is shown in Fig. 4.6 The complex wave front of the object wave is reconstructed by filtering out either the +1 or the -1 order. Let R be a plane wave described by:

$$R(x,y) = R_0 \exp[jk\sin(\theta)y] \tag{4.2}$$

The first order of hologram then is written as:

$$O(x,y)R^*(x,y) = O_0(x,y)R_0 \exp\{-j[\phi_0(x,y)+k\sin(\theta)y]\} \tag{4.3}$$

The filtered first order (or -1 order) is then moved to the center of the spectrum. Such displacement is equivalent to multiplying by a tilted plane wave $\exp[jk\sin(\theta)y]$.

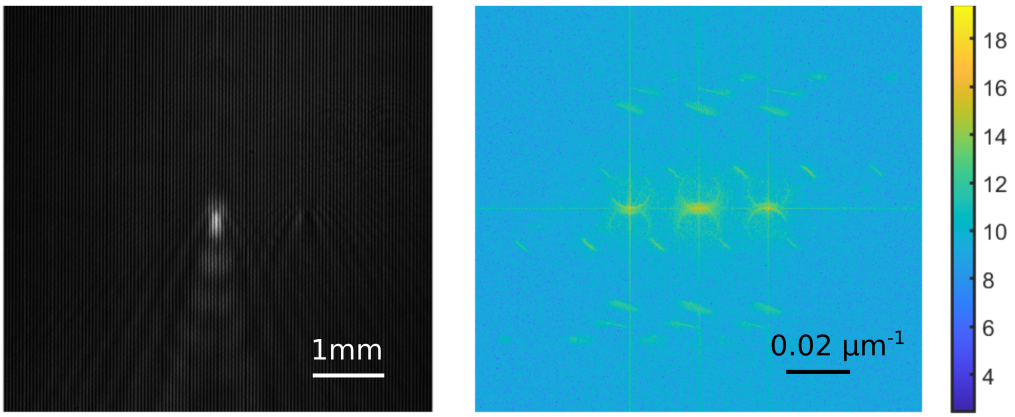

Fig. 4.6 Hologram captured by the SPR-DHM and its spectrum (a) Hologram (b) Amplitude spectrum (log scale)

The object wave $O(x,y)$ will be reconstructed using the aforementioned method if the reference wave is a perfect plane wave. However, the reference wave is not perfect in reality. It contains noise and aberrations. In order to eliminate the noise, a reference hologram is needed. It is captured without the sample, so the reconstruction will only carry aberrations and noise of the reference wave. Such a reference $O_r(x,y)$ is obtained by the filtering method. By noting $O_s(x,y)$ the reconstruction with the sample, the elimination of noise is carried out by dividing the complex amplitude $O_s(x,y)$ by $O_r(x,y)$.

$$O(x,y) = O_s(x,y)/O_r(x,y) = \frac{|O_s(x,y)|}{|O_r(x,y)|}\exp\{j[\phi_s(x,y) - \phi_r(x,y)]\} \tag{4.4}$$

It should be noticed that the wave field $O(x,y)$, is the one on the sensor plane. $O(x,y)$ needs to be backpropagated to the image plane by scalar diffraction method. The scalar diffraction is a linear space-invariant process, it could be described by a 2-dimensional convolution:

$$U(x,y,d) = \iint_{-\infty}^{+\infty} U(x_0,y_0,0)h(x,y,d)dx_0dy_0 \tag{4.5}$$

$h(x,y,d)$ is the point spread function for propagation, which depends on the selected diffraction method. The convolution could be also written in the form of a Fourier transform.

$$U(x,y,d) = \mathscr{F}^{-1}\left\{\mathscr{F}[U(x_0,y_0,0)]\hat{H}(f_x,f_y;d)\right\} \tag{4.6}$$

Back propagation is then given by :

$$U(x_0, y_0, 0) = \mathscr{F}^{-1}\left\{\mathscr{F}[U(x, y, d)]\hat{H}(f_x, f_y; d)^{-1}\right\} \tag{4.7}$$

The selection of a scalar diffraction method depends on the propagation distance, the sensor size and its pixel size, which will be introduced in the next section.

4.3 Scalar diffraction algorithm

In this section the scalar diffraction algorithm which has been applied is introduced. The theory of scalar diffraction methods has been introduced in Sec. 2.1.2. The most commonly used propagation method in the far field regime is the single Fourier transform based Fresnel method (SFT-FR). Since only a single Fourier transform is needed, it has on of the fastest speed.

In this work the scalar diffraction method has been used for the auto-focusing algorithm. Such an algorithm aims to detect the image focusing position by evaluating characteristic parameters from the propagated image. Because the parameter is compared among the numerous images at different propagation distance, the propagation algorithm with a constant sampling rate (which is not related to the propagation distance) is preferred.

The sampling rate of the SFT-FR method is related to the propagation distance as described in Eq. 4.8. Δp and Δp_0 are the pixel size on the target and original plane, N is the pixel number of the image and d is the propagation distance. Zero-padding can be used depending on the propagation distance. However, the zero-padding process can increase significantly the computation time for long propagation distances. F. Zhang and I. Yamaguchi introduced a two-steps SFT-FR method which has an adjustable magnification [132]. But this method does not satisfy the Shannon theorem [20].

$$\Delta p = \frac{\lambda d}{N \Delta p_0} \tag{4.8}$$

The convolutional Fresnel method based on double Fourier transform (DFT-FR) and the ASM method has a constant sampling rates which are independent to the propagation distance. But they are not suitable for the long distance calculations because of the aliasing of the optical transfer function (OTF). Their OTF are written as:

$$\hat{H}(f_x, f_y; d)_{Fresnel} = \exp\left\{ jkd \left[1 - \frac{\lambda^2}{2}(f_x^2 + f_y^2) \right] \right\} \tag{4.9}$$

$$\hat{H}(f_x, f_y; d)_{ASM} = \exp\left[jkd \sqrt{1 - (\lambda f_x)^2 - (\lambda f_y)^2} \right] \tag{4.10}$$

The local frequency is noted as u with $f = \sqrt{f_x^2 + f_y^2}$., it can be written as :

$$u_{DFT-FR} = d\lambda f \tag{4.11}$$

$$u_{ASM} = \frac{f\lambda d}{\sqrt{1-\lambda^2 f^2}} \tag{4.12}$$

The maximum frequency of the discrete angular spectrum is $f_{max} = \frac{1}{2\Delta p_0}$. The two times zero padding is usually applied to avoid the aliasing of the convolution. In this case, the sampling rate of the discrete angular spectrum is $\Delta f = \frac{1}{2N\Delta p_0}$. According to the Shannon sampling theorem :

$$u_{max} \leq \frac{1}{\Delta f} \tag{4.13}$$

So the maximum propagation distance of DFT-FR and ASM are calculated as:

$$d_{DFT-FR} \leq \frac{2N\Delta p_0^2}{\lambda} \tag{4.14}$$

$$d_{ASM} \leq 2N\Delta p_0^2 \sqrt{\frac{1}{\lambda^2} - \left(\frac{1}{2\Delta p_0}\right)^2} \tag{4.15}$$

Fig. 4.7 is the cross section of the ASM OTF, it can be observed that, after the f_{limit} aliasing starts to appear.

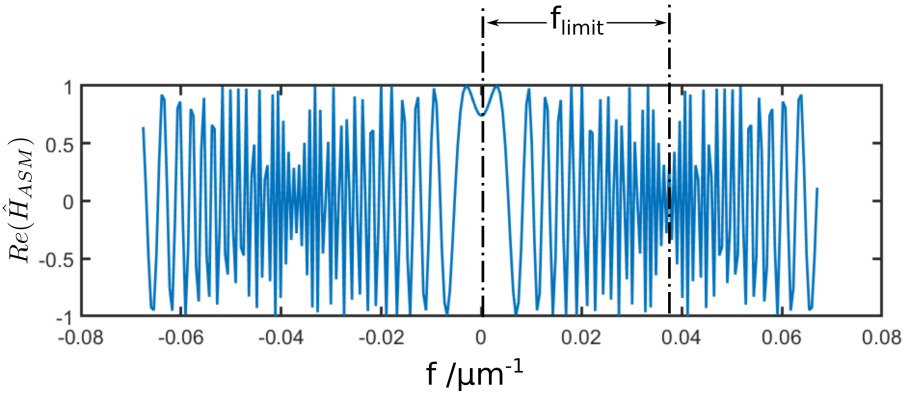

Fig. 4.7 The cross section of the ASM OTF. Only the real part is shown.

The f_{limit} of DFT-FR and ASM are written as:

$$DFT-FR: \quad f_{limit} = \frac{1}{2(\Delta f)\lambda d} \tag{4.16}$$

$$ASM: \quad f_{limit} = \frac{1}{\lambda\sqrt{[2(\Delta f)d]^2+1}} \tag{4.17}$$

K. Matsushima and T. Shimobaba introduced the Band-Limited Angular Spectrum Method (BL-ASM) which eliminates the aliasing of the ASM OTF by limiting the bandwidth of the OTF to f_{limit} [133]. This method has a constant sampling rate and requires only a single step propagation. According to the ASM theory, the maximum frequency arrives on the sensor plane f_{sensor} is written as [133]:

$$f_{sensor} = \frac{1}{\lambda\sqrt{\left(\frac{2d}{W_x+S_x}\right)^2+1}} \tag{4.18}$$

The f_{sensor} attains to its maximum when the aperture width W_x equals to the sensor width S_x.

$$f_{sensor} \leq \frac{1}{\lambda\sqrt{\left(\frac{d}{W_x}\right)^2+1}} = \frac{1}{\lambda\sqrt{\left(\frac{d}{Np_0}\right)^2+1}} = f_{limit} \tag{4.19}$$

According to Eq. 4.19 f_{limit} is always larger than the f_{sensor}. So, the bandwidth limitation does not cause lost of effective information of the image.
Fig. 4.8 are the diffraction results of a circular aperture using DFT-FR, ASM and BL-ASM. The aperture size is 512*512 pixels with a pixel size of 7.4μm. The wavelength is 850 nm. The maximum propagation distance d_{limit} of DFT-FR and ASM method is around 6.6 cm. In simulations, the diffraction distance is ten times larger than d_{limit}. In the results calculated with DFT-FR and ASM, the fringes caused by aliasing can be clearly observed while they are eliminated on the result calculated by BL-ASM.

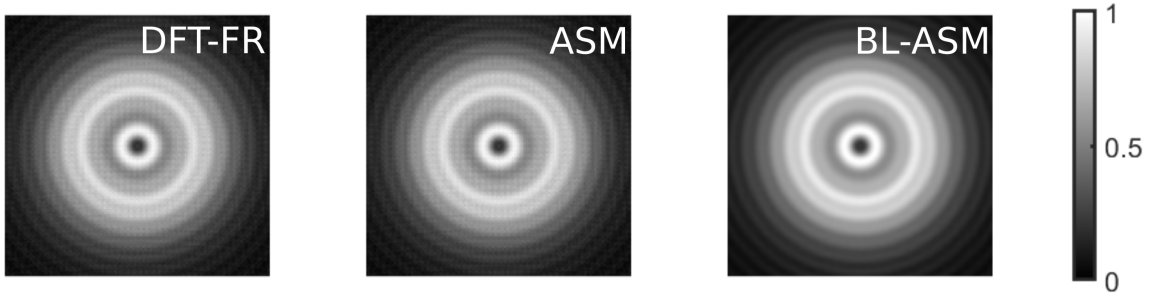

Fig. 4.8 The scalar diffraction of a circular aperture. The aperture diameter is 3 mm. $\lambda = 850$ nm, the propagation distance is $10\times d_{limit}$.

The BL-ASM algorithm is then tested with the LI-DHM hologram shown in Fig. 4.4. The point source illuminated LI-DHM can be reconstructed by means of plane wave diffraction.

Here the reconstruction distance has been obtained by the auto-focusing algorithm. The reconstruction distance of this hologram is 0.99875 m which is much longer than the maximum propagation distance of the conventional ASM method (0.34 m). The reconstruction result is shown in Fig. 4.9. The sphere sample is successfully reconstructed without the aliasing. Note that the circular diffraction pattern is due to the twin image noise of the Gabor's inline configuration. It could be eliminate by the phase retrieval algorithm.

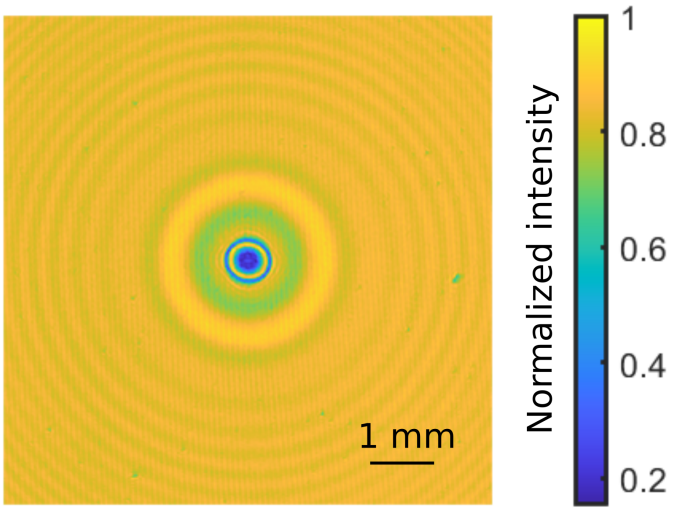

Fig. 4.9 The reconstruction of a LI-DHM hologram by BL-ASM. The reconstruction distance is 0.99875 m.

4.4 Auto focusing algorithm

4.4.1 Introduction to auto-focusing methods

Accurate knowledge of the object plane position is necessary for holographic reconstruction. Such a position is usually hard to be measured by experiment. Consequently an auto-focusing technique which can numerically estimate the axial focus position is necessary. Most of the these algorithms share the same basic idea. Finding a parameter (or a parameter created by a combination of multiple ones) that reaches its extreme value at the sought focus position. During the last decade, numerous auto-focusing methods for DHM have been invented. In 2013 Ilhan *et al.* [134] compared 11 sharpness focusing metrics and selected four among them to study the effect of scaling acceleration method. Then in 2016 Fonseca *et al.* [135], reviewed and compared fifteen auto-focusing metrics. They have classified the metrics into three groups: spatial based metrics, transform based metrics and sparsity based metrics. But they left out the energy based auto-focusing metrics which are commonly used in DHM. In addition to these techniques, a learning based auto-focusing method has been proposed [136]. Compared to conventional auto-focusing metrics, it has an impressive advantage in speed and accuracy. However, conventional metrics are still necessary to build the database consisting of holograms and their true focus distance. Several representative metrics will be reviewed basically according to Fonseca's classification with supplementary energy based metrics and some other methods.

Spatial based metrics Spatial based metrics evaluate directly the spatial characteristics of the reconstructed image. Usually the sharpness of image is taken into account. Langehanenberg *et al.* [137, 138] have done numerous research on this type of auto-focusing metrics and its application to DHM system for biological samples [135].
Typically the gradient (GRA) and Laplacien (LAP) are calculated to qualify the sharpness which is actually an edge detecting process. The derivative of the image is then computed in order to evaluate the focusing position. It reaches a maximum for amplitude objects and a minimum for phase objects [134]. The derivative methods are fast for calculation. But they also have some serious limitations. First, they are sensitive to speckle noise especially for the LAP based methods. Nevertheless the coherent diffraction of light in holography results in complex interference patterns. So, different from incoherent imaging the sharpness or the high frequencies will not necessarily diminish with defocusing [139]. Also the twin image effect for inline configurations will also disturb the focusing process.
Apart from the derivative of the image, histogram [140] and correlations of adjacent pixels

[141] can be used to qualify the sharpness of reconstructed images. But, since they also evaluate the focus position by sharpness like derivative based methods, the same problem as for other spatial based methods will occurs when applied to holography.

Energy based metrics In 2006, F. Dubois introduced an auto-focusing method based on the analysis of amplitude [142]. Based on the fact that the total energy is conserved during propagation, he has deduced that the sum of amplitudes (L1 norm) reaches its maximum for pure amplitude objects and its minimum for phase objects. W. Li *et al.* introduced an equivalent algorithm by calculating the L1 norm with a modified Fourier transform [143]. The latter is computed one time during the whole process, so that auto-focusing can be achieved in real time. This metrics have the advantage of being easily implemented with fast calculation speed. But they are only suitable for well isolated samples whose diffraction pattern occupies a relatively small area on hologram. Also they are not suitable for a spherical reference wave.
C. Trujillo and J. G. Sucerquia proposed a method which is also based on energy conservation that can be applied with a spherical reference wave [144]. Different from the aforementioned methods which are focused on energy conservation on the full image, C. Trujillo *et al.* considered only a localized area around target samples. They suggested that since the energy is conserved throughout diffraction, the focused position is located where the smallest surface can enclose a pre-defined amount of energy. The surface is normalized by a propagation factor so that the metrics can be also applied with a spherical reference wave. Its computational complexity is larger than most of other metrics since a loop is needed on every backpropagated position to search the area size.

Transform based metrics Transform based metrics are the methods that transform back-propagated image in specific spaces instead of the spatial space to extract interesting characteristics. By evaluating them when scanning along the optical axis, the exact focus position can be found. Various types of transformations have been used to serve the purpose of finding such a position [145, 140]
Comparing to spatial based methods and energy based methods, transform based methods are usually more robust. And they always have a better unimodality. However, the computation time for transform based metrics is usually higher because of the additional transformation step [135].

Sparsity based metrics In general, the principle of sparsity is to represent a phenomenon with fewest parameters. In the case of digital imaging, this means to represent an image using as few pixels as possible. P. Memmolo proposed that the reconstruction of a hologram is sparsest at refocused location[146, 147]. The Fresnel transform based method proposed by M. Liebling was based on the same idea [145]. When reconstructing at the best focus location, the Fresnel transformation intensity is localized on the smallest Fresnel coefficients set, which is equivalent to say that the reconstruction is sparsest. P. Memmolo suggested that the sparsity of refocused image can be evaluate directly using Tamura coefficient (TC) and Gini's index(GI) without additional transformation.

$$TC: \quad TC = \sqrt{\delta(I)/ < I >} \tag{4.20}$$

$\delta(I)$ is the standard deviation, $< I >$ represents the mean of the image intensity.

$$GI: \quad GI = 1 - 2\sum_{k=1}^{N} \frac{a_k}{\sum(I)} \left(\frac{N-k+0.5}{N} \right) \tag{4.21}$$

a_k is the k-th value of sorted image intensity. Y. Zhang *et al.* recently introduced a novel metrics called Sparsity of Gradient (SoG) which combined the sparsity metrics along with gradient metrics [139]. Instead of calculating sparsity directly of intensity image, they applied the sparsity operator to the gradient modulus of the complex reconstructed wave front. $SoG(U) = S(|\Delta(U)|)$. S is the sparsity operator, Δ represents the gradient operator, U is the complex reconstructed wavefront. It shows a better performance in both accuracy and robustness than metrics with standard gradient or sparsity only. Also, by applying the gradient operator directly on wave front rather than intensity, SoG has a consistent behavior for both amplitude and phase objects. SoG reaches its maximum at focus point for both of them.The performance of the GI and TC parameter has been evaluated [148].The results suggested that for extremely sparse object, TC has a better sensitivity to noise. At the same time, region of interest (ROI) shouldn't be too large compared to the size of the object. In contrast, for dense object, larger ROI results in better auto-focusing accuracy for both operators. This is actually easy to understand. For sparse object with larger ROI, more noise appears meanwhile, for dense objects, larger ROI means more objects are included.

4.4.2 Selection of the auto-focusing method

4.4.2.1 Test on the LI-DHM hologram

The amplitude (AMP), Gradient (GRA) and SoG metrics have been tested on a LI-DHM hologram. As for the SoG metric, the TC criteria is selected instead of the GI because the latter is more time consuming since the intensities need to be sorted. The expressions of these metrics are given as follow :

$$AMP: \quad AMP(I) = \sum |I(x,y;d)| \tag{4.22}$$

$$GRA: \quad GRA(I) = \sum |\Delta I(x,y;d)|^2 \tag{4.23}$$

$$TC: \quad SoG_{TC}(g) = \sqrt{\delta(|g(x,y;d)|) / < |g(x,y;d)| >} \tag{4.24}$$

where $I(x,y;d)$ represents the reconstructed wavefront, $g(x,y;d)$ is the gradient of $I(x,y;d)$, Δ is the gradient operator, δ denotes the standard deviation, and $<>$ stands for ensemble average. The transparent sphere sample is a phase object. So the AMP and GRA reach their minimum at the focusing position. On the other hand, SoG metric will reach its maximum. The LI-DHM hologram shown in Fig. 4.4 is captured with a point source. It will be reconstructed with a plane wave and an equivalent propagation distance [149]. As a result, the reconstructed image is magnified. The equivalent propagation distance is calculated by:

$$d_{pl} = \frac{d_{sph} d_{source}}{d_{source} - d_{sph}} \tag{4.25}$$

The d_{pl} is the plane wave propagation distance, d_{sph} represents the spherical wave propagation distance and d_{source} is the distance between the point source and the camera. d_{source} is estimated to 21.775 cm. The d_{pl} is around 1 m. The BL-ASM method as introduced in the last section is applied.

The normalized curve of the auto-focusing metrics is given in Fig. 4.10. The focusing distance is converted to the spherical wave propagation distance. The SoG metric shows best convexity. The estimated focusing distance is 17.88 cm. The AMP and GRA presents multiple local minimums around the focusing position which may be due to the twin image effect of inline hologram. Precise focusing position is estimated to be 17.881 cm by the SoG metric using the sequential quadratic programming (sqp) method [150].

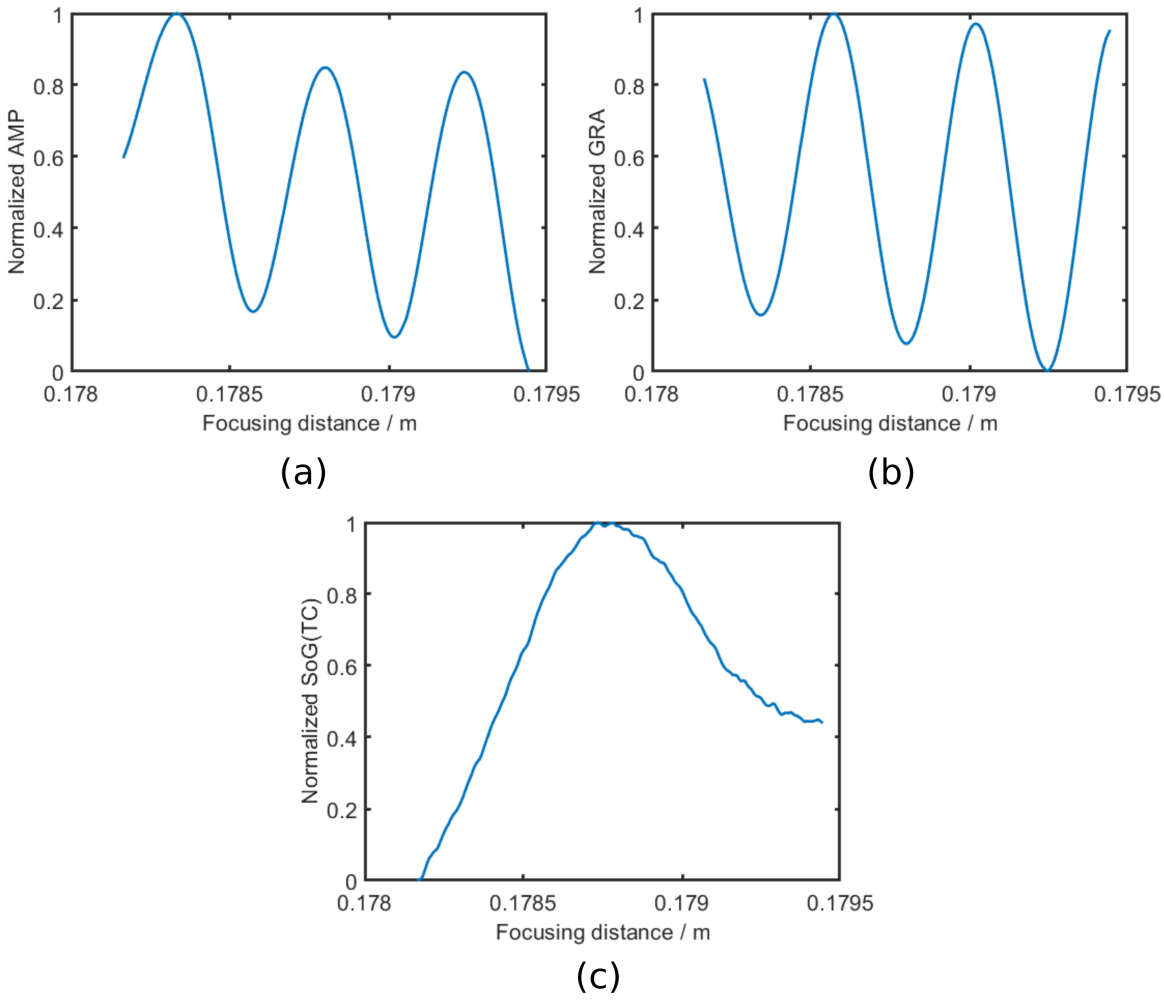

Fig. 4.10 Normalized auto-focusing metrics as functions of the propagation distances. (a) AMP (b) GRA (c) SoG with TC criteria

For the sake of validation, SoG is applied to two additional holograms. The sample is translated along propagation direction with distances of 100 µm and 200 µm. The estimated focusing position are 17.871 cm and 17.860 cm respectively. 10 µm error should be acceptable over 17.88 cm.

The transparent sphere sample has a regular shape and may be described by a two dimensional phase transmission function. Such a function which describes the phase shift of the transmitted light is given as:

$$\begin{aligned} P(x,y) &= P_{max}\sqrt{1-\frac{x^2+y^2}{R^2}} \quad x^2+y^2<R^2 \\ &= 0 \quad \text{otherwise} \end{aligned} \tag{4.26}$$

where the P_{max} is the maximum phase shift, R is the sphere radius. Based on the two dimensional model, the parameter-based inverse problem method is applied to estimate the focusing distance [38]. The cost function is written as :

$$\ell(\vec{p},\alpha,\beta) = \sum_x \sum_y W(x,y) \cdot [I_H(x,y) - \alpha I_{simu}(x,y;\vec{p}) + \beta]^2, \tag{4.27}$$

where $I_{H(x,y)}$ is the intensity distribution of the captured hologram, $I_{simu}(x,y;\vec{p})$ is a simulated hologram distribution, by numerically propagating the transmission function to the distance d. $W(x,y) = 1/\mathrm{var}[\mathrm{I_H(x,y)}]$ is a weighted mask that represents the quality of pixels by their inverse variance (var is the variance). It is set to zero for the pixels that are not involved. α and β are the parameters related to the sensor. They could be estimated analytically. Vector $\vec{p} = (x_p, y_p, d_p, D_p)$ includes the geometrical parameters of the sphere. x_p,y_p are the lateral position of the sphere center that equals to the center of the diffraction pattern. d_p is the axial position that needs to be estimated. And D_p is the diameter of the sphere. It is a known parameter measured by a dark field microscope.
d_p is estimated to be 17.878 cm by the parameter based inverse problem method. It validates the result given SoG.

4.4.2.2 Appling SoG auto-focusing to SPR-DHM hologram

The SoG metric shows a good performance with LI-DHM. It has been selected and tested on SPR-DHM holograms. Reconstruction has been achieved with the method introduced in Sec.4.2. The intensity distribution of the reconstructed image is illustrated in Fig.4.11. The SoG metric is applied and the curve of the TC criteria is shown in Fig.4.12. The maximum retrieved by sqp locates at 5.99 mm. As what has been done during the test on LI-DHM, two other holograms has been captured at different axial locations. Here, the object that needs to be reconstructed is the image generated by the SPR-DHM . Instead of displacing the sample as in LI-DHM test, the camera is displaced 5 mm before and after it original position. The estimated focusing distance are 0.12 mm and 8.18 mm. The error reaches 2 mm. It may due to the large depth of focus (DoF) on the image side. The DoF is defined as $DoF = \lambda/NA^2$, wavelength λ is 850 nm and NA is the one of the imaging lens. The diameter of image is estimated to be around 16.5 mm and the focusing distance is 600 mm. The corresponding NA is then equals to 0.0138, giving a DoF about 4.5 mm. In order to validate the assumption, the DoF of the image plane is measured experimentally. The camera is installed on a translation stage and displaced 8 mm with a step of 1 mm. The SoG of the reconstructed hologram is evaluated at each location. As shown in Fig.4.13, the DoF estimated by the full width

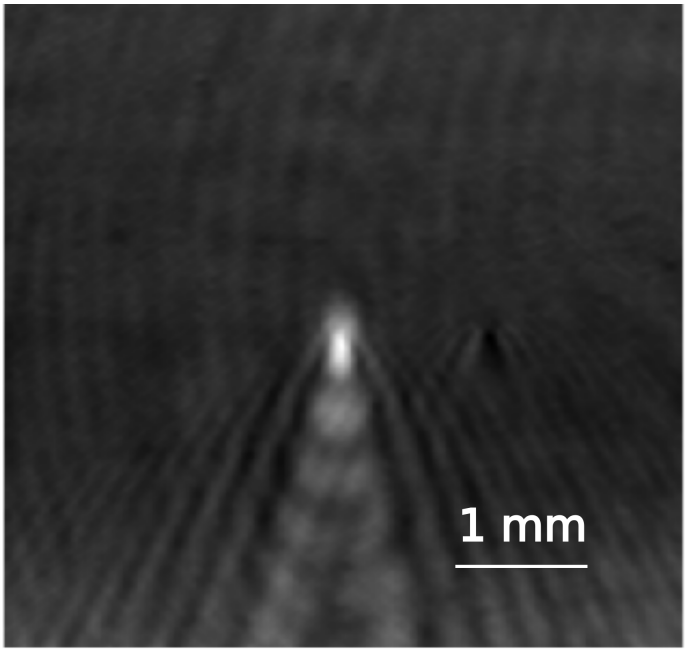

Fig. 4.11 Intensity of reconstructed SPR-DHM hologram

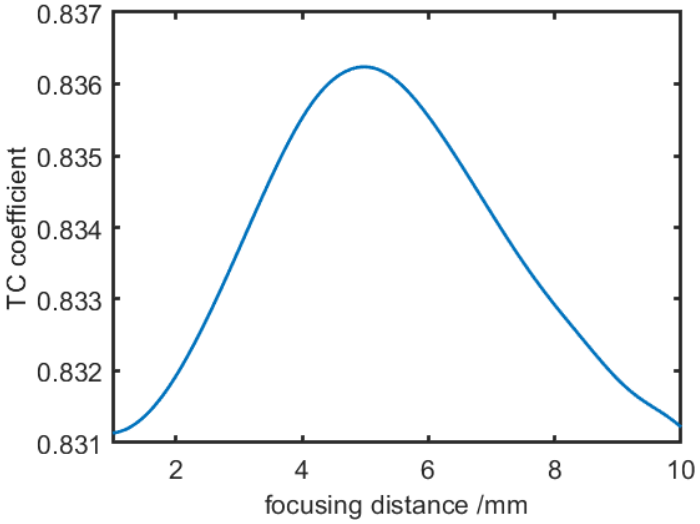

Fig. 4.12 TC curve of SPR-DHM hologram

half maximum (FWHM) of the SoG curve is equal to 3.4 mm. This could explain the low accuracy. Also millimeter scale for DOF means the focusing could be adjusted manually. Instead of using the numerical auto-focusing process, the image lens could be installed on a translation stage to manually adjust the focus location in our SPR-DHM setup.

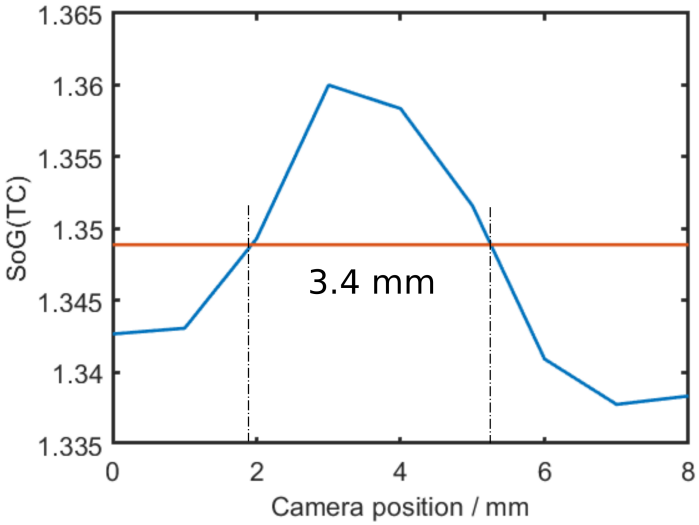

Fig. 4.13 SoG(TC) at each location. The DoF is evaluated using the FWHM of the curve which equals to 3.4 mm.

4.5 The unwrapping algorithm

The reconstructed phase is wrapped ranging from $-\pi$ to π. Such a wrapping results in discontinuities on the phase map. An unwrapping algorithm needs to be applied to estimate the continuous phase distribution.

The simplest unwrapping algorithm scans the image line by line or column by column. A modulo 2π is added or substructed when a phase difference between adjacent pixels is larger than a pre-defined threshold. Such an algorithm works well for noise free phase images. But it cannot handle noisy images. It will propagate the noise to the whole line or column. In order to solve this problem, more advanced unwrapping algorithms are needed.

In this section three algorithms are tested: the Matlab "unwrap" algorithm based on the simplest continuous path (CP) unwrapping method, a two-dimensional phase-unwrapping algorithm based on sorting by reliability following a noncontinuous path (2D-SRNCP) [151], and the robust two-dimensional phase unwrapping using a fast cosine transform (RFT) [152]. The last two algorithms represent two categories of unwrapping methods. The 2D-SRNCP unwraps the pixels based on their reliability (or quality). It unwraps the pixels with the highest reliability first then the lower ones. It then classifies the the unwrapped pixels into groups and unwraps the border of the groups according to the group reliability. So different from the simplest unwrapping, the 2D-SRNCP follows a noncontinuous path. The influence of the noisy pixels are confined into its adjacent area instead of propagating to the whole path.

The RFT method on the other hand transfers the unwrapping problem into solving a least square solution of the unwrapped phase. This solution is equivalent to a solution of the two dimensional Poisson's equation with Neumann boundary conditions [152]. The Poisson's equation is solved using the fast cosine transform. The least square solution will average the influence of noisy pixels to its adjacent area. A weighted mask could be applied if the noisy areas are known a priori. Besides, the weighted Poisson's equation is solved by an iterative method. It is noted as weighted RFT (W-RFT).

The wrapped phase response of the 149 µm transparent glass sphere acquired by LI-DHM is used to test the performance of the aforementioned unwrapping algorithms. It is a 5.6x magnified image due to the magnification of the LI-DHM. The continuous path (CP) method uses the matlab 'unwrap' function. The 2D-SRNCP is coded in C language by M. Mullen [153]. The RFT and W-RFT are coded in Matlab based on the algorithm 1 and 2 in [152].

Fig. 4.14(a) is the wrapped phase response. The phase is retrieved by an iterative phase retrieval algorithm and can be regarded as noise-free. In Fig. 4.14(b), gaussian noise is added

inside a 5x5 area. The signal to noise ratio (SNR) is 12.7 dB.

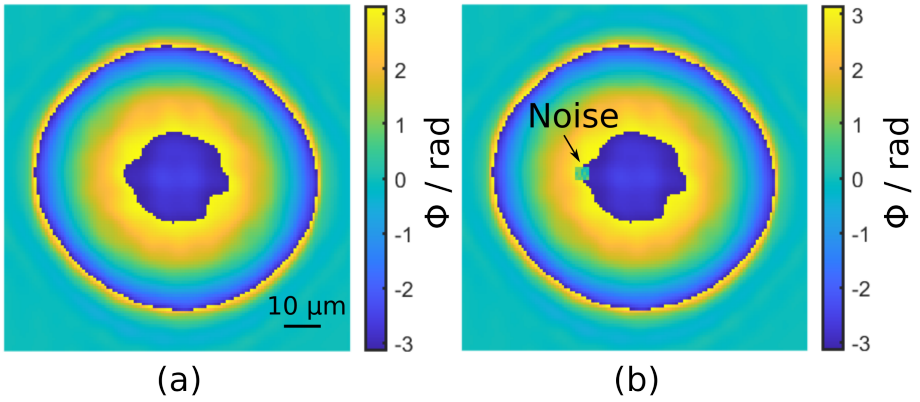

Fig. 4.14 Wrapped phase of a 149 µm transparent sphere. (a) Wrapped phase response (b) Wrapped phase response with noise.

All three unwrapping algorithms (CP, 2D-SRNCP, RFT) can successfully unwrap the noise-free wrapped phase. The unwrapped phase is shown in Fig. 4.15.

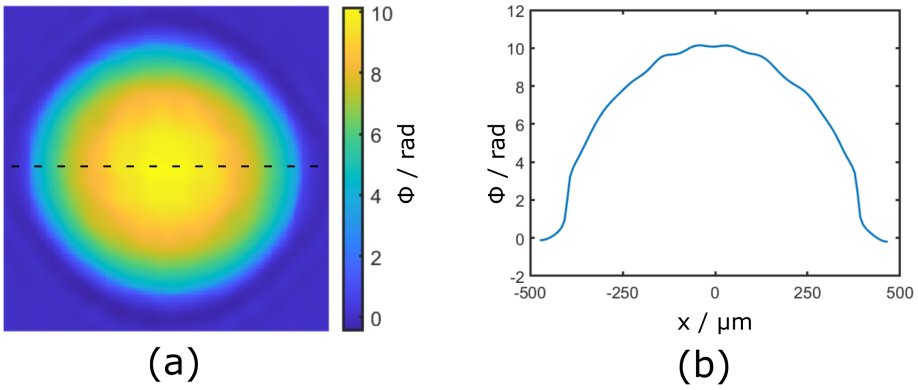

Fig. 4.15 Unwrapped phase map of the noise free wrapped phase. (a) Unwrapped phase map (b) Cross-section at the center (dashed line in (a)) of the unwrapped phase.

The algorithms have also been tested with noisy wrapped phases. The results are shown in Fig. 4.16. The CP algorithm propagates the noise error to the whole column. The 2D-SRNCP and RFT methods can both confine the noise in its adjacent area. The calculation speed is evaluated by unwrapping a 1700*1700 phase map. 2D-SRNCP takes 1.66 seconds meanwhile RFT takes 0.89 second. 2D-SRNCP is slower because it needs to sort the reliability of the pixels before unwrapping.

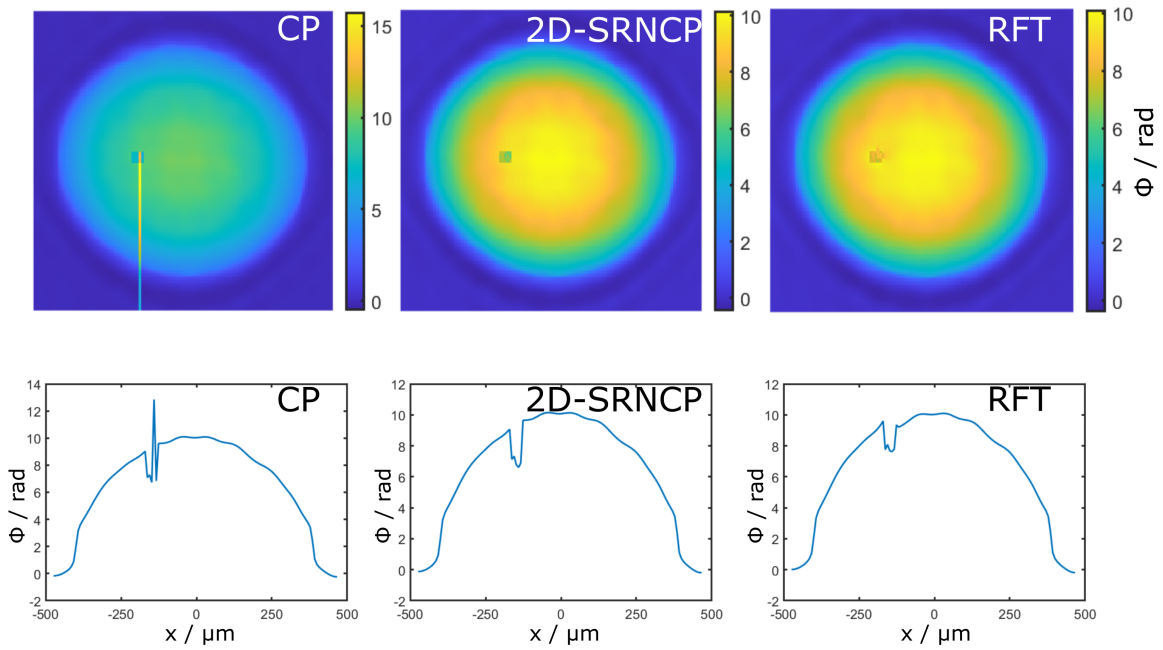

Fig. 4.16 The unwrapped phase map of the noisy wrapped phase. The algorithm used is noted on the corresponding result.

The influence of the noise can be further reduced by the W-RFT algorithm. Fig. 4.17(a) is the unwrapped result after 40 iterations. The algorithm converges after 5 iterations. It could be observed from Fig. 4.17(b) that the W-RFT can effectively reduce the disturbance. As shown by the test, the 2D-SRNCP and RFT algorithms can both handle noisy images. The computation time of RFT is lower than the one of 2D-SRNCP. And the W-RFT could reduce the disturbance if the noise distribution on image is known. It should be mentioned that while the RFT method is faster and accommodate well noisy pixels, it can not solve singular points on the phase image. The least square solution average the singularities and smooth its phase variations.

In practice these algorithms are selected according to the phase image characteristics. In our work, phase response of the SPR-DHM is generally smooth. Singular points are not likely to appear. RFT and the W-RFT algorithms have been selected.

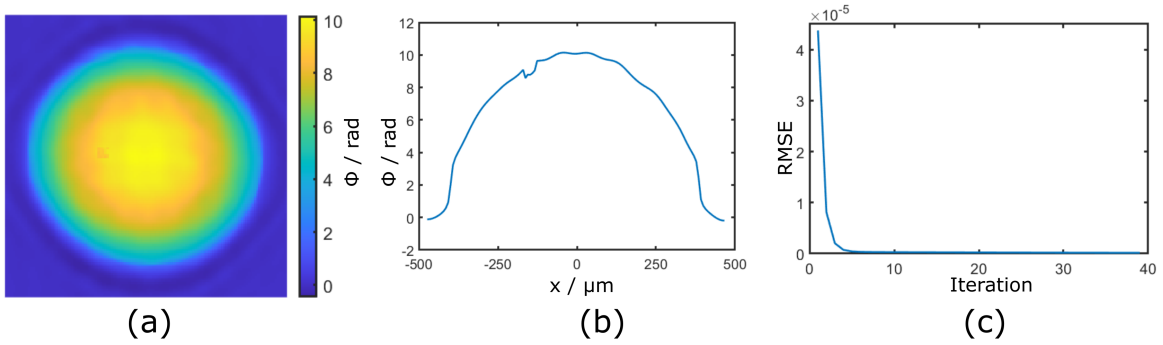

Fig. 4.17 The unwrapped phase map by W-RFT algorithm (a) The unwrapped phase image (b) A cross-section in the center (c) The convergence curve, Root Mean Square Error(RMSE)

4.6 Conclusion

In this chapter, numerous algorithms have been introduced including off-axis digital reconstruction, BL-ASM propagation method, SoG auto-focusing method and RFT unwrapping method. The SoG method although showing a good performances on LI-DHM hologram, presents a low accuracy for SPR-DHM hologram. This is due to the large depth of focus (DoF) or our imaging setup. Consequently, focusing will be adjusted manually by displacing the imaging lens.

Chapter 5

Tests and experiments with the SPR-DHM

5.1 Sample preparation

The sample is fabricated by the Physical Vapor Deposition (PVD) method in a cleanroom. About 3 nm of Cr adhesion layer and 45 nm of gold layer is coated onto an 85 μm coverslip made by SCHOTT (D263® glass). The coverslip is extremely fragile and a holder has been designed then fabricated by 3D printing.

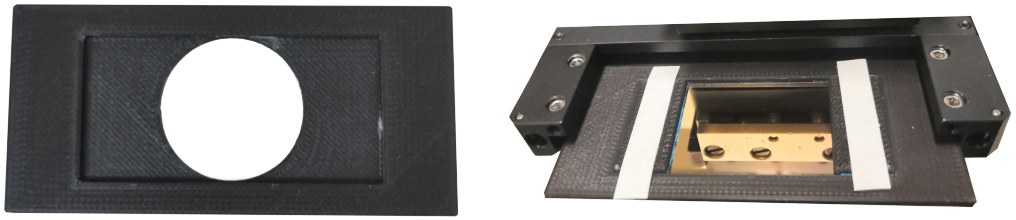

Fig. 5.1 The 3D printed sample holder.

5.2 SPR-DHM imaging of gold-air interface

5.2.1 Intensity response of the SPR microscope

In order to have a better understanding of the holographic images of the SPR, the intensity responses are analysed first.

As introduced in the Sec. 3.2, the incident angle is controlled by the focusing position at the back focal plane of the microscope objective. The illumination subsystem is installed on a translation stage to control such a focusing. The position where SPR is stimulated needs to be detected first.

A serie of images are captured when scanning p-polarized illuminations throughout the BFP. Images before, at and after resonance are shown in Fig. 5.2. On the image at resonance, the diffraction of the SPW by dust on the gold surface can be observed.

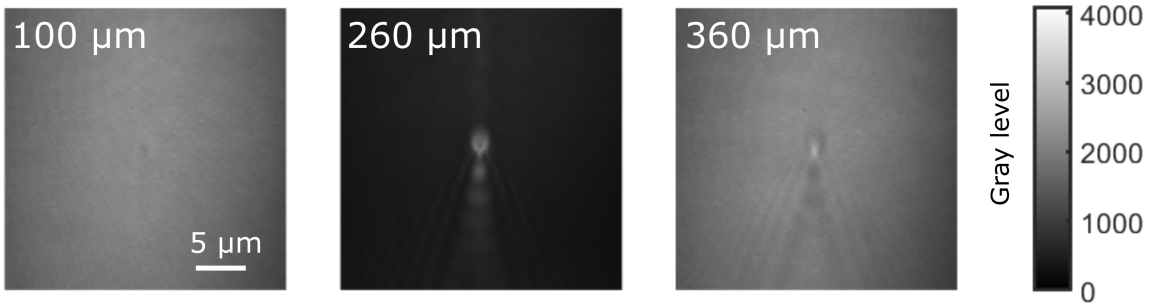

Fig. 5.2 Images captured at different focusing positions. 0 µm is the starting point that locates before the critical angle, 260 µm is strongest resonant location and 360 µm is out of resonant.

10 x 10 pixels locate near the center of image have been selected (away from the diffraction). Their average intensity is used to evaluate reflectivity. The latter is estimated by dividing the intensity of each image by their maximum (such an intensity is regarded as the intensity for total reflection). The result is shown in Fig. 5.3. Fig. 5.3(a) is the curve obtained by experiments, and Fig. 5.3(b) is the simulated reflectivity as a function of the focusing position ρ on BFP. $\rho = 0$ corresponds to the optical axis. The relation between the emitting angle θ and ρ of for an aplantic microscope objective is written as [154]:

$$\rho = f n_{oil} \sin(\theta) \tag{5.1}$$

where n_{oil} is the refractive index of the immersion oil (which is approximately equals to the RI of the coupling glass), and f is the focal distance of the objective which is equals to 3

mm.

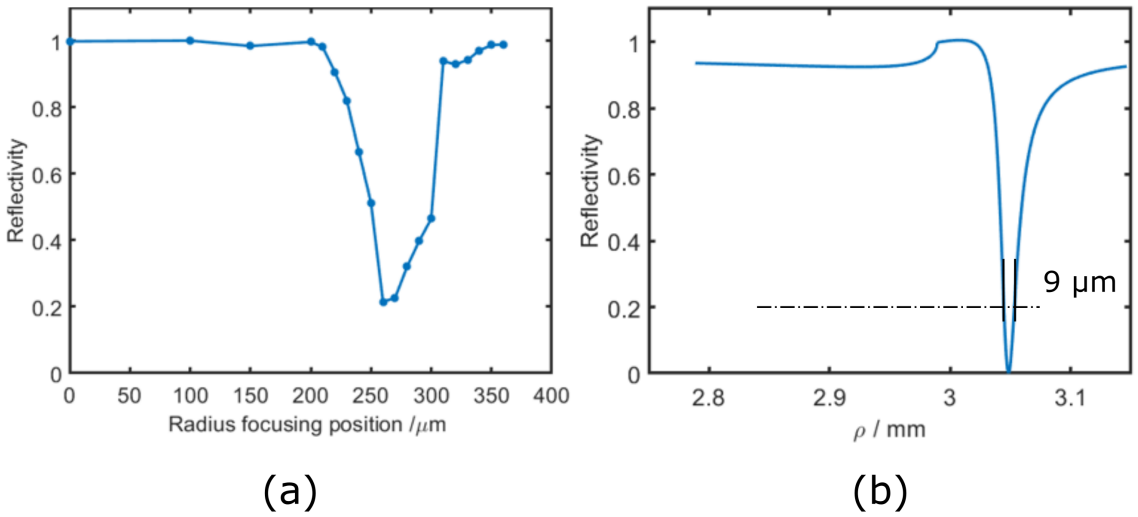

Fig. 5.3 Reflectivity curve of the gold-air interface (a) The reflectivity in function of the radius focusing position measured by experiment, 0 μm corresponds to $\rho = 2.8$ mm in experiment. (b) The reflectivity as a function of incident angle calculated by simulation.

The distance between the points with 20 % reflectivity on the simulation curve is 9 μm. It agrees with the measured distance which is about 10 μm. As the minimum measurable displacement of the translation stage is 10 μm, the maximum absorption does not appear on the curve.

At the resonance position, the illumination is changed to s-polarization by the half wave plate. The captured image is shown in Fig. 5.4(a). Since SPR only exists for p-polarized illumination, diffraction of the SPW does not appear on the s-polarized image. It is then used as the reference to normalize SPR images at resonance. Focusing is adjusted to the captured images in-focus. Fig. 5.4(b) is the normalized image.

Fig. 5.5(a) is a cross-section near the edge of the normalized SPR image. Variation of the reflectivities across the image are observed. Such a phenomenon is due to the divergence of the illumination as introduced in Sec.3.2. Due to the diffraction limit, the focused illumination on the BFP is a Airy pattern, instead of a perfect spot. As a result, the illumination on the interface is divergent as shown in Fig. 5.5(b).

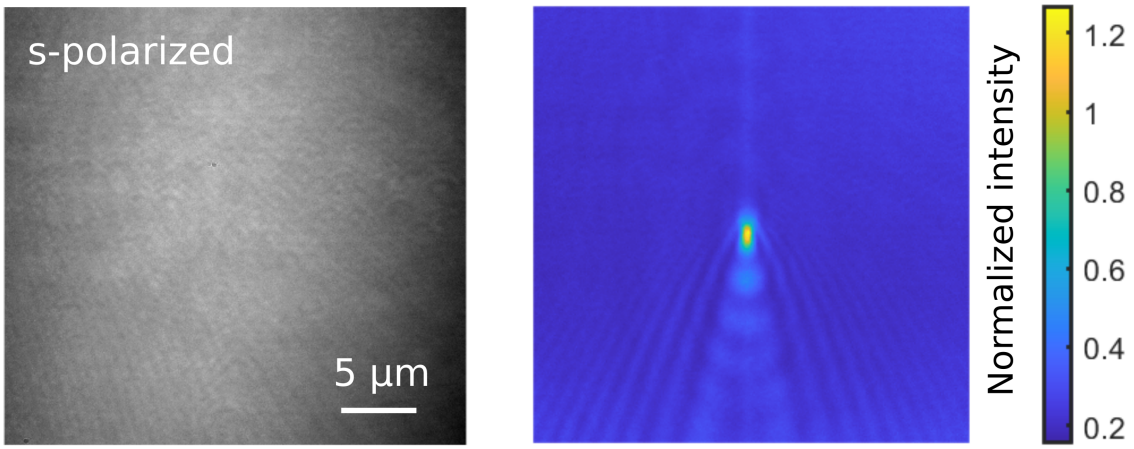

Fig. 5.4 Normalized SPR image and image under s-polarized light (a) Illumination is turned to s-polarization (b) Normalized SPR image.

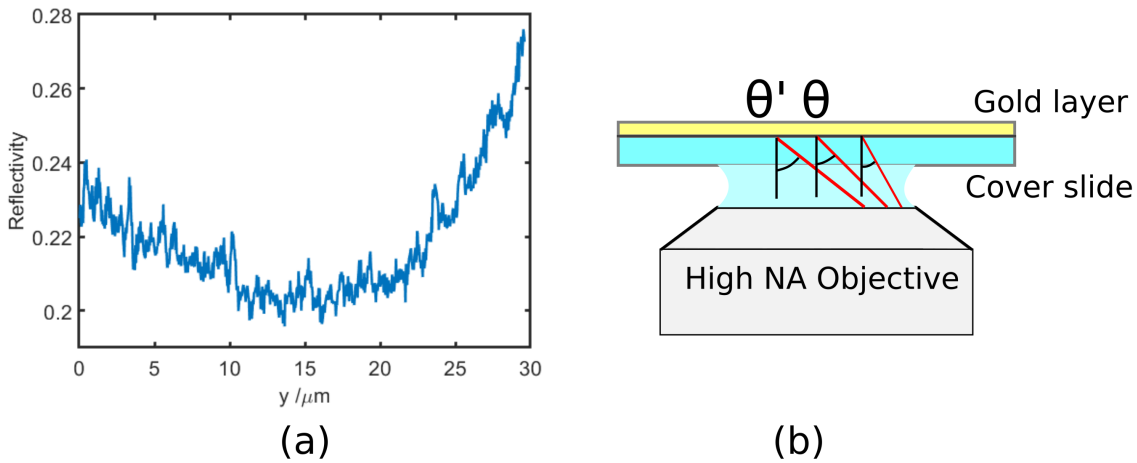

Fig. 5.5 Cross-section near the boarder of the normalized SPR image (a) The cross-section (b) Divergent incident light.

5.2.2 Spectral analysis of the SPR intensity image

In this section, the spectral of SPR image are analysed. A spectrum(logarithmic scale) is shown in Fig. 5.6. On the p-polarized image where the SPR is stimulated, two ring shape are observed. The larger ring corresponds to the displaced objective aperture that can also be observed at the s-polarized image. The smaller one indicates stimulation of the SPR. This ring does not appear on the s-polarized image as SPR is not stimulated. The theoretical explanation of the ring shape point spread function has been provided by H. Yu *et al* [155]. It comes from the interference between the SPW diffracted by the object and undiffracted part. The ring diameter is related to the wave number k_{spp} of the surface plasmon polariton. The center locates the wave number k_x of the stimulation wave. Its thickness corresponds to the SPW propagation distance L_x [156].

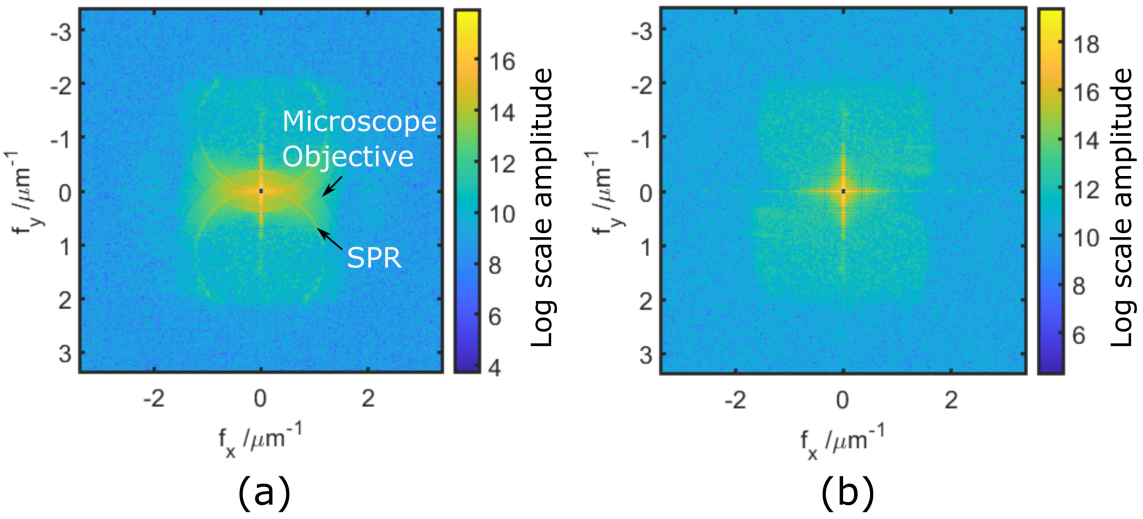

Fig. 5.6 P-polarized and s-polarized amplitude spectra(logarithmic scale), the 3x3 pixels in center are masked. (a) Spectrum of p-polarized image (b) Spectrum of s-polarized image

The center of the rings on the lower half of the spectrum is estimated to be at $f_x = -0.03\mu m^{-1}, f_y = 1.20\mu m^{-1}$. A cross-section starting from the ring center is shown in Fig. 5.7. The SPR stimulation and the edge of the objective aperture are detected to be at $f = 1.21$ µm^{-1} and $f = 1.59$ µm^{-1} respectively. The theoretical values of these two positions are $f = 1.20$ µm^{-1} and $f = 1.67$ µm^{-1}. The measured SPR stimulation position matches the theoretical one. However, the aperture size of the microscope objective is smaller. This may due to two reasons. Firstly, the noise on the image will lower the contrast at high frequencies. Secondly, the BFP is not fully illuminated. As a result the maximum available bandwidth of

the objective is smaller than the theoretical one. According to the formula of the objective $B = NA/\lambda$: the measured NA would be 1.35.

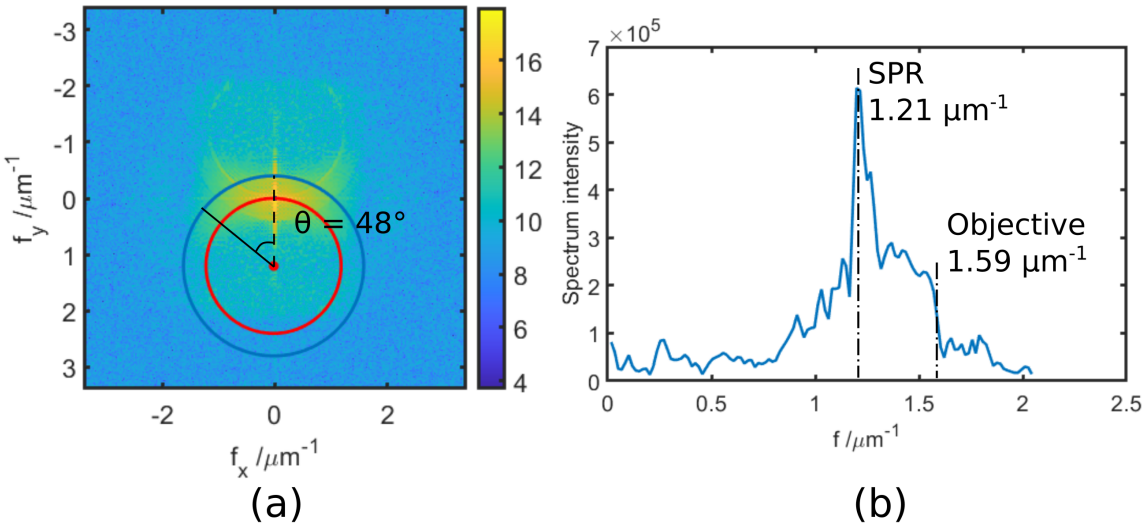

Fig. 5.7 Cross-section of SPR spectrum. (a) Schematic presentation of the cross section location. The red ring is the SPR stimulation and the blue ring is the edge of the objective aperture in the frequency domain . The red dot corresponds to the center of the rings. (b) Cross-section along the black line on (a). The SPR locates at $f = 1.21\ \mu\text{m}^{-1}$ and the edge of the objective aperture is at $f = 1.59\ \mu\text{m}^{-1}$.

5.2.3 SPR-DHM image acquisition and reconstruction

An SPR-DHM hologram of the gold-air interface is captured and reconstructed. The formation of hologram by a Wollaston prism has been introduced in Sec. 3.3.4.The p and s-polarized components of light have been split with an one degree angle. P-polarized light carries the SPR information, and the s-polarized component serves as the reference wave in the hologram formation. They are then combined by a linear polarizer. Fig. 5.8 shows both components split by the Wollaston prism. The polarizer is not installed, so that the two orthogonally polarized components do not interfere. The strong diffraction on the left hand side of the image is the SPR distribution. It has been introduced earlier. On the right hand side, a weaker diffraction pattern is observed. The s-polarized image has been been provided in Fig. 5.4 (a). Such a diffraction pattern does not appear when the Wollaston prism is not installed. So, this pattern is not due to the diffraction of the s-polarized light by the sample. The quartz Wollaston prism has a designed extinction ratio of 10000:1. Due to the alignment condition, the practical extinction ratio is generally smaller than the designed one. So part of the p-polarized component will leak to the s-polarized component.

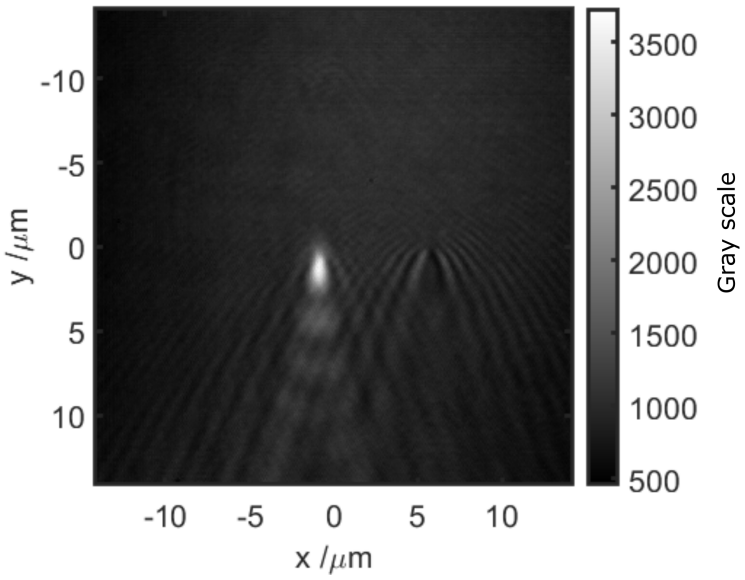

Fig. 5.8 The p-polarized and s-polarized components split by the Wollaston prism.

By adjusting the ratio between the p and s polarizations, the influence of the leaked component may be reduced. The captured hologram and its logarithmic spectrum is illustrated in

Fig. 5.9.

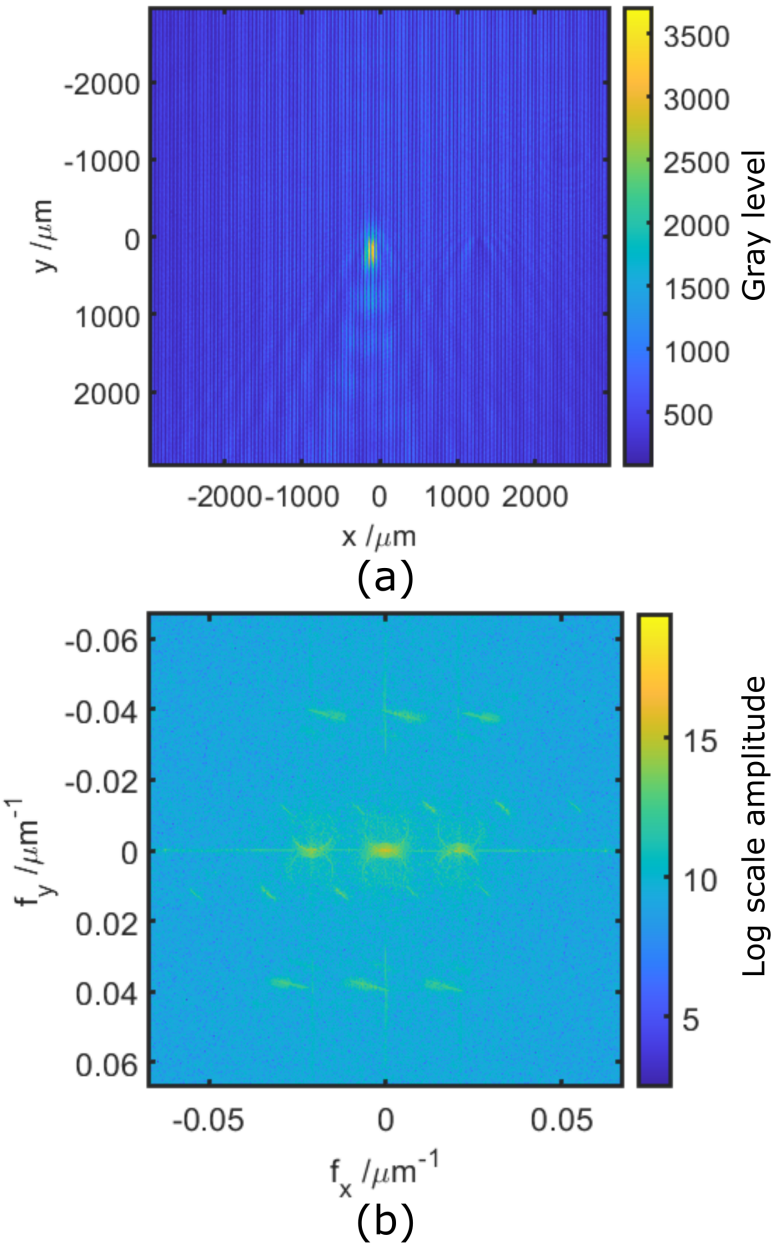

Fig. 5.9 Gold-air interface hologram and its amplitude spectrum. (a) Hologram captured by the camera. Dimensions are those of the image plane rather than the object plane. (b) Amplitude spectrum of (a), the -1, 0 and 1 orders are split by the Wollaston prism.

The first order is extracted with a Gaussian filter. It is then translated to the center of the spectrum. Its inverse Fourier transform is the reconstructed complex wave field $O(x,y)$.

The system focus is adjusted to conjugate the sample plane directly on to the sensor plane. Numerical auto-focusing is avoided. The intensity and phase are $I_{O(x,y)} = |O(x,y)|^2$ and $\phi_{O(x,y)} = \arg[O(x,y)]$. An unwrapping algorithm is applied when the phase shift surpasses 2π. The reconstructed intensity and phase are shown in Fig. 5.10.

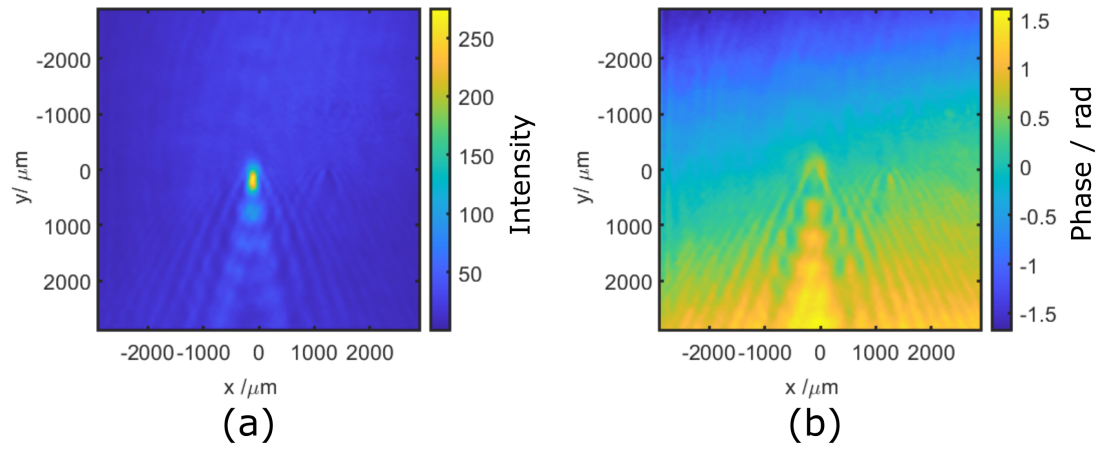

Fig. 5.10 (a) Reconstructed intensity (b) Reconstructed phase

It has been introduced in Sec. 4.2 that the reconstructed complex wave front is modulated by the reference wave because the latter is not a perfect plane wave. The reconstructed wave front may be written as:

$$O_{air}(x,y) = I_p(x,y)I_s(x,y)\exp\{j[\phi_p(x,y) - \phi_s(x,y)]\} \tag{5.2}$$

where the $I_p(x,y)$ and $I_s(x,y)$ are the intensity of the p-polarized object wave and s-polarized reference wave respectively, $\phi_p(x,y)$ and $\phi_s(x,y)$ are their phase shifts. Here in order to remove the modulation from the reference wave as well as the aberration from the illumination on the object, a reference hologram is captured. A drop of water (2 µL) is applied on top of the gold surface while keeping the light angle unchanged. The resonant angle of the gold-air interface is much smaller than the one of the gold-water interface. So the SPR is not stimulated and the illumination is reflected directly. By using such a method, the SPR is removed from the reference hologram while maintaining same reference light and illumination distribution as the SPR hologram [10]. The captured reference hologram is shown in Fig. 5.11.

Similar to the SPR hologram, its reconstruction may be also written in the form of Eq. 5.2.

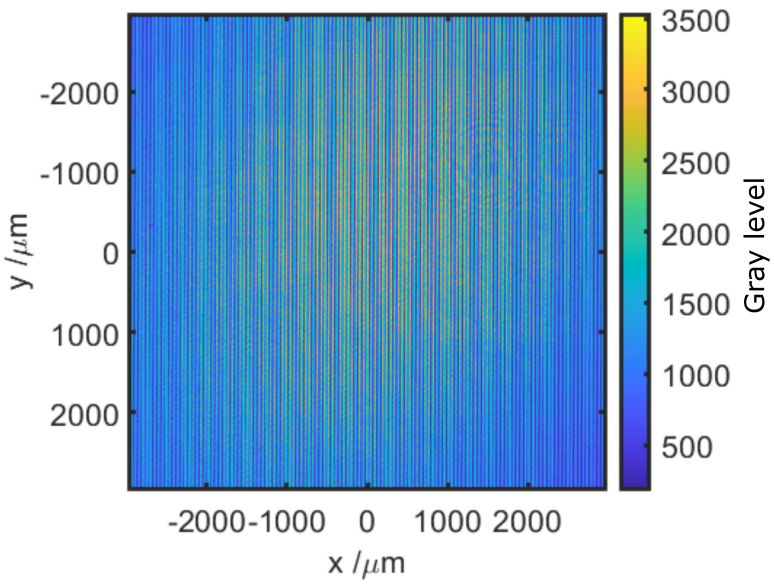

Fig. 5.11 Reference hologram.

Its intensity is the multiplication of the p and s components, and its phase shift equals to the phase difference between them. Fig. 5.12 shows the calculated reflectivity and the phase shift of the reconstructed SPR and reference holograms. According to the Fig. 5.12 (a), the response of the reference hologram (gold-air) may be regarded as constant near the resonant region. So the variations on its reconstruction is caused by the aberration of the systems and the illumination distribution. By dividing the SPR reconstruction with the reference reconstruction, their influence could be removed. The result is illustrated in Fig. 5.13. The dust has a much larger refractive index than air. So at its position, the light being reflected directly, a strong spot could be observed on the intensity reconstruction. The reconstructed phase shift at the corresponding position is around 0.18 rad.

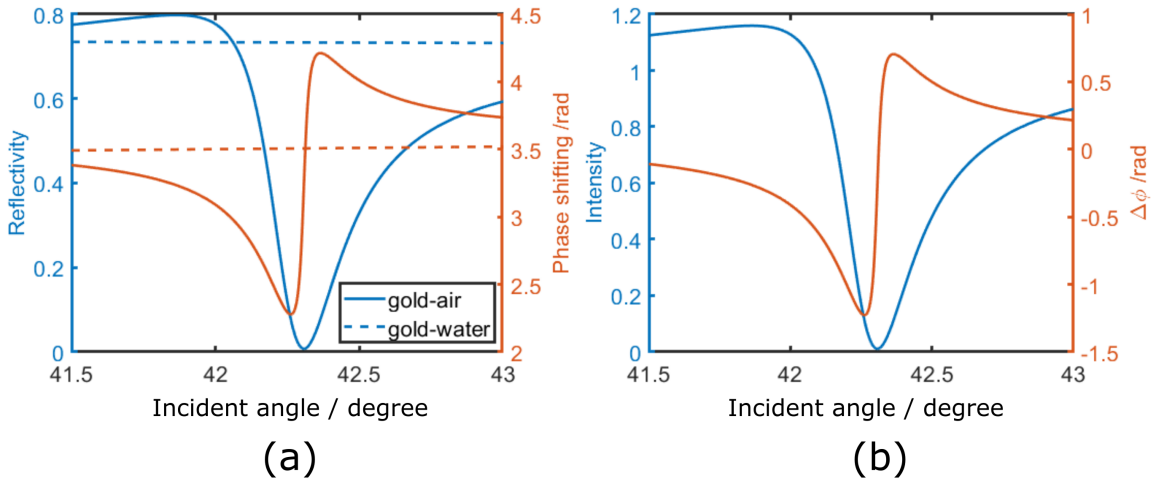

Fig. 5.12 Intensity and phase shift versus incident angle of the reconstructed wave field (a) The solid line are responses of the SPR reconstruction and the dashed lines are those of reference reconstruction. (b) SPR curve normalized by the reference curve.

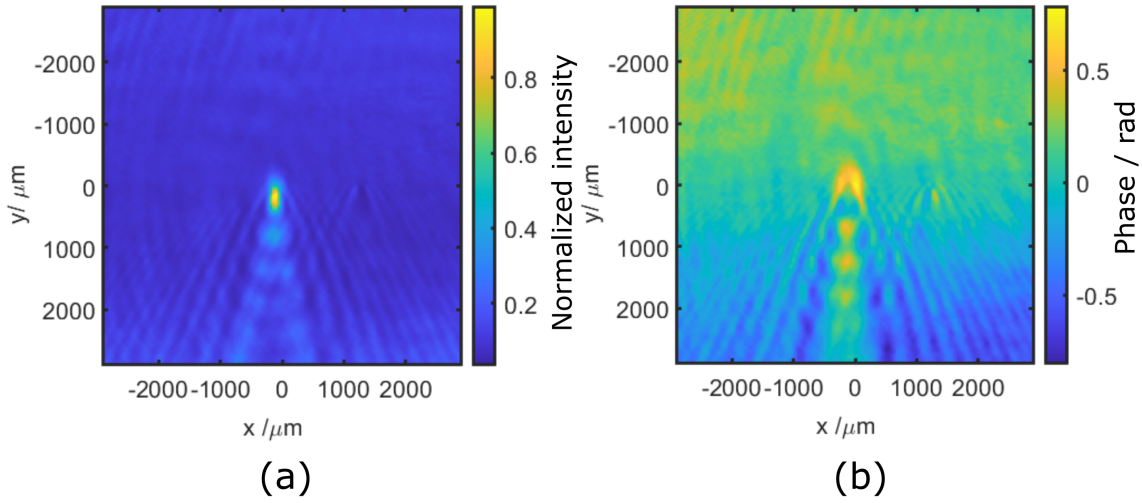

Fig. 5.13 Reconstruction with the system aberration removed and intensity corrected (a) Reconstructed intensity. (b) Reconstructed phase shift.

5.3 SPRDHM imaging of gold-water interface

5.3.1 Intensity response of the gold-water interface

In this section the SPR-DHM imaging of gold-water interface has been achieved. First the resonance position need to be detected as what has been done for the gold-air interface. The intensity is measured first with the gold-air interface (Fig. 5.14(b)). Then a water drop of 2 µL is deposed on top of the gold surface. The intensity is measured again (Fig. 5.14(a)). At the gold-air interface, the incident angle is larger than the critical angle, so the measured intensity may be regarded as total reflection. The reflectivity is then calculated as shown in Fig. 5.14. The minimum reflectivity is measured to be 20 % at 140 µm. It then increases rapidly to

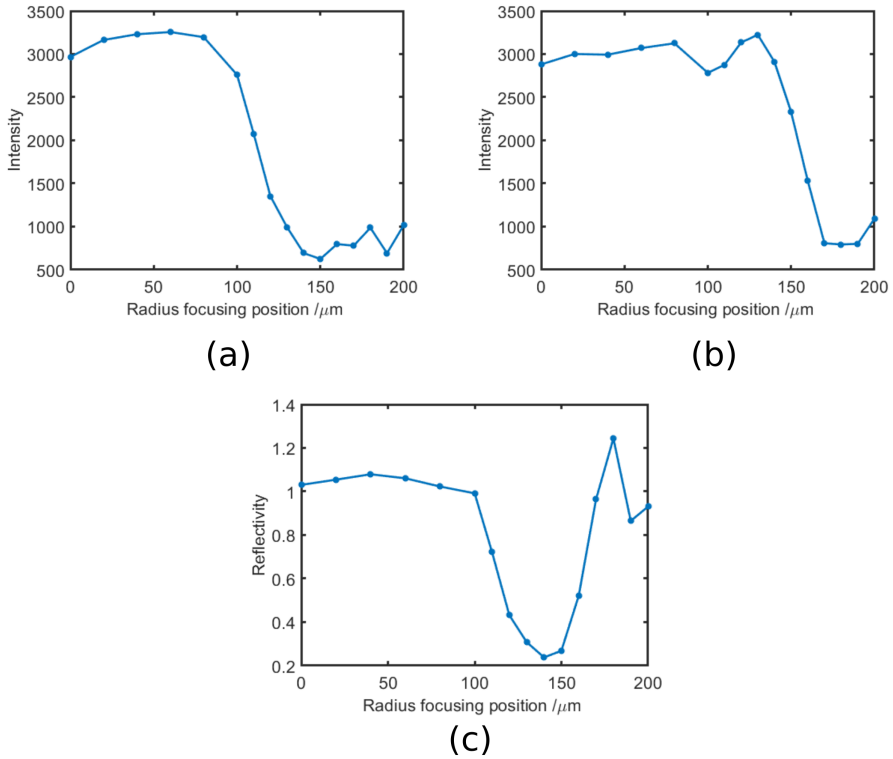

Fig. 5.14 Intensity and reflectivity as functions of the focusing position, 0 µm corresponds to $\rho = 4.0$ mm in experiment. (a) Intensity of the p-polarized light at the gold-water interface. (b) Intensity of the p-polarized light at the gold-air interface. (c) Reflectively by dividing curve (a) with curve (b).

more than 120 %. This abnormal increase is due to the blockage of light by the objective aperture. The stimulation angle of the SPR in gold-water interface is around 65 degrees. It requires the illumination being focused about the edge of the objective aperture. Part of

the illumination may be blocked in this situation. As shown in Fig. 5.14 (b), the intensity reflected from the gold-air interface drops after 140 µm. The intensity is reduced to 27 % after 170 µm. The images at some representative positions are given in the Appendix. A.2 from which the blockage of light is clearly observed.

The image at resonance and its logarithmic spectrum is shown in Fig. 5.15. The resonant angle of the gold-air interface with 850 nm light source is 65 degrees. The corresponding wave number k_x is 1.61 µm^{-1}. The wave number k_{spp} of the SPR locates at the border of the microscope objective aperture on spectrum domain.

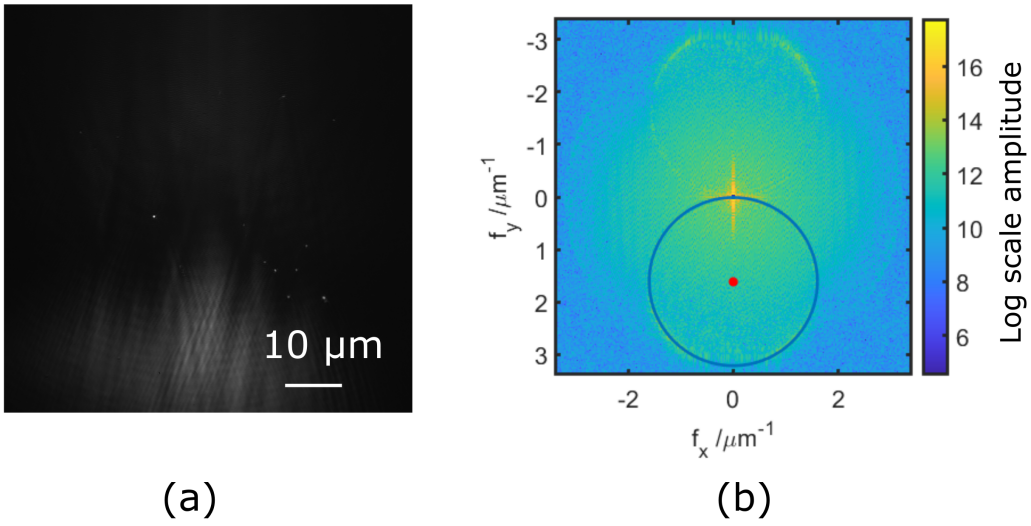

Fig. 5.15 Resonant image of gold-water interface and its logarithmic spectrum. The blue circle corresponds the SPR at gold-water interface. Its center locates at $f_x = 0$, $f_y = 1.61$µm $^{-1}$, and its radius is approximately 1.61 µm^{-1}.

5.3.2 Hologram reconstruction and real time monitoring

The gold-air hologram is reconstructed with the aforementioned method. The gold-water interface hologram is used as the reference for the gold-air interface reconstruction. Similarly, in order to reconstruct the gold-water hologram, the gold-air hologram is used as the reference. The normalized SPR curve of the gold-water interface is drawn in Fig. 5.16.

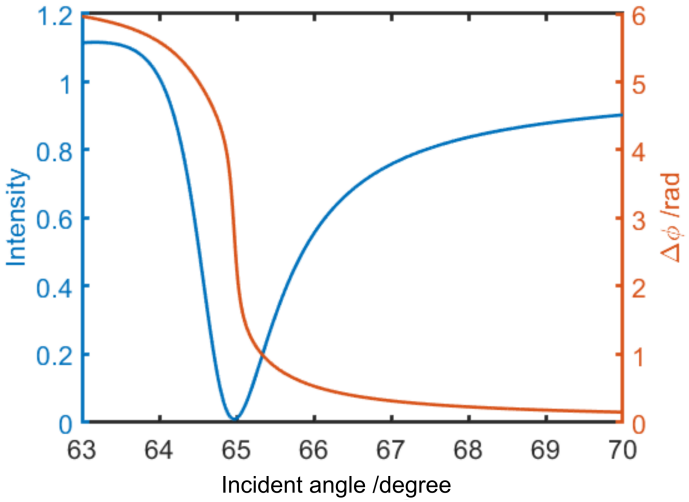

Fig. 5.16 SPR curve of the gold-water interface normalized by the SPR response of the gold-air interface.

The captured gold-water hologram and the reference hologram are show in Fig. 5.17. And the reconstruction result is illustrated in Fig. 5.18. The strong diffraction of the dust appears on both intensity and phase reconstructions. The average reflectivity and phase in the center of image are 29% and 0.89 rad respectively.

The continuous monitoring of the gold-water interface has been proceeded. The holograms are captured for each minute. Fig. 5.19 shows the variations of the reflectivity and phase shift in function of time. 5 µl water is drop at the gold surface and it is totally evaporated after 40 minutes. Consequently, the reflectivity increases to 0.98 and the phase shift decrease to 0.08 rad. Appendix.A.3 shows a real time monitoring of the water-ethanol (5µL water and 1µL ethanol) mixture evaporation. In this experiment, it has been observed that the evaporation time of the mixture is 46 minutes.

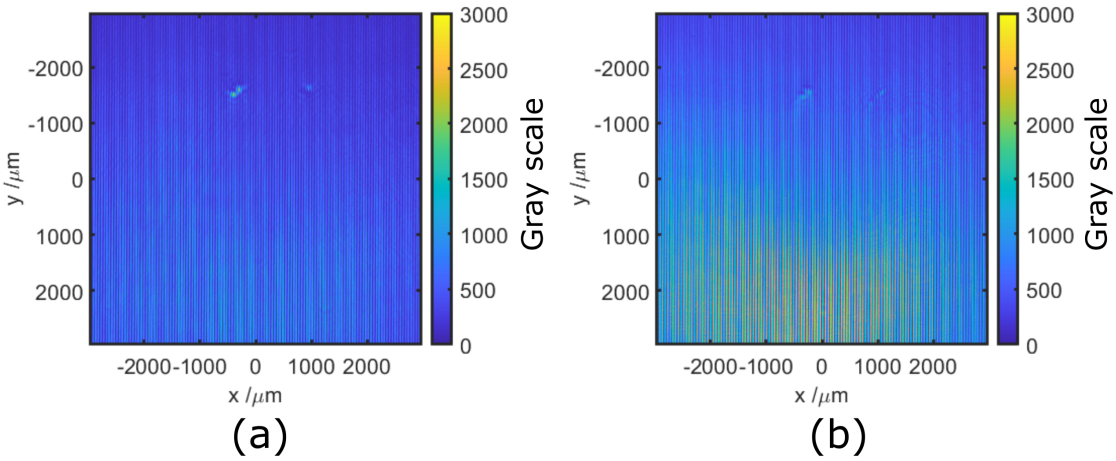

Fig. 5.17 Hologram of gold-water interface and its reference hologram. (a) Hologram of the gold-water interface (b) Reference hologram captured with the gold-air interface

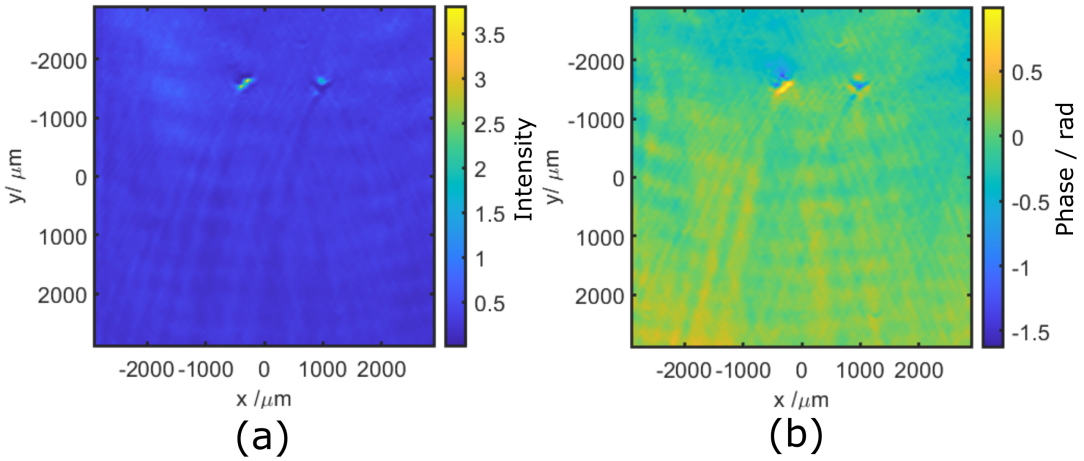

Fig. 5.18 Reconstructed intensity and phase normalized by the reference. (a) Intensity distribution (b) Phase distribution

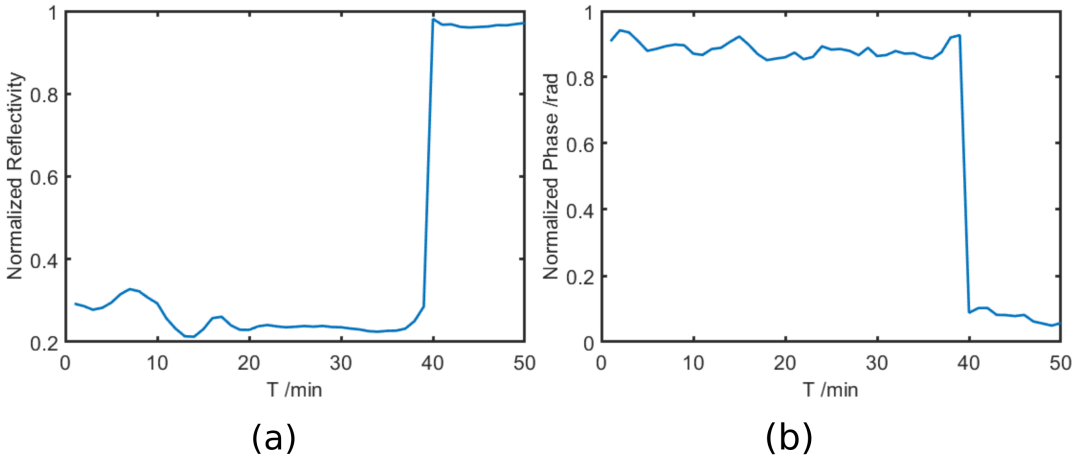

Fig. 5.19 Variation of the reflectivity and phase shift with time. (a) Reflectivity (b) Phase shift

5.4 Conclusion

In this chapter, the near infrared SPR-DHM has been applied to observe the gold-air and gold-water interfaces. It has been tested experimentally that thanks to the near infrared source, the NA 1.42 microscope objective is capable for the SPR holographic imaging the gold-water interface. It has been applied to monitor the evaporation of the a water drop and the water-ethanol mixture. Real time SPR phase imaging has been proved to be possible with our system.

Chapter 6

Conclusion and perspective

6.1 Conclusion

In this thesis, we have presented a near infra-red Surfarce Plasmon Resonance Digital Holographic microscopy (NIR-SPRDHM). It is different from the conventional objective based SPRDHM systems which use special TIRF objectives. We have chosen an 850 nm NIR source that allows the utilization of a cost effective NA 1.42 microscope objective. The system has been designed and built during this PhD work, and then tested on the gold-air and gold-water interfaces. It has been validated as being capable of stimulating and recording the SPR phase responses. This reveals its potential to be applied for biological imaging.

In Chapter 2, we have introduced the physical principle of the SPRM and DHM along with the developments of the SPR phase detection and imaging techniques. Based on the SPR stimulation and Fresnel theories, it has been demonstrated that the NIR source could effectively reduce the stimulation angle of the SPR. It makes the utilization of smaller NA objective possible for gold-water interface which is required for biological imaging. It has been addressed by theoretical analyses that phase responses of the SPR have higher sensitivities than their intensity counter parts. The techniques which could be used for SPR phase imaging are reviewed and compared. Among them the off-axis DHM method has been selected for its capability of real time imaging. The Wollaston prism based common path off-axis holographic setup has been chosen because of its simplicity in structure. Also, with the common path setup, a laser diode which has a limited coherence length can be used. It is more cost effective and may reduce the speckle.

After selection of SPR and DHM methods, the system has been designed and built. In Chapter 3, we have introduced the design of the illumination system, the stimulation and imaging system and the holographic setup. The coherent length, the divergence of the

illumination have been measured experimentally. We have designed and fabricated a spatial filter to remove the unwanted reflection by the beam splitter. From experimental results, we have found that such a filtering could effectively remove the interference noise. As a result, the quality of the hologram image has been improved. In the end, we have solved the aliasing problem due to the small splitting angle of the Wollaston prism. We have replaced the recommended 180 mm lens by a 600 mm image lens. The bandwidth of the image has been reduced to 30% of the original. So the orders of the off-axis hologram could be well separated.

In Chapter 4, we have introduced methods and algorithms that could be used for hologram reconstruction. The algorithms are compared and tested with a homemade in-line lensless DHM setup. The selected algorithms are then used with our SPR-DHM system. We have proved experimentally that our system which has a depth of focus of 3.4 mm, allows manual focusing. Numerical auto-focusing could be avoided

In Chapter 5, our homemade NIR-SPRDHM system has been tested with a coverslip coated with 3 nm of Cr and 45 nm of gold. The hologram images as well as the intensity images have been captured with and without water. We have successfully reconstructed the holograms in both situations. We have then tested the real time phase imaging capability of the SPRDHM by monitoring the evaporation of a water drop. The rapid reflectivity and phase change due to water evaporation have been observed.

6.2 Perspectives

Quantitative assessment of the system

In order to apply the SPR-DHM system for quantitative phase imaging, a sound assessment of the system is necessary. First the noise level needs to be estimated. There are three main sources of noise: variations of the laser source (intensity and phase), influence of the environment (temperature, vibration), and the electric noise of the camera. These noise will influence the accuracy of the measurements.

Then the over all response of the SPR-DHM needs be confronted experimentally including magnification, spatial resolution, phase resolution and the relation between the reconstructed phase and the sample characteristics. In this thesis, the sample is a raw gold surface. Although the SPR diffraction from the dust has been observed, it is difficult to allow quantitative analyse as its geometrical and optical parameters are not known. A sample with a regularized shape and fixed RI is preferable for the assessment. A thin photoresist layer with a designed pattern fabricated by lithography may be used [125].

Application for biological imaging

In Chapter 5, we have proved that our system is capable of stimulating SPR at the gold-water interface and of reconstructing its phase response. This shows its potential for biological imaging as the samples (DNA solution, protein solution *etc.*) are immersed in an aqueous solution. After quantitative calibration of the microscope, it is possible to proceed for quantitative measurements of these samples.

Scanning SPR-DHM

In Sec.2.2.5.3, we have briefly introduced the scanning SPRM. Instead of focusing the illumination at the BFP of the microscope objective, the illumination is collimated and illuminates the whole BFP. The sample information is retrieved based on the crescent shape absorption on the BFP image. Compared to the widefield SPRM, it has a much lower acquisition speed due to the scanning process, and a much higher resolution, because the influence of the SPW propagation can be avoided. Optical heterodyning could be applied to detect the phase response of the scanning SPRM [157]. Optical heterodyning equipments are usually complex and expensive. In contrast, holographic configurations are relatively simple and more cost effective. To the best of our knowledge, the holographic imaging techniques have not been combined with the scanning SPRM. The development of such a novel scanning SPR-DHM may be of wide interest.

References

[1] Robert Williams Wood. Xlii. on a remarkable case of uneven distribution of light in a diffraction grating spectrum. *The London, Edinburgh, and Dublin Philosophical Magazine and Journal of Science*, 4(21):396–402, 1902.

[2] Andreas Otto. Excitation of nonradiative surface plasma waves in silver by the method of frustrated total reflection. *Zeitschrift für Physik A Hadrons and nuclei*, 216(4):398–410, 1968.

[3] Erwin Kretschmann and Heinz Raether. Radiative decay of non radiative surface plasmons excited by light. *Zeitschrift für Naturforschung A*, 23(12):2135–2136, 1968.

[4] Jean-Francois Masson. Surface plasmon resonance clinical biosensors for medical diagnostics. *ACS sensors*, 2(1):16–30, 2017.

[5] Denise Wilson and Brian Ferguson. Optimization of surface plasmon resonance for environmental monitoring. In *SENSORS, 2010 IEEE*, pages 1100–1103. IEEE, 2010.

[6] Saikat Datta Mazumdar, Markus Hartmann, Peter Kämpfer, and Michael Keusgen. Rapid method for detection of salmonella in milk by surface plasmon resonance (spr). *Biosensors and Bioelectronics*, 22(9-10):2040–2046, 2007.

[7] Benno Rothenhäusler and Wolfgang Knoll. Surface–plasmon microscopy. *Nature*, 332(6165):615–617, 1988.

[8] Bo Huang, Fang Yu, and Richard N Zare. Surface plasmon resonance imaging using a high numerical aperture microscope objective. *Analytical chemistry*, 79(7):2979–2983, 2007.

[9] B Mandracchia, V Pagliarulo, M Paturzo, and P Ferraro. Surface plasmon resonance imaging by holographic enhanced mapping. *Analytical chemistry*, 87(8):4124–4128, 2015.

[10] Jiwei Zhang, Siqing Dai, Chaojie Ma, Jianglei Di, and Jianlin Zhao. Compact surface plasmon holographic microscopy for near-field film mapping. *Optics letters*, 42(17):3462–3465, 2017.

[11] Siqing Dai, Tongyao Yu, Jiwei Zhang, Hua Lu, Jiazhen Dou, Mengmeng Zhang, Chen Dong, Jianglei Di, and Jianlin Zhao. Real-time and wide-field mapping of cell-substrate adhesion gap and its evolution via surface plasmon resonance holographic microscopy. *Biosensors and Bioelectronics*, 174:112826, 2021.

[12] Dennis Gabor. A new microscopic principle. *nature*, 161:777–778, 1948.

[13] Ulf Schnars and Werner PO Jüptner. Digital recording and numerical reconstruction of holograms. *Measurement science and technology*, 13(9):R85, 2002.

[14] Dennis Gabor. Microscopy by reconstructed wave-fronts. *Proceedings of the Royal Society of London. Series A. Mathematical and Physical Sciences*, 197(1051):454–487, 1949.

[15] Dennis Gabor. Microscopy by reconstructed wave fronts:. *Proceedings of the Physical Society. Section B*, 64(6):449, 1951.

[16] Emmett N Leith and Juris Upatnieks. Reconstructed wavefronts and communication theory. *JOSA*, 52(10):1123–1130, 1962.

[17] Sean F Johnston. A cultural history of the hologram. *Leonardo*, 41(3):223–229, 2008.

[18] The nobel prize in physics 1971. https://www.nobelprize.org/prizes/physics/1971/summary, 2021.

[19] Joseph W. Goodman. *Introduction to fourier optics*. Roberts & amp; Company, 2005.

[20] Junchang LI and Yanmei Wu. *Diffraction Calculation and Digital Holography.* Science Press, 2016.

[21] Erich W Marchand and Emil Wolf. Consistent formulation of kirchhoff's diffraction theory. *JOSA*, 56(12):1712–1721, 1966.

[22] John C Heurtley. Scalar rayleigh–sommerfeld and kirchhoff diffraction integrals: a comparison of exact evaluations for axial points. *JOSA*, 63(8):1003–1008, 1973.

[23] M Totzeck. Validity of the scalar kirchhoff and rayleigh–sommerfeld diffraction theories in the near field of small phase objects. *JOSA A*, 8(1):27–32, 1991.

[24] Juha Saatsi and Peter Vickers. Miraculous success? inconsistency and untruth in kirchhoff's diffraction theory. *The British Journal for the Philosophy of Science*, 62(1):29–46, 2011.

[25] George C Sherman. Application of the convolution theorem to rayleigh's integral formulas. *JOSA*, 57(4):546–547, 1967.

[26] Jonathan Maycock, Bryan M Hennelly, John B McDonald, Yann Frauel, Albertina Castro, Bahram Javidi, and Thomas J Naughton. Reduction of speckle in digital holography by discrete fourier filtering. *JOSA A*, 24(6):1617–1622, 2007.

[27] Vicente Micó and Zeev Zalevsky. Superresolved digital in-line holographic microscopy for high-resolution lensless biological imaging. *Journal of biomedical optics*, 15(4):046027, 2010.

[28] Jialin Zhang, Jiasong Sun, Qian Chen, Jiaji Li, and Chao Zuo. Adaptive pixel-super-resolved lensfree in-line digital holography for wide-field on-chip microscopy. *Scientific reports*, 7(1):1–15, 2017.

[29] Vittorio Bianco, Pasquale Memmolo, Marco Leo, Silvio Montresor, Cosimo Distante, Melania Paturzo, Pascal Picart, Bahram Javidi, and Pietro Ferraro. Strategies for reducing speckle noise in digital holography. *Light: Science & Applications*, 7(1):1–16, 2018.

[30] Yair Rivenson, Yichen Wu, and Aydogan Ozcan. Deep learning in holography and coherent imaging. *Light: Science & Applications*, 8(1):1–8, 2019.

[31] KA Nugent. Twin-image elimination in gabor holography. *Optics communications*, 78(3-4):293–299, 1990.

[32] CP Grover. Multiple-exposure in-line holography of object transparencies with binary tone. *Applied optics*, 12(1):149–150, 1973.

[33] JJ Barton. Removing multiple scattering and twin images from holographic images. *Physical review letters*, 67(22):3106, 1991.

[34] Loic Denis, Corinne Fournier, Thierry Fournel, and Christophe Ducottet. Twin-image noise reduction by phase retrieval in in-line digital holography. In *Wavelets XI*, volume 5914, page 59140J. International Society for Optics and Photonics, 2005.

[35] Tatiana Latychevskaia and Hans-Werner Fink. Solution to the twin image problem in holography. *Physical review letters*, 98(23):233901, 2007.

[36] Corinne Fournier, Loic Denis, Eric Thiebaut, Thierry Fournel, and Mozhdeh Seifi. Inverse problem approaches for digital hologram reconstruction. In *Three-Dimensional Imaging, Visualization, and Display 2011*, volume 8043, page 80430S. International Society for Optics and Photonics, 2011.

[37] Weijuan Qu, Oi Choo Chee, Yingjie Yu, and Anand Asundi. Recording and reconstruction of digital gabor hologram. *Optik*, 121(23):2179–2184, 2010.

[38] Hongyu Li, Anastasia Bozhok, Yoshitate Takakura, Jean Dellinger, Patrice Twardowski, and Jihad Zallat. Lensless inline digital holography versus fourier ptychography: phase estimation of a large transparent bead. *Optical Engineering*, 59(8):083104, 2020.

[39] Yair Rivenson, Yibo Zhang, Harun Günaydın, Da Teng, and Aydogan Ozcan. Phase recovery and holographic image reconstruction using deep learning in neural networks. *Light: Science & Applications*, 7(2):17141–17141, 2018.

[40] Zhenbo Ren, Zhimin Xu, and Edmund YM Lam. End-to-end deep learning framework for digital holographic reconstruction. *Advanced Photonics*, 1(1):016004, 2019.

[41] Yichen Wu, Yilin Luo, Gunvant Chaudhari, Yair Rivenson, Ayfer Calis, Kevin De Haan, and Aydogan Ozcan. Bright-field holography: cross-modality deep learning enables snapshot 3d imaging with bright-field contrast using a single hologram. *Light: Science & Applications*, 8(1):1–7, 2019.

[42] G Tricoles and Nabil H Farhat. Microwave holography-applications and techniques. In *IEEE Proceedings*, volume 65, pages 108–121, 1977.

[43] Christoph T Koch. Towards full-resolution inline electron holography. *Micron*, 63:69–75, 2014.

[44] Lu Rong, Tatiana Latychevskaia, Chunhai Chen, Dayong Wang, Zhengping Yu, Xun Zhou, Zeyu Li, Haochong Huang, Yunxin Wang, and Zhou Zhou. Terahertz in-line digital holography of human hepatocellular carcinoma tissue. *Scientific reports*, 5(1):1–6, 2015.

[45] Hongyue Sun, Philip William Benzie, N Burns, David C Hendry, Michael Antony Player, and John Watson. Underwater digital holography for studies of marine plankton. *Philosophical Transactions of the Royal Society A: Mathematical, Physical and Engineering Sciences*, 366(1871):1789–1806, 2008.

[46] Yichen Wu and Aydogan Ozcan. Lensless digital holographic microscopy and its applications in biomedicine and environmental monitoring. *Methods*, 136:4–16, 2018.

[47] Ting-Wei Su, Serhan O Isikman, Waheb Bishara, Derek Tseng, Anthony Erlinger, and Aydogan Ozcan. Multi-angle lensless digital holography for depth resolved imaging on a chip. *Optics express*, 18(9):9690–9711, 2010.

[48] Wenbo Xu, MH Jericho, IA Meinertzhagen, and HJ Kreuzer. Digital in-line holography for biological applications. *Proceedings of the National Academy of Sciences*, 98(20):11301–11305, 2001.

[49] Emmett N Leith and Juris Upatnieks. Wavefront reconstruction with continuous-tone objects. *JOSA*, 53(12):1377–1381, 1963.

[50] Emmett N Leith and Juris Upatnieks. Wavefront reconstruction with diffused illumination and three-dimensional objects. *Josa*, 54(11):1295–1301, 1964.

[51] Yves Emery, Tristan Colomb, and Etienne Cuche. Metrology applications using off-axis digital holography microscopy. *Journal of Physics: Photonics*, 2021.

[52] Tatsuki Tahara, Xiangyu Quan, Reo Otani, Yasuhiro Takaki, and Osamu Matoba. Digital holography and its multidimensional imaging applications: a review. *Microscopy*, 67(2):55–67, 2018.

[53] Gili Dardikman and Natan T Shaked. Is multiplexed off-axis holography for quantitative phase imaging more spatial bandwidth-efficient than on-axis holography? *JOSA A*, 36(2):A1–A11, 2019.

[54] Björn Kemper and Gert Von Bally. Digital holographic microscopy for live cell applications and technical inspection. *Applied optics*, 47(4):A52–A61, 2008.

[55] Nazif Demoli, Dalibor Vukicevic, and Marc Torzynski. Dynamic digital holographic interferometry with three wavelengths. *Optics Express*, 11(7):767–774, 2003.

[56] Markus Fratz, Tobias Seyler, Alexander Bertz, and Daniel Carl. Digital holography in production: an overview. *Light: Advanced Manufacturing*, 2(2):134–146, 2021.

[57] Gabriel Popescu, Takahiro Ikeda, Ramachandra R Dasari, and Michael S Feld. Diffraction phase microscopy for quantifying cell structure and dynamics. *Optics letters*, 31(6):775–777, 2006.

[58] Amardeep SG Singh, Arun Anand, Rainer A Leitgeb, and Bahram Javidi. Lateral shearing digital holographic imaging of small biological specimens. *Optics express*, 20(21):23617–23622, 2012.

[59] KyeoReh Lee and YongKeun Park. Quantitative phase imaging unit. *Optics letters*, 39(12):3630–3633, 2014.

[60] Chaojie Ma, Ying Li, Jiwei Zhang, Peng Li, Teli Xi, Jianglei Di, and Jianlin Zhao. Lateral shearing common-path digital holographic microscopy based on a slightly trapezoid sagnac interferometer. *Optics express*, 25(12):13659–13667, 2017.

[61] Arne Bokemeyer, Phil Robin Tepasse, Lena Quill, Philipp Lenz, Emile Rijcken, Michael Vieth, Nik Ding, Steffi Ketelhut, Florian Rieder, Björn Kemper, et al. Quantitative phase imaging using digital holographic microscopy reliably assesses morphology and reflects elastic properties of fibrotic intestinal tissue. *Scientific reports*, 9(1):1–11, 2019.

[62] Jonas Kühn, Bimochan Niraula, Kurt Liewer, J Kent Wallace, Eugene Serabyn, Emilio Graff, Christian Lindensmith, and Jay L Nadeau. A mach-zender digital holographic microscope with sub-micrometer resolution for imaging and tracking of marine microorganisms. *Review of Scientific Instruments*, 85(12):123113, 2014.

[63] Frédéric Verpillat, Fadwa Joud, Pierre Desbiolles, and Michel Gross. Dark-field digital holographic microscopy for 3d-tracking of gold nanoparticles. *Optics express*, 19(27):26044–26055, 2011.

[64] Xiao Yu, Jisoo Hong, Changgeng Liu, and Myung K Kim. Review of digital holographic microscopy for three-dimensional profiling and tracking. *Optical engineering*, 53(11):112306, 2014.

[65] Heikki Rekola, Alex Berdin, Chiara Fedele, Matti Virkki, and Arri Priimagi. Digital holographic microscopy for real-time observation of surface-relief grating formation on azobenzene-containing films. *Scientific reports*, 10(1):1–10, 2020.

[66] Monica Hellesvik, Hanne Øye, and Henriette Aksnes. Exploiting the potential of commercial digital holographic microscopy by combining it with 3d matrix cell culture assays. *Scientific reports*, 10(1):1–14, 2020.

[67] James P Ryle, John T Sheridan, and Susan McDonnell. Lensless multispectral digital in-line holographic microscope. *Journal of biomedical optics*, 16(12):126004, 2011.

[68] Vicente Micó, Zeev Zalevsky, Carlos Ferreira, and Javier García. Superresolution digital holographic microscopy for three-dimensional samples. *Optics express*, 16(23):19260–19270, 2008.

[69] Ugo Fano. The theory of anomalous diffraction gratings and of quasi-stationary waves on metallic surfaces (sommerfeld's waves). *JOSA*, 31(3):213–222, 1941.

[70] David Pines. Collective energy losses in solids. *Reviews of modern physics*, 28(3):184, 1956.

[71] Rufus H Ritchie. Plasma losses by fast electrons in thin films. *Physical review*, 106(5):874, 1957.

[72] EA Stern and RA Ferrell. Surface plasma oscillations of a degenerate electron gas. *Physical Review*, 120(1):130, 1960.

[73] RH Ritchie. On surface plasma oscillations in metal foils. *Progr. Theoret. Phys.(Kyoto)*, 29, 1963.

[74] T Turbadar. Complete absorption of light by thin metal films. *Proceedings of the Physical Society (1958-1967)*, 73(1):40, 1959.

[75] Masahiro Yamamoto. Surface plasmon resonance (spr) theory: tutorial. *Review of Polarography*, 48(3):209–237, 2002.

[76] P.B. Johnson and R.W. Christy. Optical constants of the noble metals. *Physical review B*, 6(12):4370, 1972.

[77] Masahiko Daimon and Akira Masumura. Measurement of the refractive index of distilled water from the near-infrared region to the ultraviolet region. *Applied optics*, 46(18):3811–3820, 2007.

[78] Jiri Homola. *Surface plasmon resonance based sensors*, volume 4. Springer Science & Business Media, 2006.

[79] Linda S Jung, Charles T Campbell, Timothy M Chinowsky, Mimi N Mar, and Sinclair S Yee. Quantitative interpretation of the response of surface plasmon resonance sensors to adsorbed films. *Langmuir*, 14(19):5636–5648, 1998.

[80] Ralph C Jorgenson and Sinclair S Yee. A fiber-optic chemical sensor based on surface plasmon resonance. *Sensors and Actuators B: Chemical*, 12(3):213–220, 1993.

[81] D.C. Cullen, R.G.W. Brown, and C.R. Lowe. Detection of immuno-complex formation via surface plasmon resonance on gold-coated diffraction gratings. *Biosensors*, 3(4):211–225, 1987.

[82] Anastasiya Derkachova, Krystyna Kolwas, and Iraida Demchenko. Dielectric function for gold in plasmonics applications: size dependence of plasmon resonance frequencies and damping rates for nanospheres. *Plasmonics*, 11(3):941–951, 2016.

[83] Wilford N Hansen. Electric fields produced by the propagation of plane coherent electromagnetic radiation in a stratified medium. *JOSA*, 58(3):380–390, 1968.

[84] Jiri Homola, Sinclair S Yee, and Günter Gauglitz. Surface plasmon resonance sensors. *Sensors and actuators B: Chemical*, 54(1-2):3–15, 1999.

[85] Pranveer Singh. Spr biosensors: historical perspectives and current challenges. *Sensors and actuators B: Chemical*, 229:110–130, 2016.

[86] Bo Liedberg, Claes Nylander, and Ingemar Lunström. Surface plasmon resonance for gas detection and biosensing. *Sensors and actuators*, 4:299–304, 1983.

[87] Stefano Mariani and Maria Minunni. Surface plasmon resonance applications in clinical analysis. *Analytical and bioanalytical chemistry*, 406(9):2303–2323, 2014.

[88] Peng Zhang, You-Peng Chen, Wei Wang, Yu Shen, and Jin-Song Guo. Surface plasmon resonance for water pollutant detection and water process analysis. *TrAC Trends in Analytical Chemistry*, 85:153–165, 2016.

[89] Jinru Zhou, Qinqin Qi, Chong Wang, Yifan Qian, Guangming Liu, Yanbo Wang, and Linglin Fu. Surface plasmon resonance (spr) biosensors for food allergen detection in food matrices. *Biosensors and Bioelectronics*, 142:111449, 2019.

[90] Web of Science. Citation report of publications related to surface plasmon resonance (spr) from 1990 to 2020, 2021. https://www.webofscience.com/wos/woscc/citation-report/0000e19e-1a7c-499a-a608-d041ebacb7ca-108e7b38, https://www.webofscience.com/wos/woscc/citation-report/7022c199-442e-4739-aab1-a5cf12c6742a-108eb19c.

[91] Christelle Corne, Jean-Bernard Fiche, Didier Gasparutto, Valérie Cunin, Emmanuel Suraniti, Arnaud Buhot, Julia Fuchs, Roberto Calemczuk, Thierry Livache, and Alain Favier. Spr imaging for label-free multiplexed analyses of dna n-glycosylase interactions with damaged dna duplexes. *Analyst*, 133(8):1036–1045, 2008.

[92] Alexander W Peterson, Michael Halter, Alessandro Tona, Kiran Bhadriraju, and Anne L Plant. Surface plasmon resonance imaging of cells and surface-associated fibronectin. *BMC cell biology*, 10(1):1–17, 2009.

[93] Graham Stabler, Michael Geoffrey Somekh, and CW See. High-resolution wide-field surface plasmon microscopy. *Journal of Microscopy*, 214(3):328–333, 2004.

[94] Alexander W Peterson, Michael Halter, Alessandro Tona, Kiran Bhadriraju, John T Elliott, and Anne L Plant. High resolution surface plasmon resonance imaging of focal adhesions in single cells. *Biophysical Journal*, 106(2):24a–25a, 2014.

[95] Alexander W Peterson, Michael Halter, Anne L Plant, and John T Elliott. Surface plasmon resonance microscopy: Achieving a quantitative optical response. *Review of Scientific Instruments*, 87(9):093703, 2016.

[96] Han-Min Tan, Suejit Pechprasarn, Jing Zhang, Mark C Pitter, and Michael G Somekh. High resolution quantitative angle-scanning widefield surface plasmon microscopy. *Scientific reports*, 6(1):1–11, 2016.

[97] Sorawit Tontarawongsa, Sarinporn Visitsattapongse, and Suejit Pechprasarn. Performance analysis of non-interferometry based surface plasmon resonance microscopes. *Sensors*, 21(15):5230, 2021.

[98] Hiroshi Kano, Seiji Mizuguchi, and Satoshi Kawata. Excitation of surface-plasmon polaritons by a focused laser beam. *JOSA B*, 15(4):1381–1386, 1998.

[99] Hiroshi Kano and Wolfgang Knoll. A scanning microscope employing localized surface-plasmon-polaritons as a sensing probe. *Optics Communications*, 182(1-3):11–15, 2000.

[100] Kouyou Watanabe, Nobuhiro Horiguchi, and Hiroshi Kano. Optimized measurement probe of the localized surface plasmon microscope by using radially polarized illumination. *Applied optics*, 46(22):4985–4990, 2007.

[101] KJ Moh, X-C Yuan, J Bu, SW Zhu, and Bruce Z Gao. Surface plasmon resonance imaging of cell-substrate contacts with radially polarized beams. *Optics express*, 16(25):20734–20741, 2008.

[102] Andrei V Kabashin, Sergiy Patskovsky, and Alexander N Grigorenko. Phase and amplitude sensitivities in surface plasmon resonance bio and chemical sensing. *Optics Express*, 17(23):21191–21204, 2009.

[103] Dongping Wang, Jacky Fong Chuen Loo, Jiajie Chen, Yeung Yam, Shih-Chi Chen, Hao He, Siu Kai Kong, and Ho Pui Ho. Recent advances in surface plasmon resonance imaging sensors. *Sensors*, 19(6):1266, 2019.

[104] F Abeles. Surface electromagnetic waves ellipsometry. *Surface Science*, 56:237–251, 1976.

[105] YH Huang, HP Ho, SY Wu, and SK Kong. Detecting phase shifts in surface plasmon resonance: a review. *Advances in Optical Technologies*, 2012, 2012.

[106] Youjun Zeng, Rui Hu, Lei Wang, Dayong Gu, Jianan He, Shu-Yuen Wu, Ho-Pui Ho, Xuejin Li, Junle Qu, Bruce Zhi Gao, et al. Recent advances in surface plasmon resonance imaging: detection speed, sensitivity, and portability. *Nanophotonics*, 6(5):1017–1030, 2017.

[107] Ian R Hooper and J Roy Sambles. Sensing using differential surface plasmon ellipsometry. *Journal of Applied Physics*, 96(5):3004–3011, 2004.

[108] Ian R Hooper and J Roy Sambles. Differential ellipsometric surface plasmon resonance sensors with liquid crystal polarization modulators. *Applied physics letters*, 85(15):3017–3019, 2004.

[109] HP Ho, Wing Cheung Law, SY Wu, XH Liu, SP Wong, Chinlon Lin, and SK Kong. Phase-sensitive surface plasmon resonance biosensor using the photoelastic modulation technique. *Sensors and Actuators B: Chemical*, 114(1):80–84, 2006.

[110] SG Nelson, Kyle S Johnston, and Sinclair S Yee. High sensitivity surface plasmon resonace sensor based on phase detection. *Sensors and actuators B: Chemical*, 35(1-3):187–191, 1996.

[111] Yu Xinglong, Zhao Lequn, Jiang Hong, Wang Haojuan, Yin Chunyong, and Zhu Shenggeng. Immunosensor based on optical heterodyne phase detection. *Sensors and Actuators B: Chemical*, 76(1-3):199–202, 2001.

[112] HP Ho, WW Lam, and SY Wu. Surface plasmon resonance sensor based on the measurement of differential phase. *Review of Scientific Instruments*, 73(10):3534–3539, 2002.

[113] Shean-Jen Chen, Yuan-Deng Su, Feng-Ming Hsiu, Chia-Yuan Tsou, and Yi-Kuang Chen. Surface plasmon resonance phase-shift interferometry: real-time dna microarray hybridization analysis. *Journal of Biomedical Optics*, 10(3):034005, 2005.

[114] CL Wong, HP Ho, TT Yu, YK Suen, Winnie WY Chow, SY Wu, Wing Cheung Law, W Yuan, WJ Li, SK Kong, et al. Two-dimensional biosensor arrays based on surface plasmon resonance phase imaging. *Applied optics*, 46(12):2325–2332, 2007.

[115] Cuiying Hu, Jingang Zhong, and Jiawen Weng. Digital holographic microscopy by use of surface plasmon resonance for imaging of cell membranes. *Journal of biomedical optics*, 15(5):056015, 2010.

[116] Andrei Viktorovich Kabashin and Petr Ivanovich Nikitin. Interferometer based on a surface-plasmon resonance for sensor applications. *Quantum Electronics*, 27(7):653, 1997.

[117] AV Kabashin and PI Nikitin. Surface plasmon resonance interferometer for bio-and chemical-sensors. *Optics communications*, 150(1-6):5–8, 1998.

[118] AN Grigorenko, PI Nikitin, and AV Kabashin. Phase jumps and interferometric surface plasmon resonance imaging. *Applied Physics Letters*, 75(25):3917–3919, 1999.

[119] Ariel G Notcovich, V Zhuk, and SG Lipson. Surface plasmon resonance phase imaging. *Applied Physics Letters*, 76(13):1665–1667, 2000.

[120] Shiping Li and Jingang Zhong. Simultaneous amplitude-contrast and phase-contrast surface plasmon resonance imaging by use of digital holography. *Biomedical optics express*, 3(12):3190–3202, 2012.

[121] PI Nikitin, AA Beloglazov, VE Kochergin, MV Valeiko, and TI Ksenevich. Surface plasmon resonance interferometry for biological and chemical sensing. *Sensors and Actuators B: Chemical*, 54(1-2):43–50, 1999.

[122] Jiwei Zhang, Siqing Dai, Chaojie Ma, Jianglei Di, and Jianlin Zhao. Common-path digital holographic microscopy for near-field phase imaging based on surface plasmon resonance. *Applied optics*, 56(11):3223–3228, 2017.

[123] Jiwei Zhang, Siqing Dai, Jinzhan Zhong, Teli Xi, Chaojie Ma, Ying Li, Jianglei Di, and Jianlin Zhao. Wavelength-multiplexing surface plasmon holographic microscopy. *Optics express*, 26(10):13549–13560, 2018.

[124] Siqing Dai, Hua Lu, Jiwei Zhang, Yuping Shi, Jiazhen Dou, Jianglei Di, and Jianlin Zhao. Complex refractive index measurement for atomic-layer materials via surface plasmon resonance holographic microscopy. *Optics letters*, 44(12):2982–2985, 2019.

[125] Jiazhen Dou, Siqing Dai, Chen Dong, Jiwei Zhang, Jianglei Di, and Jianlin Zhao. Dual-channel illumination surface plasmon resonance holographic microscopy for resolution improvement. *Optics Letters*, 46(7):1604–1607, 2021.

[126] Aaron R Halpern, Jennifer B Wood, Yong Wang, and Robert M Corn. Single-nanoparticle near-infrared surface plasmon resonance microscopy for real-time measurements of dna hybridization adsorption. *ACS nano*, 8(1):1022–1030, 2014.

[127] Ryan M Spies, Grace H Cole, Marit A Engevik, Britta G Nordberg, Evan A Scharnick, Isaac M Vliem, Alexandre G Brolo, and Nathan C Lindquist. Digital plasmonic holography with iterative phase retrieval for sensing. *Optics Express*, 29(3):3026–3037, 2021.

[128] Max Born and Emil Wolf. *Principles of optics: electromagnetic theory of propagation, interference and diffraction of light*. Elsevier, 2013.

[129] Rajiv Dubey and Raj Kumar. A simple setup for measurement of the coherence length of a laser diode using holographic optics. *European Journal of Physics*, 40(5):055304, 2019.

[130] Amrita Mazumdar. Principles and techniques of schlieren imaging systems. 2013.

[131] Shaopeng Wang, Xiaonan Shan, Urmez Patel, Xinping Huang, Jin Lu, Jinghong Li, and Nongjian Tao. Label-free imaging, detection, and mass measurement of single viruses by surface plasmon resonance. *Proceedings of the National Academy of Sciences*, 107(37):16028–16032, 2010.

[132] Fucai Zhang, Ichirou Yamaguchi, and LP Yaroslavsky. Algorithm for reconstruction of digital holograms with adjustable magnification. *Optics letters*, 29(14):1668–1670, 2004.

[133] Kyoji Matsushima and Tomoyoshi Shimobaba. Band-limited angular spectrum method for numerical simulation of free-space propagation in far and near fields. *Optics express*, 17(22):19662–19673, 2009.

[134] Hazar A. Ilhan, Mert Doğar, and Meriç Özcan. Fast autofocusing in digital holography using scaled holograms. *Optics Communications*, 287:81–84, 2013.

[135] Elsa S. R. Fonseca, Paulo T. Fiadeiro, Manuela Pereira, and António Pinheiro. Comparative analysis of autofocus functions in digital in-line phase-shifting holography. *Applied Optics*, 55(27):7663, 2016.

[136] Zhenbo Ren, Zhimin Xu, and Edmund Y. Lam. Learning-based nonparametric autofocusing for digital holography. *Optica*, 5(4):337, 2018.

[137] Patrik Langehanenberg, Björn Kemper, Dieter Dirksen, and Gert von Bally. Autofocusing in digital holographic phase contrast microscopy on pure phase objects for live cell imaging. *Applied Optics*, 47(19):D176, 2008.

[138] Patrik Langehanenberg, Gert von Bally, and Björn Kemper. Autofocusing in digital holographic microscopy. *3D Research*, 2(1):1–11, 2011.

[139] Yibo Zhang, Hongda Wang, Yichen Wu, Miu Tamamitsu, and Aydogan Ozcan. Edge sparsity criterion for robust holographic autofocusing. *Optics Letters*, 42(19):3824, 2017.

[140] Lawrence Firestone, Kitty Cook, Kevin Culp, Neil Talsania, and Kendall Preston. Comparison of autofocus methods for automated microscopy. *Cytometry*, 12(3):195–206, 1991.

[141] D. Vollath. Automatic focusing by correlative methods. *Journal of Microscopy*, 147(3):279–288, 1987.

[142] Frank Dubois, Cédric Schockaert, Natcaha Callens, and Catherine Yourassowsky. Focus plane detection criteria in digital holography microscopy by amplitude analysis. *Optics Express*, 14(13):5895, 2006.

[143] Weichang Li, Nick C Loomis, Qiao Hu, and Cabell S Davis. Focus detection from digital in-line holograms based on spectral l 1 norms. *JOSA A*, 24(10):3054–3062, 2007.

[144] Carlos Trujillo and Jorge Garcia-Sucerquia. Comparative analysis of the modified enclosed energy metric for self-focusing holograms from digital lensless holographic microscopy. *Applied Optics*, 54(16):5102, 2015.

[145] Michael Liebling and Michael Unser. Autofocus for digital Fresnel holograms by use of a Fresnelet-sparsity criterion. *Journal of the Optical Society of America A*, 21(12):2424, 2004.

[146] P. Memmolo, C. Distante, M. Paturzo, A. Finizio, P. Ferraro, and B. Javidi. Automatic focusing in digital holography and its application to stretched holograms. *Optics Letters*, 36(10):1945, 2011.

[147] Pasquale Memmolo, Melania Paturzo, Bahram Javidi, Paolo A. Netti, and Pietro Ferraro. Refocusing criterion via sparsity measurements in digital holography. *Optics Letters*, 39(16):4719, 2014.

[148] M. Tamamitsu, Y. Zhang, H. Wang, Y. Wu, and A. Ozcan. A robust holographic autofocusing criterion based on edge sparsity: Comparison of Gini index and Tamura coefficient for holographic autofocusing based on the edge sparsity of the complex optical wavefront. *Progress in Biomedical Optics and Imaging - Proceedings of SPIE*, 10503:1–9, 2018.

[149] Karen M Molony, Bryan M Hennelly, Damien P Kelly, and Thomas J Naughton. Reconstruction algorithms applied to in-line gabor digital holographic microscopy. *Optics Communications*, 283(6):903–909, 2010.

[150] Michael J Best. *Quadratic programming with computer programs*. CRC Press, 2017.

[151] Miguel Arevallilo Herráez, David R Burton, Michael J Lalor, and Munther A Gdeisat. Fast two-dimensional phase-unwrapping algorithm based on sorting by reliability following a noncontinuous path. *Applied optics*, 41(35):7437–7444, 2002.

[152] Dennis C Ghiglia and Louis A Romero. Robust two-dimensional weighted and unweighted phase unwrapping that uses fast transforms and iterative methods. *JOSA A*, 11(1):107–117, 1994.

[153] Michael Mullen. 2d and 3d phase unwrapping using srncp, 2021. https://github.com/mfmullen/PhaseUnwrapping/releases/tag/v3.0.2.

[154] Luru Dai, Ingo Gregor, Iris von der Hocht, Thomas Ruckstuhl, and Jörg Enderlein. Measuring large numerical apertures by imaging the angular distribution of radiation of fluorescing molecules. *Optics express*, 13(23):9409–9414, 2005.

[155] Hui Yu, Xiaonan Shan, Shaopeng Wang, and Nongjian Tao. Achieving high spatial resolution surface plasmon resonance microscopy with image reconstruction. *Analytical chemistry*, 89(5):2704–2707, 2017.

[156] Yingyan Jiang and Wei Wang. Point spread function of objective-based surface plasmon resonance microscopy. *Analytical chemistry*, 90(15):9650–9656, 2018.

[157] Lotfi Berguiga, T Roland, K Monier, J Elezgaray, and Françoise Argoul. Amplitude and phase images of cellular structures with a scanning surface plasmon microscope. *Optics express*, 19(7):6571–6586, 2011.

Appendix A

Appendix

A.1 List of equipment

Here is the list of equipments used in the SPR-DHM setup

850 nm Diode laser	Thorlabs LDM-850
Polarizer	Thorlabs LPVIS100-MP2
Waveplate	Thor labs WPHSM05-850
Filtering objective	Newport M-10X
Spatial Filter 50 µm	Newport PNH-50
Spatial Filter 1 mm	Thorlabs P1000HK
Focusing lens	Thorlabs AC254-050-AB
Imaging lens	Thorlabs AC508-600-AB
Cube beam splitter	Thorlabs SSM-1-pbs252
Imaging objective	Olympus UPLXAPO60XO
Wollaston Prism	Thorlabs WPQ10
Camera	Allied Vision Procilica GE 7.4 µm pixels

A.2 Light blocked by the edge of the imaging objective

The images are captured when the focus on the BFP of the imaging objective is scanned. Illumination is p-polarized. Water drop is not applied on the gold surface. The incident angle is larger than the critical angle of glass-air interface. As the illumination is approaching to the edge of the objective, part of the reflected light is blocked. The values of the lateral focus movement are displayed on each image.

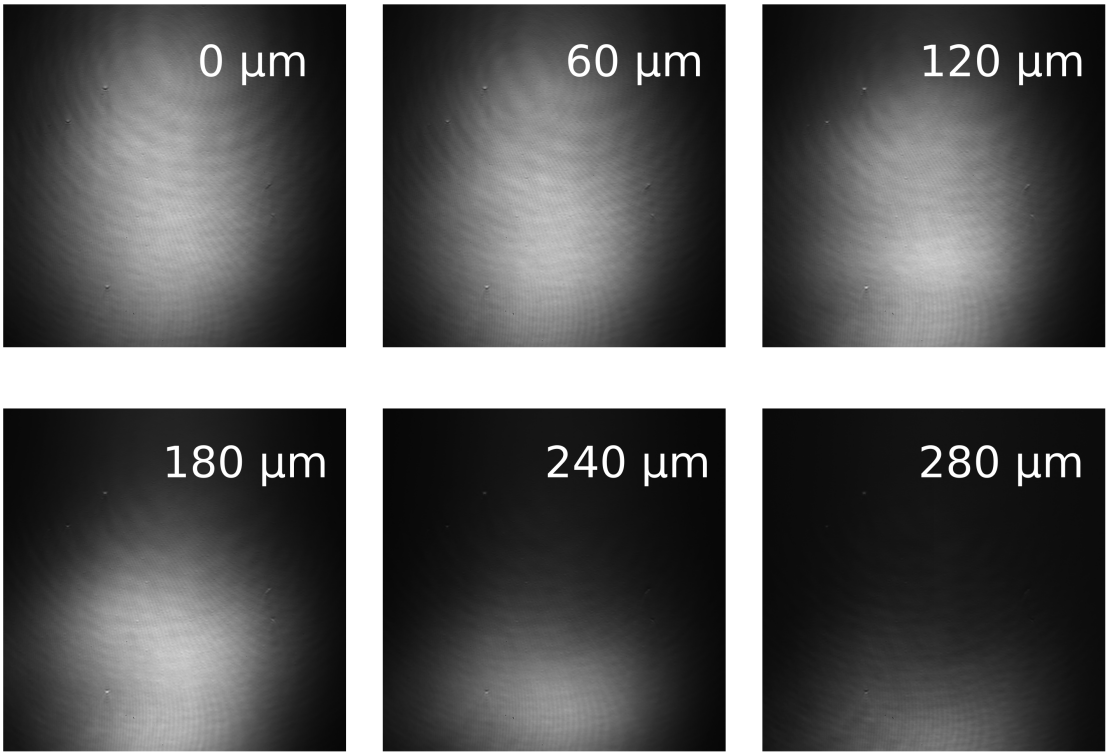

Fig. A.1 Reflected light blocked by the edge of objective.

A.3 Monitoring the evaporation of water-ethanol mixture

At the resonant angle of gold-water interface, 5 µL of water then 1 µL of ethanol are dropped on top of the gold surface. The holograms are captured every 10 seconds. Some of the holograms are shown in Fig. A.2.

The holograms are then reconstructed. The reconstructed reflectivities and phase shifts as a function of time are shown in Fig. A.3. The evaporation of the mixture is much more complex than only water. On the reflectively curve, we can observe several leaps. The phase response is relatively smooth. The RI of ethanol at 850 nm is 1.35. It is larger than the RI of water (1.33). So, at the beginning, the image is out of the resonance. The evaporation of ethanol is faster than water, we suppose the RI of the mixture will eventually converge to the RI of water. We can observe from the curves that reflectivities drop and phase shifts increase before 10 min. That may be due to the evaporation of ethanol. The reason of the leaps in reflectivity is still unclear. After 46 min, all liquid is evaporated, the reflectivities return to 1 and phase shifts drop to 0.

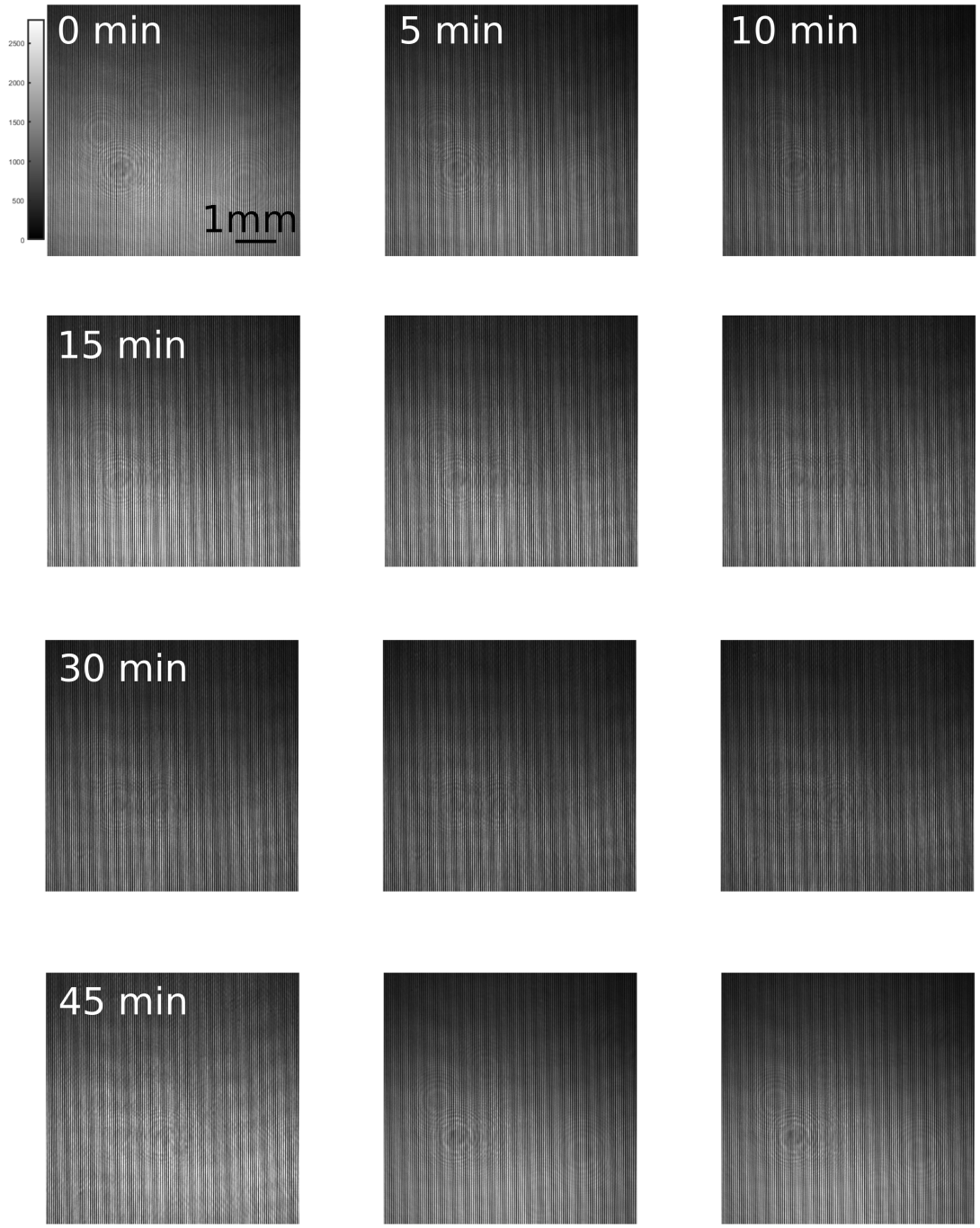

Fig. A.2 Holograms captured with water-ethanol mixture. There is a 5 min gap between shown holograms.

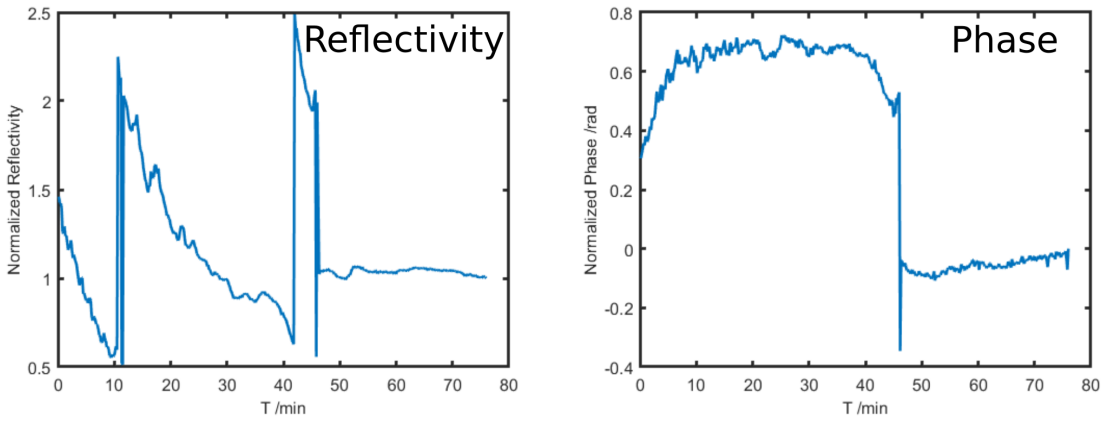

Fig. A.3 Reconstructed reflectivities and phase shifts as a function of time.

Résumé

Développement d'un microscope SPR pour imagerie de phase par holographie numérique

Doctorant : Hongyu LI

1. Introduction

La résonance du plasmon de surface (SPR) est la résonance des oscillations collectives des électrons libres à l'interface entre un matériau de permittivité négative (métal) et un matériau de permittivité positive (diélectrique), le plasmon pouvant être considéré comme une onde qui se propage le long de cette interface. La SPR peut être stimulée par une onde électromagnétique externe et se manifeste par une forte absorption. Ce phénomène a été observé pour la première fois par R.W Wood et rapporté dans sa publication en 1902. En 1968, A. Otto a présenté la première méthode d'excitation optique des ondes plasmoniques de surface non radiatives (SPW), basée sur la réflexion totale atténuée (ATR) et a donné une explication théorique de l'absorption SPR. Plus tard dans la même année, E. Kretschmann et H. Raether ont indépendamment proposé leur méthode de stimulation SPR. Leur configuration prisme-métal-diélectrique (configuration K-R) est toujours la méthode la plus utilisée pour la détection et l'imagerie SPR.

Depuis les années 1980, les techniques SPR ont été appliquées à la biodétection. Elles ont été utilisées dans divers domaines, comme le diagnostic médical, la surveillance de l'environnement et l'industrie alimentaire. La méthode de détection SPR est une méthode sans marquage, très sensible et qui convient à la détection in-vivo. Sa faible profondeur de pénétration (de l’ordre de quelques centaines de nanomètres) en fait un outil idéal pour étudier des interactions biologiques ou chimiques ayant lieu aux interfaces.

L’approche d’imagerie SPR a été proposée pour la première fois en 1988 reposant sur la configuration K-R. Elle permet une imagerie bidimensionnelle des réponses SPR en temps réel. En 2007, Huang et al. ont présenté un nouveau microscope SPR (SPRM) à grand champ de vue en remplaçant le prisme de couplage dans la configuration K-R par un objectif à grande ouverture numérique (ON). Il a une résolution beaucoup plus élevée que les systèmes SPR à prisme. Grâce à cette méthode, l’imagerie in-vivo d'une cellule unique a été réalisée.

Les réponses en phase de la SPR sont plus sensibles que les réponses en intensité. Depuis la fin des années 80, de nombreuses méthodes de détection de phase ont été combinées avec le SPRM, notamment la polarimétrie, l'hétérodynage optique, l'interférométrie et les méthodes holographiques. Parmi celles-ci, la méthode holographique présente l'avantage de pouvoir fournir des informations de phase à partir d'une seule acquisition. Elle est idéale pour faire de l'imagerie de phase SPR en temps réel et in-vivo. En 2015, B. Mandracchia et al. ont proposé un microscope holographique numérique SPR (SPR-DHM) qui combine le SPRM à objectif avec l'interféromètre de Mach-Zehnder. Plus tard en 2017, J. Zhang et al. ont présenté leur SPR-DHM en utilisant une unité holographique basée sur un prisme de Wollaston. Ils ont pu observer les mécanismes d'adhésion in vivo cellule-substrat à l’aide d’un tel système.

Les systèmes SPR-DHM disposent d'une haute résolution et d'une grande sensibilité. Cependant, en raison de l’angle élevé de la résonance SPR dans le visible, une ouverture numérique (NA) extrêmement élevée est nécessaire pour les observations biologiques qui ont lieu en milieu aqueux. Habituellement, des objecitfs spéciaux (par exemple, des objectifs TIRF à NA 1,49 ou NA 1,65) sont nécessaires. Ces objectifs sont onéreux et peu répandus dans les laboratoires biologiques. Dans cette thèse, nous proposons de concevoir et de construire un SPR-DHM opérant dans le proche infrarouge (NIR). Une diode laser

émettant à 850 nm est utilisée comme source d'illumination au lieu de la lumière visible. Elle peut réduire efficacement l'angle de résonance de la SPR. En conséquence, un objectif de microscope de NA 1.42 donc accessible, peut être utilisé. Notre SPR-DHM NIR a été expérimenté sur des interfaces or-air et or-eau.

2. Principe du microscope holograhique à resonance du plasmon de surface

Dans ce chapitre, les principes du DHM et de la SPR sont présentés. Nous passons en revue l'état de l'art de l'imagerie de phase SPR et du SPR-DHM. Dans la première section, nous rappelons la Physique de base de l'approche scalaire de la diffraction. Nous présentons ensuite la théorie de l'holographie numérique et comparons les configurations holographiques en ligne et hors axe. Nous justifions le choix de l'holographie hors axe pour ses avantages en matière d'imagerie en temps réel. Dans la deuxième section, la Physique de la SPR est abordée, et les méthodes de stimulation de la SPR sont présentées. Nous expliquons que la source NIR peut réduire l'angle de résonance. Dans la dernière section, nous passons en revue les développements de l'imagerie de phase SPR. Nous montrons finalement que la méthode holographique numérique est la plus appropriée.

Montage du microscope

En utilisant la source NIR à 850 nm, l'angle de résonance est à 65 degrés. L'exigence de NA pour l'objectif du microscope de couplage (MO) est alors réduite à 1,37. Pour ce projet, un objectif corrigé à l'infini de NA 1,42 a été sélectionné. Le schéma du SPR-DHM est illustré à la Fig. A1. Le système peut être séparé en trois parties : la partie éclairage, la partie couplage et imagerie SPR, et la partie génération d'hologrammes.

Système d'illumination

Le système d'illumination contient une diode laser NIR 850 nm, un polariseur, une lame demi-onde, un filtre spatial (objectif et trou microscopique) et une lentille de focalisation. La source NIR est polarisée, filtrée puis focalisée sur le plan focal arrière de l'objectif du microscope. Le système est installé sur une table de translation pour le contrôle de la position de focalisation.

Système de stimulation et d'imagerie SPR

Cette partie comprend un cube séparateur, l'objectif à grande ouverture numérique, une lentille de formation d'image et un filtre spatial. La lumière est focalisée sur le plan focal arrière de l'objectif du microscope. Ellle est ensuite collimatée par le MO sur son plan focal avant. La lumière illumine l'interface or-diélectrique à l'angle de résonance de la SPR. La lumière polarisée p stimule la SPR, et le faisceau réfléchi porte l'information de l'interaction entre l'échantillon et le plasmon de surface. La partie polarisée s ne peut pas exciter la SPR, elle est directement réfléchie par l'interface métallique et sert d'onde de référence. Les lumières réfléchies sont ensuite collectées par une lentille à longue distance focale. L'objectif et cette lentille à longue focale peuvent être considérés comme un système 4-f qui dirige l'information vers le capteur.

Système de formation d'hologrammes

Dans ce travail, l'information sur la phase de la SPR est obtenue par une méthode holographique pour pouvoir faire l'imagerie en temps réel. Nous avons choisi une configuration holographique hors axe à trajet commun qui s'inspire des travaux de Zhang. Cette configuration utilise un prisme de Wollaston qui permet de séparer la lumière polarisée p de la lumière polarisée s avec un petit angle. L'onde p qui transporte les informations de la SPR est l'onde objet. L'onde s, puisqu'elle est réfléchie directement, sert d'onde de référence. Les ondes objet et de référence polarisées orthogonalement sont combinées par

un polariseur linéaire. L'hologramme est alors enregistré sur une caméra CMOS conventionnelle sans filtre IR.

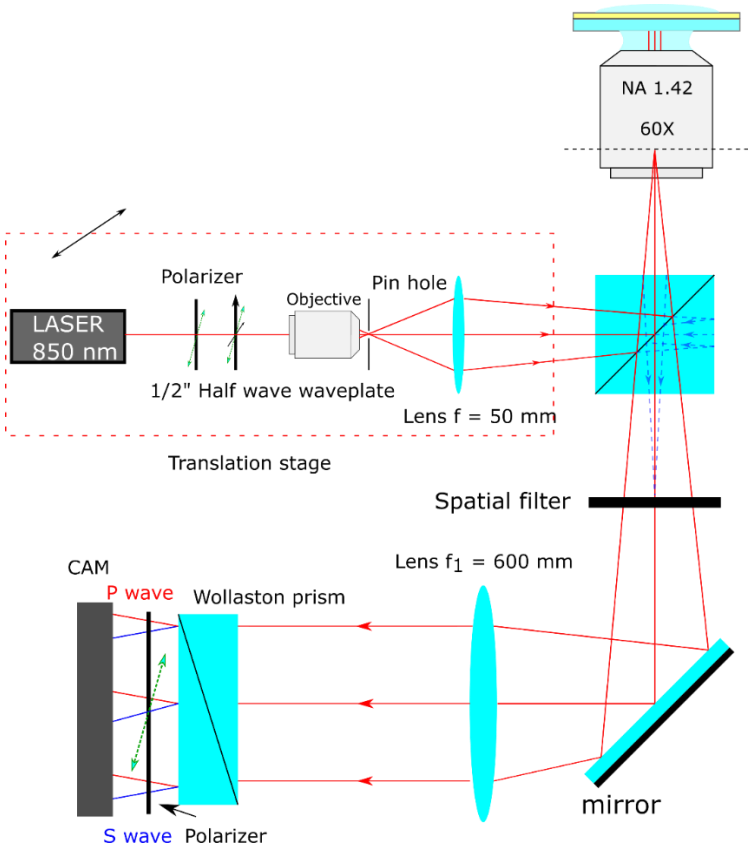

Fig. A1 Représentation schématique du SPR-DHM

3. Algorithmes de reconstruction

En général, la reconstruction d'un hologramme hors axe se compose de trois étapes. Dans la première étape, la composante de l'objet est filtrée du spectre de l'hologramme. Ensuite, dans la deuxième étape, on utilise une méthode scalaire de propagation pour la restitution de l'objet. La distance de propagation est déterminée par un algorithme d'auto-focalisation. Enfin, des post-traitements sont appliqués au front d'onde complexe reconstruit. Le plus courant est le déroulement de la phase. La correction des aberrations peut être également appliquée, et est généralement complexe. Cependant, dans notre configuration, les ondes de référence et objet suivent le même chemin optique,

donc les aberrations introduites par les composants sont automatiquement corrigées.

Reconstruction numérique d'un hologramme off-axis

Le champ d'interférences dans le plan de l'hologramme pour la configuration basée sur le prisme de Wollaston s'écrit comme suit :

$$H = O^2 + R^2 + R^* O \exp[jk \sin(\theta)\, y] + R O^* \exp[-jk \sin(\theta)\, y]$$

O représente l'onde objet, *R* désigne l'onde de référence. θ est le angle de division du prisme de Wollaston. Le spectre de l'hologramme hors axe est représenté dans la Figure. A2. Les deux premiers termes de la formule forment l'ordre zéro du spectre. Les deux dernières expressions identifient les ordres +1 et -1, pour lesquels la bande spectrale suivant les fréquences spatiales fy vaut 2B. En raison de la modulation spatiale, ces ordres sont situés de part et d'autre de l'ordre zéro. L'angle θ doit être suffisamment grand pour éviter le chevauchement. En filtrant l'ordre +1 ou -1, on récupère le spectre du champ complexe. Ce dernier peut être reconstruit en appliquant une transformée de Fourier inverse.

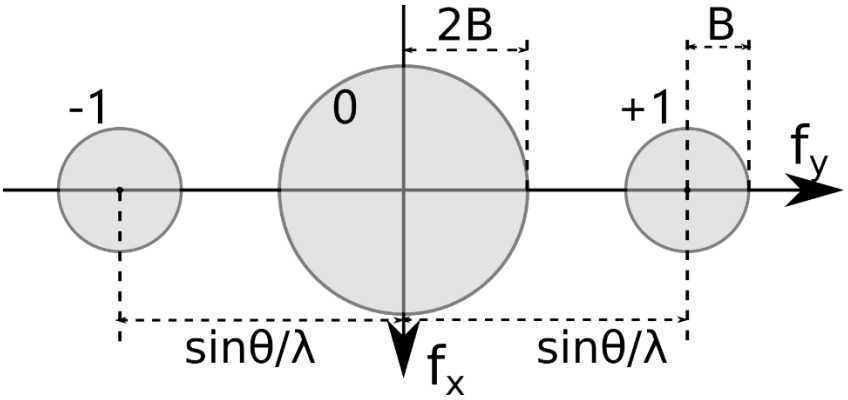

Fig. A2 Représentation schématique du spectre d'un hologramme hors axe. θ est l'angle de division du prisme de Wollaston.

L'onde d'illumination n'est pas parfaitement collimatée en réalité. Elle contient du bruit et des aberrations. Pour d'éliminer le bruit et les aberrations, un hologramme de référence est nécessaire. Il est enregistré sans l'échantillon, de

sorte que sa reconstruction ne contiendra que les aberrations et le bruit de l'onde de référence. Une telle référence $O_r(x,y)$ est obtenue par la méthode de filtrage. En notant $O_s(x,y)$ la reconstruction avec l'échantillon, l'élimination du bruit est effectuée en divisant l'amplitude complexe $O_s(x,y)$ par $O_r(x,y)$.

Algorithme de diffraction scalaire

Dans une configuration holographique parfaite, le capteur est positionné précisément sur le plan de l'image. La reconstruction serait directement réalisée par une simple transformée de Fourier après filtrage. En réalité, ces deux positions ne sont pas nécessairement identiques. Par conséquent, le champ d'onde reconstruit doit être propagé vers le plan image. Parmi les nombreuses méthodes scalaires, celle du spectre angulaire à bande limitée (BL-ASM) a été choisie. La méthode ASM est une solution rigoureuse de l'équation scalaire des ondes, et la discrétisation du champ d'ondes ne dépend pas de la distance de propagation. Pour cette raison, elle est adaptée au processus d'auto-focalisation pour lequel une même fonction de coût doit être calculée à plusieurs distances de reconstruction. Cependant, l'ASM classique ne convient que pour le champ proche. La propagation en champ lointain entraîne des problèmes d'échantillonnage de la fonction de transfert. La méthode ASM à bande limitée résout ce problème en limitant le spectre à propager. Une telle limitation du spectre n'affectera pas l'information effective.

Algorithme d'auto-focalisation

Plusieurs algorithmes d'auto-focalisation ont été expérimentés avec un système holographique sans lentille, notamment la méthode basée sur l'amplitude, la méthode basée sur le gradient et la méthode basée sur la faible densité du gradient. Parmi ces méthodes, celle basée sur la faible densité du gradient montre la meilleure robustesse et précision sur l'hologramme en ligne. Une erreur de 10 microns à la distance de 17,88 cm a été obtenue.

Sur notre SPR-DHM, la précision tombe à 2 mm. La méthode n'est donc pas

adaptée à notre système. Comme nous avons utilisé une lentille de focale 600 mm, notre système a une grande profondeur de champ. Cette profondeur de champ théorique est d'environ 4,5 mm. La profondeur de champ mesurée est de 3,4 mm. Puisque la profondeur de champ du microscope est suffisamment grande, la mise au point de notre système est ajustée manuellement au lieu d'utiliser l'algorithme d'auto-focalisation.

Algorithme de déroulement de la phase

Plusieurs méthodes ont été expérimentées : La fonction "unwrap" de Matlab, un algorithme de déroulement de phase piloté par la fiabilité (2D-SRNCP), et le déroulement de phase bidimensionnel robuste, basé sur la transformée en cosinus rapide. Ces trois algorithmes représentent deux catégories de méthodes. Les deux premiers sont des algorithmes de suivi de chemin basés sur la différence de phase locale de pixels adjacents, et le dernier est une méthode de déroulement par la méthode des moindres carrés, qui minimise une fonction de mérite sur l'ensemble de l'image.

La fonction "unwrap" n'a pas donné de bons résultats car elle propage le bruit de phase à toute une ligne ou colonne de pixels. La méthode 2D-SRNCP et la méthode des moindres carrés ont toutes deux correctement déroulé la phase dans notre cas. Au final, nous avons choisi la méthode des moindres carrés car elle est plus rapide que la méthode 2D-SRNCP pour les grandes matrices. Bien que la méthode ne puisse pas traiter correctement les points singuliers, de tels points sont rarement présents sur les images de phase SPR.

4. Expérimentation et résultats

L'échantillon est fabriqué par la méthode de dépôt physique en phase vapeur (PVD) dans une salle blanche. Environ 3 nm de couche d'adhérence en Cr et 45 nm de couche d'or ont été déposées sur une lamelle de 85 µm d'épaisseur fabriquée par SCHOTT (verre D263). La lamelle étant extrêmement fragile, un

support a été conçu puis fabriqué par impression 3D.

Imagerie SPR-DHM de l'interface or-air

Tout d'abord, la réponse en intensité de la SPR à l'interface or-air a été étudiée. La position de résonance a été détectée en balayant la position de focalisation au niveau du plan focal arrière. Ensuite, l'image en intensité de la SPR a été enregistrée avec une lumière en polarisation p et s, comme le montre la Figure. A3.

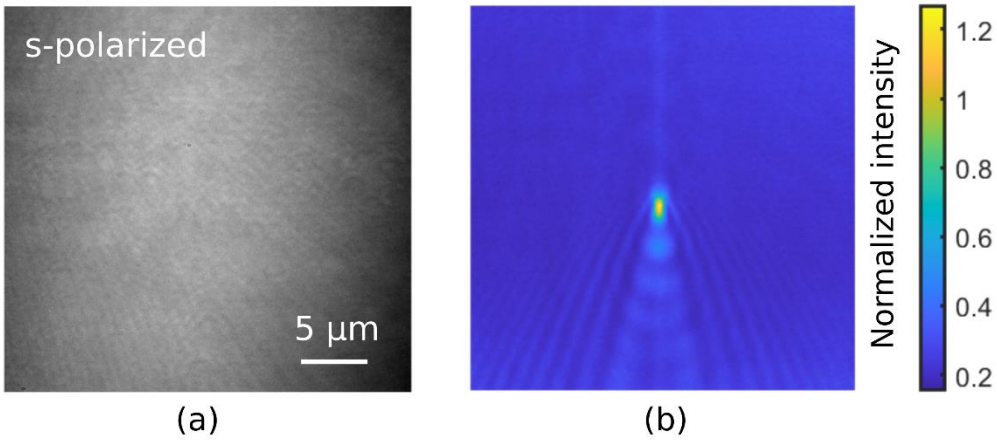

Fig. A3. Image en polarisation s (a) et image SPR normalisée (b).

Puis leurs spectres ont été analysés. Sur le spectre de la polarisation s, seule la réponse de l'objectif a été observée. Sur le spectre de l'image en polarisation p, on observe en plus une composante en forme d'anneau qui correspond à la stimulation de la SPR. Ces spectre sont représentés dans la Figure. A4. L'hologramme enregistré avec l'unité holographique à base de prisme de Wollaston, est représenté dans la Figure. A5.

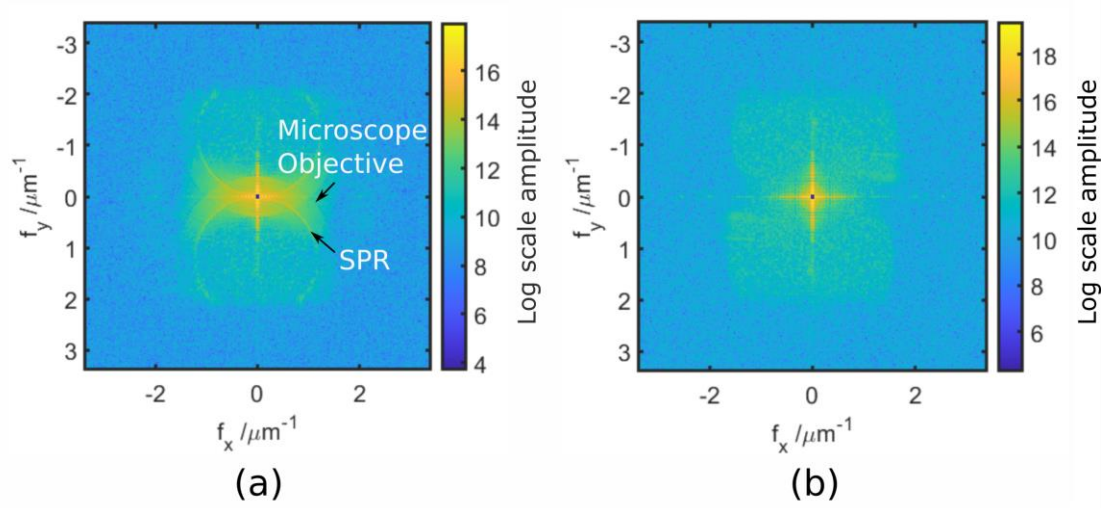

Fig. A4. Spectres en polarisation p et s (amplitude en échelle logarithmique), les 3x3 pixels centraux sont masqués (a) Spectre de l'image en polarisation p (b) Spectre de l'image en polarisation s

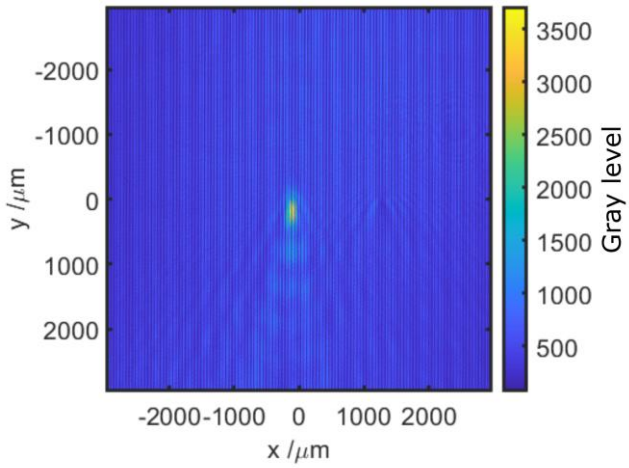

Fig. A5. Hologramme SPR pour l'interface or-air

L'hologramme SPR a été reconstruit par la méthode de filtrage introduite précédemment. Comme mentionné plus haut, il contient des aberrations et du bruit. L'hologramme de référence a été pris à l'angle de résonance de l'interface or-air en mettant une goutte d'eau dans le champ d'observation. L'angle de résonance SPR or-air étant beaucoup plus petit que celui de l'interface or-eau, l'information SPR n'est plus acquise. En divisant l'hologramme de l'échantillon reconstruit par celui de l'hologramme de référence, on obtient une reconstruction normalisée.

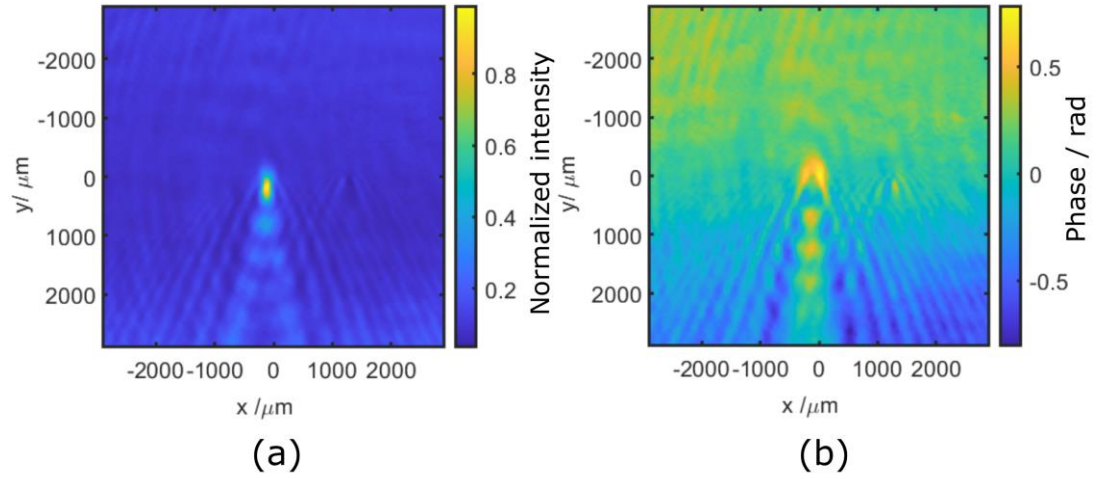

Fig. A6. Reconstruction avec élimination des aberrations et correction d'intensité. (a) Intensité reconstruite. (b) Phase reconstruite.

Imagerie SPR-DHM de l'interface or-l'eau

2 µL d'eau ont été déposés sur la surface d'or. La position de résonance SPR a été trouvée en modifiant la position de focalisation sur le plan focal arrière de l'objectif. L'hologramme SPR de l'interface or-eau a été ainsi enregistré. L'hologramme de référence a été pris à l'angle de résonance SPR or-eau, avant injection du milieu aqueux. Comme l'angle de résonance de l'interface or-air est beaucoup plus petit que celui de l'interface or-eau, la SPR n'est pas stimulée. La reconstruction normalisée est présentée dans la Figure. A7.

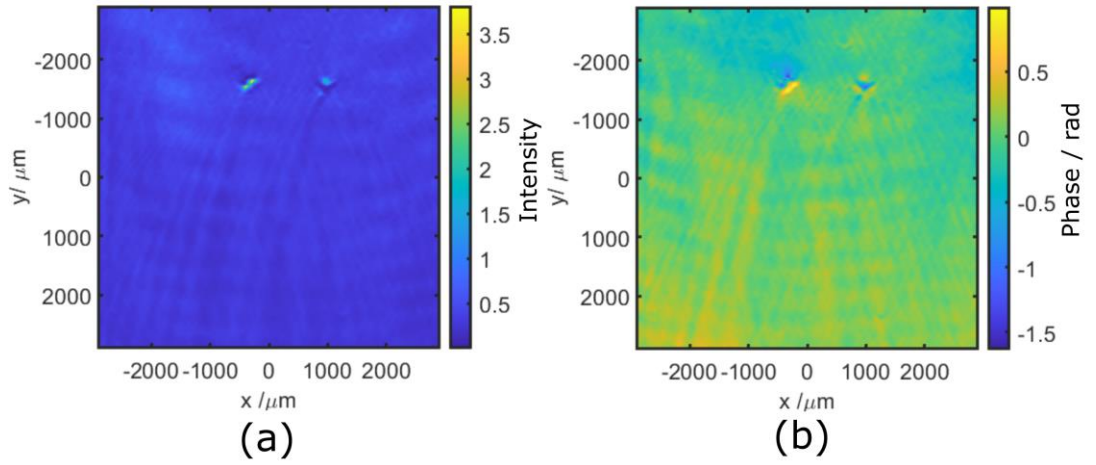

Fig. A7. Intensité et phase reconstruites après normalisation par un hologramme de référence. (a) Distribution de l'intensité (b) Distribution de la phase.

Une observation continue de l'interface or-eau a été menée. Les hologrammes ont été pris toutes les minutes. La Figure. A8 représente les variations de la réflectivité et du déphasage en fonction du temps. 5 µL d'eau déposée sur la surface d'or, ont été totalement évaporés après 40 minutes : la réflectivité passe à 0,98 et le déphasage à 0,08 rad.

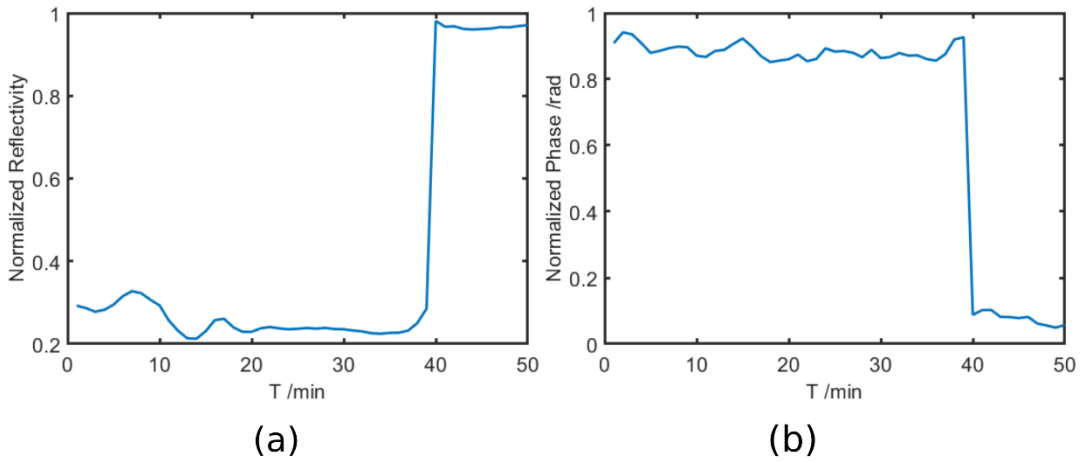

Fig. A8. Variation de la réflectivité et du déphasage avec le temps. (a) Réflectivité (b) Phase.

5. Conclusion

Nous avons conçu et réalisé un microscope d'holographie numérique à résonance de plasmon de surface opérant dans le proche infrarouge (NIR-SPRDHM). Ce système diffère des SPRDHM conventionnels qui reposent sur des objectifs TIRF spéciaux. Nous avons choisi une diode NIR émettant à 850 nm comme source lumineuse, ce qui permet l'utilisation d'un objectif de microscope de NA 1,42. Le système a été expérimenté sur des interfaces or-air et or-eau. Les expériences ont mis en évidence la capacité du microscope à stimuler et à enregistrer les réponses en phase de la SPR, révélant ainsi sa potentialité pour des applications en imagerie biologique.